Analysis of Fracturing Processes Preceding Caldera Collapse

Ing. Michael Somr

supervisor: **Prof. Ing. Petr Kabele, Ph.D.**

Czech Technical University in Prague
Faculty of Civil Engineering

A thesis submitted for the degree of
Doctor of Philosophy
March, 2019

I would like to dedicate this thesis to my recently deceased grandfather Ludvík Tomášek. He always appreciated my achievements, including the academic ones. I will never forget our great talks...

Acknowledgements

First of all, I would like to thank my supervisor professor Petr Kabele for his unlimited willingness and patience. He trusted me, believed in me and my abilities, and spent countless hours of his precious time explaining me whatever I needed. It is an honor to work with him, and his precision always motivates me to do my best.

I would also like to thank professor Jiří Žák from the Institute of Geology and Paleontology at the Faculty of Science, Charles University and Filip Tomek from the Institute of Geology at the Czech Academy of Sciences for numerous consultations and cooperation on the geological part of the project, and to professor Bořek Patzák from Department of Mechanics at the Faculty of Civil Engineering, CTU in Prague for precious consultations and understanding from his position of the Vice-Dean for Science and Research.

Special thanks go to my parents Petra and Dušan for their huge support during the years of my study, to my wife Pavla and daughter Anna for their patience and support when I spent countless hours at the computer instead of being with them, and to my friend and colleague Václav Nežerka for many discussions and long mind-refreshing bicycle rides.

The support of the Czech Science Foundation, project No. GAČR P210/12/1385, and of ADINA R & D, Inc. is also gratefully acknowledged.

Abstract

Calderas are volcanic depressions caused by rupturing of a magma chamber roof as a consequence of pressure evolution inside the chamber. The collapse of a caldera is accommodated by ring faults, whose formation is commonly accompanied by ejection of large volumes of pyroclastic material to the Earth's atmosphere and thus represents severe volcanic hazards for the environment, climate, and human society. However, it can also be beneficial as it may contribute to the formation of ore deposits, serve as geothermal energy resources, and produce fertile soils. A deeper understanding of geological conditions under which these events can occur is thus of great importance and interest. Geological survey and field studies can usually access just surface manifestation of immense magmatic processes taking place under the Earth's surface. In this respect, numerical analysis has proven as a key tool in understanding the mechanical conditions of caldera collapse.

In order to advance the knowledge and bring new views on fracturing processes preceding caldera collapse through mathematical modeling, numerical simulations, and analysis, extensive research was carried out. Based on a state-of-the-art review, outstanding issues, which are still a subject of debate in the research community, were identified and provided the objectives for the thesis.

To achieve the goals, the finite element method (FEM) was employed in this work due to its capabilities and universality. To make the FE simulations realistic, yet feasible, appropriate modeling strategy, material models and parameters, and simplifying assumptions were selected.

Subsequently, many cases covering a wide range of possible magma chamber geometries and roof aspect ratios (roof thickness/chamber diameter)—from shallow to deep-seated, mid-size and large, tabular and cylindrical—were calculated. Nevertheless, 12 cases, which were selected as the most representative, were in detail analyzed, interpreted, and discussed in terms of geological phenomena in the presented thesis.

The modeling strategy employed in this work demonstrates that pressure evolution inside a magma chamber is manifested by a range of fracturing processes in the host rock. These processes are not restricted to the formation of various ring faults alone but may also include radial and circumferential fracturing, surface tearing, magmatic stoping, and cauldron subsidence. The modeling strategy also enables capturing, orientation (inward-dipping, vertical, outward-dipping), mode (shear or extension), and direction (upwards, downwards) of a ring fault initiation and growth. Moreover, a dependence of the fracturing processes on the roof aspect ratio is identified and analyzed.

Contents

Chapter 1

Introduction and state of the art

Caldera is a volcanic feature resulting from a depression of a magma chamber roof, typically 1–20 km, but in some cases up to 80–100 km in diameter (e.g., [1, 2]). When a large amount of magma is erupted from the chamber over a short time, the roof loses the structural support and collapses, see 1.1. The calderas may be mistaken for apical craters, which are a result of the volcanic conduit collapse, while the chamber roof is unimpaired and therefore also the diameter of the structure is much smaller. The calderas are an evidence of the most powerful displays of the volcanic energy hidden beneath the Earth's surface. Consequences of this phenomenon, which is always followed by immense pyroclastic eruptions, are both negative and positive. It represents a huge danger for the environment and society claiming thousands of lives [3–6], however, ore resources and fertile soils made of the erupted volcanic material can be generated this way [7, 8]. Caldera collapse represents a relatively rare phenomenon as approximately three new calderas occur every 100 years since 1783 [9]. Nevertheless, the processes accompanying its origin can be devastating and belong among the most catastrophic geologic events that have occurred on the Earth's surface. This is one of the reasons, why calderas have received a significant attention of researchers in last several decades. Another reason is that it is mostly not possible to observe huge magmatic processes ongoing under the surface, since just the surface manifestations, like volcanoes and eruptions, are visible. The calderas can provide an important insight into the generation and evolution of large-scale silicic magma bodies [10].

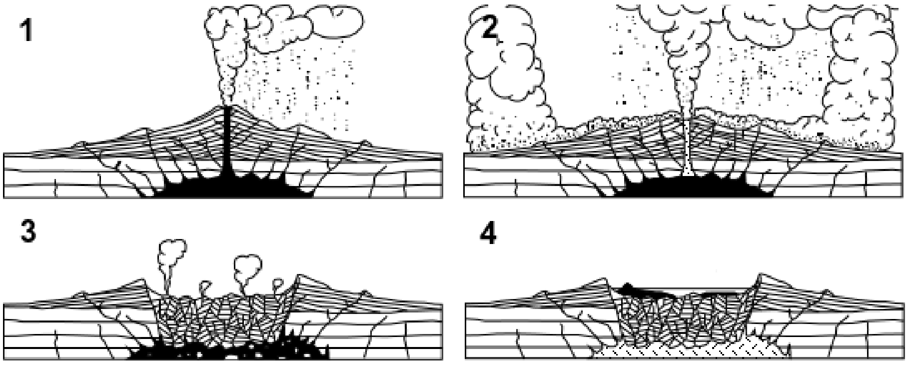

Figure 1.1: Scheme of a caldera collapse (reproduced from [11]).

Caldera collapse and associated volcanic eruptions represent a climactic stage in the evolution of magmatic systems after a period of shallow magma chamber growth (e.g., [1, 12–15]).

The chamber growth usually consists of several fresh magma additions (e.g., [16–26]), which is coupled with the chamber inflation/deflation stages meaning that caldera-forming eruptions are in some cases preceded by the pressure build-up. In the case of positive excess magma pressure, so called overpressure calderas, a formation of ring faults enabling the caldera collapse is superposed on previous doming of the chamber roof (e.g., [27, 28]). These conclusions correspond to seismic and ground-deformation measurements that reveal an oscillating up-down motion above active magma chambers (e.g., [29–31]) meaning, that the spatial, temporal, and mechanical link of magma chamber roof uplift and collapse may be much more common than previously envisaged (e.g., [32, 33]). To understand the comprehensive topic of the calderas, a cooperation of several scientific disciplines is necessary, e.g., geophysics [34–36], petrology [37–39], geochemistry [37, 38, 40].

A key tool for a quantitative assessment and better understanding of kinematics and dynamics of caldera collapse has been provided by theoretical and analogue models using various methods and including various initial and boundary conditions and simplifying assumptions (e.g., [41–56]). However, the models have often yielded contradictory results. The main controversies relate to the development and evolution of caldera ring fractures.

Field studies have evidenced extensive chamber roof fracturing during chamber growth caused by magma emplacement, thermal stresses, and hydraulic fracturing by fluids released from the magma (e.g., [57–60]). However, most of theoretical models consider chamber roof doming as a simple elastic bending without explicit display of fractures (e.g., [61–64]). Nevertheless, crack formation causes stress redistribution in the volcanic system, and it represents a significant factor in the evolution of ring faults. Advanced theoretical models should therefore incorporate development of fractures in the roof prior to ring fault propagation and caldera collapse. To understand and properly simulate the above-mentioned processes, it is necessary, in ideal case, to have data about real volcanic structures from field studies, knowledge of magma material properties at high pressure and temperature, and a robust numerical model.

1.1 Collapse mechanisms

Traditionally, two main mechanisms triggering a depression and subsequent collapse of a magma chamber roof leading to a caldera formation are cited in the literature: (a) positive excess pressure (overpressure) inside the magma chamber causing fracturing of the roof (e.g., [48, 55, 65–71]), and (b) negative excess pressure (underpressure) within the magma chamber following a magma depletion due to, e.g., an eruption (e.g., [1, 12, 13, 41, 47, 72–76]). Next to the excess pressure mechanisms, the influence of an overburden (ash-flow units) is also considered as a possible trigger causing fracturing of the roof from above (e.g., [7, 44]).

However, as there are two hypotheses of trigger mechanism, there are also two groups of researches favoring one or the other. The underpressure mechanism is very popular when modeling processes leading to caldera collapse, but several papers have disproved the arguments justifying this approach (e.g., [67, 77]). The authors mostly question differences in dip directions of the ring faults predicted by models and those documented by field studies, disproportion between the volume of the erupted material and the volume occupied by the collapsed material, etc. One of the most appealing arguments against underpressure trigger mechanism is that conduits and/or feeder dikes would stop erupting magma from the chamber before the necessary collapse-triggering negative excess pressure is reached. On the other hand, paper by Pinel and Jaupart [78] shows that the conduit closure can be prevented if an overburden with appropriate size and weight is present. The overburden alters stress field enabling caldera collapse during deflation.

From the previous paragraphs is obvious that there are sound arguments for both over- and underpressure mechanisms, but the arguments are mostly contradictory. Some of the other recognized arguments are stated below.

1.1.1 Overpressure

In the case of overpressure calderas the magma chamber is overpressurized at the moment of the collapse, and the stress field conditions leading to the formation of ring faults are achieved prior to initiation of the eruption. Overpressure in a magma chamber can be caused by a fresh magma income (e.g., fed by a deep-seated magma reservoir), doming (causing remote horizontal tensile stresses and vertical compressive stresses), underplating (e.g., due to movement of tectonic plates), etc. Pressure can increase until it exceeds the tensile strength of the host rock and ring faults occur. To reach large explosive eruptions, the overpressure must exceed the host rock tensile strength by one or two orders of magnitude [67]. Such a rapid increase of pressure before eruption is probably caused by gas expansion (e.g., [79–81]. However, it remains unclear how the gas expansion can be so fast that the gas does not permeate the chamber walls.

1.1.2 Underpressure

The process begins with overpressure inside a chamber, as described in Section 1.1.1, which fractures the host rock creating a feeder dike. Then the pressure inside the chamber decreases to values lower than lithostatic pressure. With further pressure decrease the magma chamber tends to reach lithostatic pressure, the roof deforms and fractures, and caldera forms.

Druitt and Sparks [41] argue for the underpressure model claiming that geological relationships in pyroclastic deposits associated with large caldera eruptions provide independent evidence for this model. They also conclude that in most volcanic systems only small to moderate volumes can be erupted while the chamber remains overpressurized. Magma can be further discharged from the chamber even after the internal pressure decreases below lithostatic. However, the feeder dike or conduit must have suitable geometry or sufficiently irregular shape to remain opened. The magma ascends due to imbalance between the hydrostatic pressure of the vesiculating magma column in the conduit and the magma chamber pressure. The low density of the vesiculating magma results in the hydrostatic pressure being significantly lower than the chamber pressure even when the chamber pressure has fallen below the lithostatic value. The underpressure is expected to be sufficient for the roof of the chamber to collapse.

Cashman [82] states four key events leading to caldera resulting from the underpressurized chamber: (1) development of stably zoned magma chamber by crystal fractionation, where crystal-liquid separation is driven by settling of individual crystals or crystal plumes within a large batch of liquid that cools from the margins inwards, (2) eruption initiation by injection of a (vertical) and pressurized dike, (3) magma withdrawal starting from the top of the chamber and propagating downwards, as evidenced by deposits that are reversely zoned in composition and/or pre-eruptive temperature and pressure, and (4) caldera formation by collapse of an underpressurized magma chamber after some fraction of magma has been withdrawn.

Gudmundsson [67] questions the underpressure models because if a spherical magma chamber is subject to negative excess pressure as the only loading, then the tensile stress at the surface is too small to cause fracturing. Moreover, the location of the maximum shear stress is not suitable for ring fault initiation. Gudmundsson also points out that the volume of collapse and the associated volume of eruptive materials do not correspond (e.g., [83]) and that the negative excess pressure model assumes that underpressure in the magma chamber can drive out large volumes of magma [41, 72].

1.2 Ring faults

Despite the controversies about the mechanisms causing a caldera collapse (see Section 1.1), there is a broad agreement on the fact that roof block depression is enabled by a set of ring (concentric) faults. The roof can then subside as coherent block, as in the case of the Silali caldera [84], or in a fragmented and/or chaotic way, as the Somma Vesuvius calderas [85]. The ring faults are traditionally distinguished as dip-slip (reverse or normal) faults or mixed-mode (shear and extension) fractures. Recently, it has been evidenced that also oblique-slip faulting (combination of strike- and dip-slip) can be present during a caldera collapse [86, 87]. However, a layout of ring faults at depth is still unresolved, because the information about calderas deeper structures are available only due to relatively rare monitored collapses (e.g., Sierra Negra [88], Rabaul [89], Piton de la Fournaise [90], Miyakejima [91]) and partially eroded calderas (e.g., Glencoe [39, 92], Scafel [93, 94]). This fact launched a questioning about ring faults initiation and propagation and about the internal configuration of faults and fractures. Researchers therefore investigate the direction of ring faults propagation (either starting from the surface and extending downwards until reaching the magma chamber, or starting from the magma chamber and growing upwards to the surface) and their orientation (outward-dipping, vertical, or inward-dipping, as described in Figure 1.2). It is worth mentioning that all the previously mentioned possibilities of the propagation direction and dip orientation exist and have been proven by field and geophysical evidences [15, 95]. Possible approaches of the ring faults investigation follows.

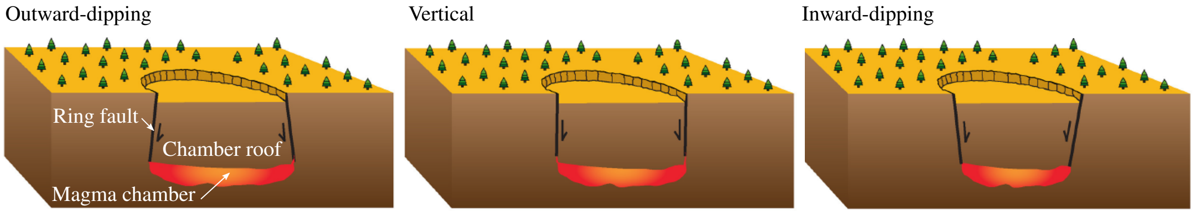

Figure 1.2: Classification of the ring faults orientation (reproduced from [96]).

1.2.1 Analogue models

Not only caldera collapse, but all volcanic processes involve an interaction of a huge variety of phenomena, materials, and phases. Most of them are hidden beneath the Earth's surface and are not directly observable. A certain way how to make them visible is an experimental investigation employing analogue models (e.g., [42, 45, 46, 49, 74, 75, 95, 97–101]). A host rock around the magma chamber is usually substituted by dry quartz sand, flour, etc., and the chamber is modeled using, e.g., water or air-filled balloons or silicone reservoirs. Analogue models are a useful tool, which can be used for comparison with theoretical models. However, analogue models are always smaller than real volcanic systems and to scale them to real dimensions is generally not possible. They are also limited by an inability to represent realistic mechanical behavior of rock and dynamics of volcanic fluids. Therefore, a more conclusive approach is to utilize a theoretical modeling, which enables including a wide range of physical approaches and properties, material and rheological models, geometries, types of loading, etc.

1.2.2 Theoretical models

If the quantification of variables is required, than theoretical models play a key role (e.g., [43, 44, 47, 52, 53, 76, 102–104]). They are mostly based on the thermodynamics and solid and fluid mechanics and their increasing importance in the research of the caldera formation is indisputable. It is possible to include the physical properties of the host rock and magma into the analyses, which enables predicting semi-quantitative conditions for fracture and fault formation. However, this can be a weakness as well since insufficient knowledge of input parameters and/or rheology, boundary conditions, and geometry may give incorrect results.

1.2.3 Field studies

Next to the analogue and theoretical models, there are also field studies, which examine and monitor reality (e.g., [89, 92, 105–108]). Nevertheless, the field studies are more or less limited to surface phenomena. Main advantage of the field studies is that they can be compared with the models to check their veracity. The studies provide information about the structure of the caldera and may also determine the pre-eruptive conditions of magma and triggers of the eruptions [109].

1.3 Numerical simulation

Sophisticated and more realistic theoretical models involve complex systems of equations. Nowadays, these systems can be efficiently solved by different numerical methods. These methods are widely available in computer programs and they are fast and relatively accurate. Therefore, their importance is still rising not only in the volcanology. The efforts to advance the knowledge about collapse caldera mechanics and to tackle with limitations of the analogue models led to development of several theoretical models in last decades. A proper caldera model should cover physical processes in both interior and exterior of a magma chamber. Nowadays, the standard practice is to deal with one of the domains, i.e., magma chamber or host rock, while the other is taken into account employing various simplifying assumptions [51], because our present knowledge does not enable coupling magma dynamics and host rock mechanics into one unified model. Therefore, the ongoing research employs either solid mechanics based models (fracturing and faulting of the host rock, e.g., [44, 67, 76]), or fluid mechanics and thermodynamics based models (pressure evolution inside the magma chamber prior to and during caldera collapse, e.g., [68, 110]). As the presented thesis focuses on solid mechanics, the first group of models is to be further described.

1.3.1 Modeling approaches

As mentioned above, setups considered at caldera collapse modeling consist of two domains—magma chamber and host rock. The magma chambers are most commonly represented as circular or elliptical cavities (e.g., [48, 55, 104]), domains filled by a viscous fluid (e.g., [17]) or by rigid particles simulating particulate flow (e.g., [56, 76]), or the chamber is omitted and its loading effect is simulated by a subsiding piston [52].

When dealing with host rock modeling, the research works can be divided into three groups with respect to the approach the authors used to reach their goal. The most commonly used are the elastic continuum models, which encompass only host rock (e.g., [47, 69, 104, 111]). These models give stress field around the magma chamber, which enables estimating a location of the ring fault origin indirectly. The non-elastic continuum models, on the other hand, can predict the position of the faults directly (e.g., [7, 44, 54, 55, 102, 103, 112]. The discontinuum-based models (distinct element method [76], discrete element method [52], smoothed particle hydrodynamics [48], etc.) are able to exactly determine not only position of fault, but also its width, shape, etc. All the models are more deeply discussed in the following subsections.

1.3.1.1 Elastic continuum models

These models are suitable for determining the geometrical configuration of the magma chamber which induces the stresses needed to initiate the ring faults. The magma chamber is considered as an empty cavity which inflates (positive excess pressure) and deflates (negative excess pressure), thus applying loading to the surrounding host rock. Most authors consider two-dimensional numerical models (e.g., [7, 42, 47, 53, 104, 113]). Results of such models were compared with three-dimensional analytical and numerical models [69], and it was proven that magnitudes of stress are different, but local stress fields distributions are similar. As the analysis is based on elastic solution (e.g., [47, 67, 104]), the following conditions, formulated using the principles of strength of materials, must be satisfied simultaneously in order to encourage the initiation of the ring faults. Let σ_1, σ_2, and σ_3 be the principal stresses, where $\sigma_1 \geq \sigma_2 \geq \sigma_3$, and compressive stress is assumed to be positive. Then the conditions are defined as follows: (1) the minimum value of σ_3 (i.e., the maximum tensile stress) must be at surface, (2) the maximum value of $\sigma_1 - \sigma_3$ (i.e., the double of the maximum shear stress) must occur at the margins of the magma chamber, (3) the minimum value of σ_3 at the surface must be approximately above the lateral margins of the magma chamber. Moreover, Folch and Martí [47] specified that the minimum value of σ_3 should be in the area defined by the angle $\alpha \leq$10–15° [96], see Figure 1.3.

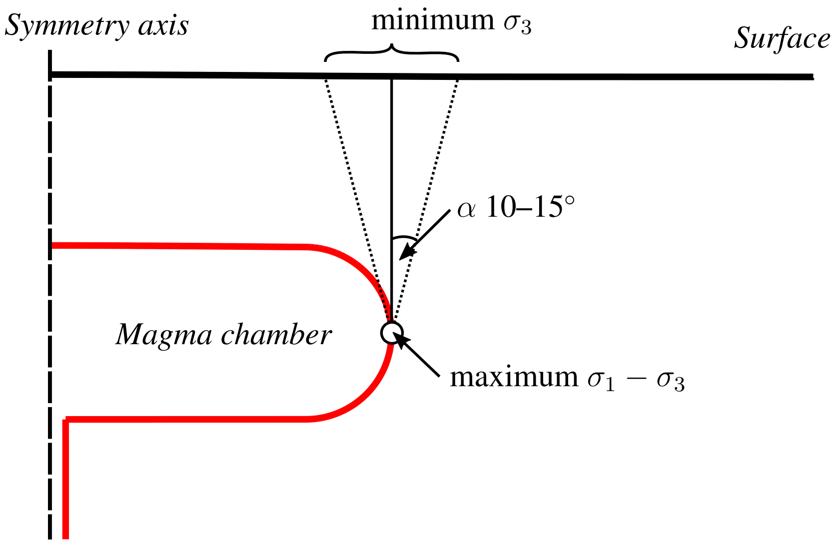

Figure 1.3: Graphical representation of the three conditions necessary for formation of normal ring faults in elastic models.

The research works employing the elastic models investigated: magma chambers subjected to different loading conditions (overpressure, underpressure, regional tectonic stresses, topography, etc.)(e.g. [33, 67, 78]); volcanic systems with various chamber geometries (width, height, depth beneath surface)(e.g. [43, 47]); host rock with different material properties (e.g. [53, 69, 104]). Paper by Holohan et al. [87] presented, probably for the first time, an elastic model, which constrains mechanical causes of oblique-slip faulting from the three-dimensional stress field in the initial elastic phase of subsidence, as it has been observed in nature (e.g., Miyakejima and Dolomieu, [87]).

However, it is important to bear in mind that in all of the above-mentioned cases, formation of ring faults was inferred from the elastic stress field, based on the conditions defined in the beginning of this Section 1.3.1.1. It means that the accurate orientation and shape of the faults (inward-/outward-dipping) cannot be determined; it can be only supposed that in the range of $\alpha \leq$10–15° the faults could be steeply dipping or subvertical. Moreover, elastic models are able to predict the stress distribution in the host-rock only up to initiation of fracturing. However, they are not capable of capturing the stress redistribution associated with generation and propagation of the fractures and thus they cannot reveal the complex fracturing phenomena taking place prior to and during caldera collapse [96].

1.3.1.2 Non-elastic and thermo-mechanical continuum models

The approaches reviewed hereafter utilize various plasticity, damage or fracture models, time-dependent viscoelastic and viscoplastic models, or models accounting for thermal regimes, which may alter crustal rheology and physical properties of the rock, and consequently influence fracture formation and development in the vicinity of the magma chamber. Using these models, researchers investigated the fault location and geometry, and the directions of the potential brittle failure zones around the magma reservoir including the formation and deep geometry of the caldera faults and the relationships between the magmatic system and the surface features of calderas. The main variables are then typically the regional stress fields, magma chamber geometry, and the roof aspect ratio (ratio of the chamber roof thickness to its width).

Komuro et al. [42] investigated the apical caldera collapse as a consequence of a domal deformation, using the elasto-plastic model with von Mises criterion. In paper by Chery et al. [114], the caldera collapse, resurgence of a central dome, and quasi-static evolution of thermally stratified continental crust near both, inflating and relaxating magma chambers were investigated, utilizing elastic-visco-plastic model. Guillou-Frottier et al. [7] utilized elastic-plastic-ductile model, Mohr-Coulomb criterion, and non-linear viscous model to calculate a caldera formation from a pre-defined rectangular magma chamber and the steady-state geotherm without heat transport during the collapse. Burov and Guillou-Frotier [44] used the same approach also for a thermomechanical numerical model using a stationary temperature field with and without a regional extension, and also using a full time-dependent conduction and advection describing the caldera collapse and long-term post-collapse activity, considering the influence of the heat diffusion. Different approach, using elasto-plastic model, von Mises criterion, and Griffith criterion under tensile strength, was chosen in [48] to numerically simulate the formation of cracks under the tensile stresses or increasing magma chamber pressures, including a fracture model that enables to follow the growth of cracks. Folch [47] considered a coupled thermomechanical model in order to find out the conditions for the caldera collapse due to the magma chamber underpressure, with help of the thermoelasticity, Mohr-Coulomb criterion, and Griffith criterion under tensile strength. The quantitative discussion about the relationship between the caldera geometry and the magma chamber depth, which utilizes the elasto-plastic model and the Mohr-Coulomb criterion was presented by Kusumoto and Takemura [103]. Viscoelasticity with linear Maxwell model was employed by Simakin and Ghasemi [54].

Gregg et al. [55] investigated the influence of chamber roof aspect ratio and chamber volume on caldera collapse initiation at both, over- and underpressure, collapse mechanisms. They concluded that the eruptions connected with small chambers (less than 10^2 km^3) are more frequent and less voluminous and eventually cause chamber deflation and collapse. Medium reservoirs (10^2–10^4 km^3) exhibit hindering of the fracture initiation due to the temperature-dependent viscoelastic properties of the host rock. This is in agreement with conclusions of Jellinek and de Paolo [17] who found out that long-term heating of the chamber vicinity makes the rock viscoelastic, thus creeping viscously and absorbing deviatoric stresses causing host rock fracturing. In the case of large chambers (more than 10^4 km^3), even a moderate pressure increment leads to a considerable chamber roof deformation and consequently to a feeder dike formation. Regarding the roof aspect ratio, the authors concluded that for high ratios (more than 2) the chamber roof is rigid enough to withstand relatively high overpressures ($\sim$40 MPa). With decreasing aspect ratio, the damage to the roof becomes crucial and feeder dikes form even at moderate overpressures. It means that large volume and low aspect ratio volcanic systems are the most prone to fault propagation in the chamber roof.

1.3.1.3 Discontinuum-based models

The discontinuum methods consider the treated domains as a set of distinct, interacting elements/particles that are supposed to undergo considerable motion with time. These models solve repeatedly the dynamic equation of equilibrium for each element/particle in the system until the boundary conditions and laws of contact and motion are satisfied. Such an approach makes it possible to treat complex non-linear interaction phenomena between elements/particles. Such models enable to investigate opening/closure of fractures and to take into account sliding along faults [115].

The work by Gray and Monaghan [48] is based on the smoothed particle hydrodynamics method and studies simple two-dimensional configurations. They investigated fracturing around magma chamber and its influence on caldera collapse, they showed that the smoothed particle hydrodynamics formulation of the elastic equations gives satisfactory results for the stress concentration around a circular chamber, and their results are in general agreement with experiments. Holohan et al. [76] employed a distinct element method to show the importance of the magma chamber shape and material properties with respect to the final shape of the caldera. This research complements and improves the work by Hardy [52], who used a discrete element model of a frictional cover undergoing piston-like subsidence at its base, simulating magma chamber deflation and cover collapse. This discontinuum-based approach can be directly compared to analogue models, because the discontinuities are explicitly demonstrated, unlike the continuum-based approaches (elastic, see Section 1.3.1.1 and non-elastic, see Section 1.3.1.2), where incorporating discontinuities is generally possible, but the procedure is often difficult and time consuming. Conclusion of this work is in agreement with works using continuum-based models, as it claims that the features occurring during the caldera collapse are mainly influenced by the chamber geometry, roof aspect ratio, and material properties. In this case, however, the material properties were defined using bulk properties of particle Young's modulus and bond strength.

1.3.2 Stages

Numerical simulations can be also distinguished according to a stage of a volcanological process they aim to capture—before or during the eruption. Pre-eruptive models, focus on the phenomena leading to volcanic eruptions (e.g., a magma chamber rupture, overpressure in the chamber, degasification, mixing, differentiation and cooling). The pre-eruptive models usually take into account several basic scenarios—either the pressure rise in the chamber is caused by a volatile oversaturation due to cooling and crystallization processes [116, 117], or overpressurization originates from the income of fresh magma into the chamber [116, 118], or the eruption is caused by the stress fields around the chamber, its rupture, and dike injection [44, 67].

On the other hand, eruptive models, aim at the physical processes inside the magma chamber, in the conduit, during the magma discharge, and in the atmosphere during the eruption. The listed processes influence mutually each other, however their coupling is a very complex problem. That is why they are in practice usually solved separately, i.e. magma chamber models (pressure evolution inside the chamber), conduit models (a degasification and magma fragmentation along the conduit), and atmospheric models (deposition of the volcanic material).

Even though many of the above-presented models and approaches advanced our knowledge about caldera collapse and its deeper structures, there are still areas which need to be developed. Particularly challenging are coupling of the processes ongoing inside the magma chamber and in the surrounding host rock, and simulation of the effects of regional tectonic stresses, pre-existing faults, and magma flow through fractures connected with the magma chamber [96].

1.4 Magma emplacement

The previous sections, no matter what the phenomena they described, have one common feature—pre-existing chamber represented as an underground cavity containing magma. It is a well-know fact that the Earth has a liquid outer core and, in the scale of a geological time, viscous mantle. Therefore, there must be a way how magma is transported through many kilometers of the overlaying viscous and solid layers and indeed, there are many examples, when silicic magmas reached shallow crustal layers. Geologists came up with several theories of how magma can emplace into these layers.

One of these theories is a diapirism. The diapirism is a subsurface flow of earth materials, which is caused by inverted density stratification. It means that one or more layers of a material with lower density (magma) are initially constrained beneath a material with higher density (wall rock). Due to the density difference, the magma propagates through the wall rock, forming a diapir. Magma emplacement caused by the diapirism is a slow process, which is dependent on the diffusion of heat. The best conditions for diapirism are when the wall rock is very hot and viscous. There were many researchers dealing with a gravitational instability of multi-layer systems, for example [119–126]. After publishing papers of Grout [127] and Ramberg [128, 129], the diapirism became a popular theory explaining the ascent and emplacement of magma. Several numerical analyses [130, 131] and laboratory experiments [132] have proven that after rising a distance of several diameters at a constant low velocity, the diapir attains spherical shape if the diapir is less viscous than the wall rock (which is mostly the case). The heat transfer of such hot spherical diapirs was studied by Marsh [133], Ribe [134], Daly and Raefsky [135], Ansari and Morris [136]. Even though the sphere is a good approximation, especially for the analytical calculations, the shape can be influenced by several factors e.g. syn-tectonic stresses, geometry of the source region, and inhomogeneities in the wall rock [137]. The ascent of magma can originate either from the Rayleigh-Taylor instability (gravitationally unstable configuration of viscous layers) or from a discrete region. The subsequent rising of the diapir is caused by a creeping flow of a wall rock around it [138], which is controlled by a fault or other instability. The crust, in which the diapir is emplaced, can be both syn-tectonic (active) or post-tectonic (inactive) [139–141]. Then, we can distinguish two types of an intrusion—permitted (emplaced into opened cavities [140]) and forceful (sheared or squeezed into place [139]). As an explanation for complex structures in Precambrian terrains, a phenomenon called polydiapirism has been proposed [142–144]. The polydiapirs originate from a multi-wavelength Rayleigh-Taylor instability. However, the diapirism is still a questioned theory, as it has never been conclusively proven that diapirs can reach the shallow crustal layers in a geologically reasonable time [145, 146].

Another theory is a dike intrusion. Magma emplacement via the dike intrusion parts the wall rock along fractures caused by magma or along pre-existing fractures. The wall rock is usually considered to be elastic and there is a relatively small internal deformation while it is pushed apart. A result of this process is a typical shape of the dike with the ratio of thickness to length approximately 1 : 1000 [147]. The deformation occurs almost exclusively within magma rising through the dike. The major influence on the propagation velocity has the magma viscosity. This is an important difference when compared to the diapirs, where the ascent velocity is mostly controlled by the wall rock viscosity. While the diapirism is a relatively slow process ideally taking place in a hot and viscous host rock, the dike intrusion is much faster and occurs in a brittle rock. Therefore the fragments of the wall rock, which fall into the rising magma, may be brought to the surface more easily by the dike intrusion than in the case of the diapirism.

Stoping is another theory that should be mentioned. During the magmatic stoping blocks of disintegrated and spalled roof rock sink through magma as magma mines its way upwards. This phenomenon was firstly described by Goodchild [148] and Lawson [149]. However, this theory was developed to its present state of appreciation by Daly [150–153]. Nowadays, there are no doubts that some plutons were emplaced by stoping. The evidences are undeformed host rock and large xenoliths of a roof rock [154]. Nevertheless, the extent to which it occurs is still not clear.

There are also other mechanisms of the magma emplacement such as an elevation of the overburden, bedrock drop, extension of the surrounding rocks, and lateral translation (along faults).

Chapter 2

Objectives

As discussed in the Chapter 1, there still remain many unresolved issues and controversial explanations of the geological processes associated with formation of volcanic calderas, such as what is the relationship between the three-dimensional geometry of a magma chamber and mechanism of caldera collapse, or how initial construction of a magma chamber will control the caldera development. To bring new views on these topics, a joint research grant project involving both extensive geologic field studies and mathematical modeling and numerical simulations has been carried out between 2012 and 2014 (GAČR P210/12/1385—Calderas as indicators of thermal-mechanical evolution of subvolcanic magma chambers). Research presented in this thesis was initiated as part of the mentioned project and was further extended and developed even after the project was completed. In line with the aims of the project, the thesis addresses the following specific objectives:

- The loci and direction of a ring fault initiation and growth, i.e., whether it propagates from the surface downwards or from the magma chamber upwards,
- The mode of a ring faults propagation, i.e., whether it propagates as shear, or extension fractures,
- The orientation (inward-dipping, vertical, outward-dipping) and sense of shear (normal, reverse) along ring faults,
- Influence of the roof aspect ratio, R, on formation of particular types of fractures to predetermine the subsequent collapse mode,
- Effect of a roofwall transition (rounded blunt edges vs. abrupt bend with a significantly smaller radius) on the fracture propagation.

Chapter 3

Modeling strategy

As discussed in Chapter 1, interaction of hot, inflating-deflating magma chamber and host rock in the upper crust involves complex physical processes involving deformation and failure due to varying magma pressure, heat transfer in various forms and subsequent non-steady thermal field and phase changes, and percolation of hydrothermal fluids. Although formulation of coupled mathematical models for many of these phenomena may be possible, numerical (not to say analytical) solution of the ensuing problem still requires that further simplifications are introduced. Firstly, it may be difficult to quantify experimentally, or even by a qualified estimate, all necessary parameters for the coupled models. Secondly, convergence problems are often encountered when the mathematical models involve multiple sources of nonlinearities and instabilities. Thirdly, numerical simulations involving complex models are very demanding in terms of computational resources and time, which makes analysis of a large number of configurations not feasible. Therefore, appropriate modeling strategy, which takes into accounts only those phenomena which are significant with regards to the analysis objectives, must be adopted. Considering that the present work aims at formation of faults in the vicinity of magma-filled chamber prior to caldera collapse (see Chapter 2), the host rock is idealized as a material-nonlinear solid, while magma is treated as a nearly incompressible fluid. The problem is further simplified by neglecting the thermal effects associated with emplacement of the magma body. The problem then can be efficiently solved by the finite element method—to this end, we used a general-purpose code ADINA [155].

3.1 Geometry

The evidences observed during field studies, such as granitoid plutons in the upper crust that could possibly represent frozen sub-caldera magma chambers, indicate an existence of a large variety of sizes and shapes. The 3D shapes of plutons at depth have been discussed extensively and could be anything from vertically extensive columns (height $\gg$ width) to thin, laterally extensive sill-like bodies (width $\gg$ thickness; e.g., [157–160]). On the other hand, the minimum horizontal dimensions of sub-caldera magma chambers are better constrained and may be best inferred from dimensions of well-exposed calderas (e.g., [1, 161]). They usually do not exceed 20 km in diameter (e.g., [2]) but, at the extreme, some caldera super-eruptions required magma chambers larger than 80-100 km across (e.g., [162, 163]).

3.1.1 Magma chambers

As a compromise, two geometries, which represent the most characteristic shapes of magma chambers seen in the nature, were modeled: (1) sill-like axisymmetric discs, corresponding to tabular magma chambers, with diameters of 10 and 50 km and thickness of 2.5 km, which were fed by a magma conduit, as illustrated in Figure 3.1(a), and (2) axisymmetric cylindrical bodies with vertical sides and horizontal roofs (see Figure 3.1(b)), corresponding to what has been referred to as the "bell-jar" plutons (e.g., [164–166]), also with diameters of 10 and 50 km. To examine the effect of a roofwall transition on the fracture propagation, the tabular bodies had rounded blunt edges whereas the cylindrical bodies had their roofs taking an abrupt bend (with a significantly smaller radius) into the wall. Furthermore, to examine the effect of the overburden, the modeled chambers were placed to depths ranging from shallow-crustal to the base of the upper crust, with the chamber-roof contact at 2.5-10 km below the surface, respectively. Such model setups cover a wide range of possible magma chamber geometries and roof aspect ratios R (where R is chamber roof thickness/chamber diameter).

3.1.2 Axial symmetry

Both types of model setups, with sill-like and bell-jar chamber geometries, were assumed axially symmetric about the vertical axis. The axisymmetric element represents one radian of the structure, and the stiffness, mass, and loads are then defined accordingly. The model was placed in the y-z plane in such a way that z was the vertical (symmetry) axis, y was the horizontal (radial) axis, and x was the angular axis, as illustrated in Figure 3.1. Consequently, ε_{xx} stands for circumferential strain, and shear strains γ_{xy} and γ_{xz} equal to zero. This notation is consistent with the system implemented in the ADINA program, which we used to perform the simulations, and will be used throughout this work.

3.1.3 Overall model size

The dimensions of the host rock domain were chosen large enough to eliminate any boundary effects in the chamber vicinity. Depending on the depth of the magma chamber roof, the height of the model ranged from 30 to 50 km. The radius of the model ranged from 50 to 70 km.

3.2 Material models for magma chamber and host rock

As already mentioned, thermal effects, such as phase transformations, thermal dilatancy, and the temperature-dependence of material parameters were neglected, as well as the magma flow within the chamber as it was considered having minor effect on the host rock failure.

3.2.1 Magma chamber

Kabele et al. [156] investigated performance of different constitutive models representing magma chamber—elastic solid model, elastoplastic solid model, and potential-based fluid model. Even

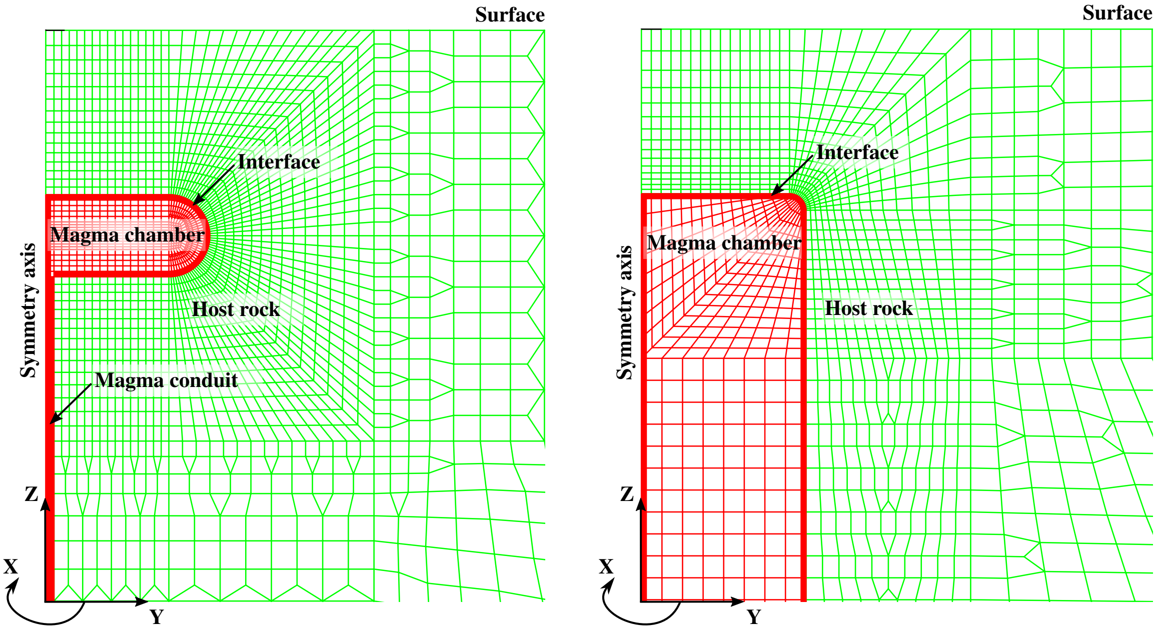

(a) sill-like magma chamber (with a radius of 5 km and a thickness of 2.5 km) emplaced at a depth of 5 km

(b) bell-jar magma chamber (with a radius of 5 km) emplaced at a depth of 5 km

Figure 3.1: Finite element models representing two initial end-member magma chambers emplaced in the upper crust.

though the solid models performed well (considering that many authors omit the magma domain completely, recall Section 1.3.1.1), drawbacks resulting from their solid-material nature are not negligible, e.g., the elastoplastic model offers very limited compressibility as the von Mises yield criterion, which the model follows, preserves volume. Considering the conclusions made in the study, the potential-based fluid model was found as the most plausible and meeting the basic requirements on magma representation.

The potential-based fluid model implemented in ADINA program [155] enables representing fluid as an inviscid, compressible, or almost incompressible medium with no actual flow. As it can be coupled with a solid, the model is suitable for static analysis, where the pressure distribution in the fluid and the displacement and stress distribution in the surrounding structure is of interest. The fluid constitutive model is defined by a slightly compressible relationship between pressure, p, and density, ρ:

$$\frac{\rho}{\rho_0} = 1 + \frac{p}{K} \tag{3.1}$$

where ρ_0 is nominal density and K is bulk modulus. The formulation employs fluid velocity potential to express the continuity and energy/momentum conservation equations. Considering infinitesimal velocities and subsequently quasi-static conditions, the resulting governing equations become linear. In the discretized form, they involve displacements and potential rate as degrees of freedom. For additional details on the model description, the reader is referred to ADINA Theory and modeling guide [155].

3.2.2 Host rock

Brittle fracture of rock is generally associated with tensile and/or shear failure. Kabele et al. [156] examined two different constitutive models representing host rock—fracture model with the Rankine failure condition (covering tensile failure) and plasticity model with the Mohr-Coulomb criterion (covering shear failure). It was concluded that the plasticity model is more appropriate for simulating formation of ring faults and potentially for caldera collapse. It has been also stated in Section 1.3.1.1 that caldera collapse is, among others, conditioned by occurrence of maximum shear stress at the margins of a magma chamber. Moreover, fractures propagate from a chamber upwards in most cases, which implies that employing a model covering shear failure is preferable. Therefore, the plasticity model with the Mohr-Coulomb criterion was chosen for host rock simulation.

The Mohr-Coulomb condition, which is commonly used to simulate shear-driven fracturing of rocks within the theory of plasticity (e.g., [167]), can be written as:

$$|\tau| = c - \sigma \tan \varphi \tag{3.2}$$

where σ is the normal stress, τ is the shear stress, c is the cohesion, and φ is the angle of internal friction. For the future use, it is convenient to express the criterion in terms of the principal stresses:

$$\begin{aligned} F_{\mathrm{MC}} = \frac{m+1}{2} \max\big(&|\sigma_1 - \sigma_2| + q(\sigma_1 + \sigma_2), |\sigma_1 - \sigma_3| + q(\sigma_1 + \sigma_3), \\ &|\sigma_2 - \sigma_3| + q(\sigma_2 + \sigma_3)\big) - \frac{2c\cos\varphi}{1 - \sin\varphi} = 0 \end{aligned} \tag{3.3}$$

where $m = \frac{1+\sin\varphi}{1-\sin\varphi}$ and $q = \sin\varphi$. In this work, the Mohr-Coulomb model followed perfectly plastic yield behavior with non-associative flow rule, and its potential function was defined by the Drucker-Prager criterion:

$$g = \alpha I_1 + \sqrt{J_2} - k \tag{3.4}$$

where I_1 is the first invariant of the stress tensor, and coefficients α and k are determined so that, in the principal stress space, the Drucker-Prager surface is inscribed to the Mohr-Coulomb surface defined by the dilatation angle ψ (for more in-depth information see the ADINA Theory and modeling guide [155]).

The tensile failure was here treated by tension cut-off, T, which improves the ability of the plasticity model to represent rock behavior under tension by defining a limiting surface in the stress space via

$$I_1 - T = 0 \tag{3.5}$$

where I_1 is the first invariant of the stress tensor and $T \geq 0$. The tension cut-off, T, can be estimated as three times the tensile strength of the material [155].

The Mohr-Coulomb model implemented in the ADINA program can be used with the small displacement/small strain and large displacement/small strain formulations. As the large displacement of the magma chamber roof was expected, large displacement/small strain formulation was opted for, implying that a total Lagrangian formulation was employed. In the total Lagrangian formulation, all the static and kinematic variables are referred to the initial (undeformed) configuration at time $t = 0$. The independent variables are then the initial position vector, $\mathbf{X}$, and time, t, and the dependent variable is the displacement $\mathbf{u}(\mathbf{X}, t)$. On the contrary, the updated Lagrangian formulation refers the variables to current (last calculated) configuration, and the independent variables are current position vector, $\mathbf{x}$, and time, t, and the dependent variables are the Cauchy stress $\sigma(\mathbf{x}, t)$ and velocity $\mathbf{v}(\mathbf{x}, t)$.

3.2.3 Magma chamber-host rock interface

Interaction of the potential-based fluid domain with a solid domain was ensured through potential-interfaces, which link the fluid and solid displacement degrees of freedom. A fluid-structure potential interface was placed along the boundary between the fluid and the adjacent solid structure. However, a fluid-rigid wall potential interface was placed along the boundary defined by a contact of the fluid and symmetry axis, as the fluid was required not to flow through the boundary. This boundary condition was modeled by the absence of any interface elements, which was reached by suppressing an automatic generation of the interface elements.

3.2.4 Material parameters

The modeled host rock was represented by rhyolite to consider a magma chamber set in the felsic crust composed of older volcanic edifice, a case which is common, for instance, in continental-margin arc settings. Using Mohr-Coulomb parameters of intact rock would lead to an overestimation of the mechanical performance. Therefore, values of cohesion, c, and friction angle, φ, resulting from testing by Lutz et al. [168], who determined the parameters corresponding to quasi-brittle frictional sliding on the newly formed fracture, were used. Value of dilatation angle, ψ, was derived using an empiric estimate $\psi = 0.666\varphi$ [169], and tension cut-off limit, T, was set as three times tensile strength of the material [155]. All the parameters are listed in Table 3.1.

Table 3.1: Material parameters of the host rock Mohr-Coulomb model.

Young's modulus E [GPa]	Poisson's ratio ν [-]	Density ρ [$\mathrm{kg \cdot m^{-3}}$]	Tension cut-off T [MPa]
80	0.25	2700	9.3
Cohesion c [MPa]	**Friction angle φ [deg]**	**Dilatation angle ψ [deg]**	
3.31	39.6	26.4	

Density, ρ, of the felsic magma was adopted from paper by Bottinga and Weill [170]. Bulk modulus of the magma, K, was derived considering that the magma may have a high gas content (typical of caldera-forming eruptions), thus the value of its Young's modulus, E, was assumed to be one tenth of that of the solid rhyolite, and Poisson's ratio, ν, was considered to be 0.49 to simulate the near-incompressibility of the continuum, while still allowing to use standard FE formulation. The parameters are listed in Table 3.2.

Table 3.2: Material parameters of the magma potential-based fluid model.

Bulk modulus K [GPa]	Density ρ [$\mathrm{kg} \cdot \mathrm{m}^{-3}$]
133.33	2200

3.3 Boundary conditions and loading

The boundary conditions were defined to plausibly simulate a real volcanic system and to diminish an influence of the model boundaries. Radial displacements along the symmetry axis and along the outer vertical boundary of the host rock domain were fixed. Vertical displacements were constrained along the horizontal bottom edge, and the upper edge was traction-free.

Loading was applied in three stages. First, a self-weight due to gravity acceleration of $10\ \mathrm{m} \cdot \mathrm{s}^{-2}$ was applied. At the same time, a magma chamber was slightly inflated to counteract deformation induced by the gravity load, which would otherwise result in undesirable initial stress state and deformation of the chamber roof. During the second stage, positive excess pressure was applied to the magma chamber causing its inflation. This stage represented fresh magma injection through a magma conduit to the chamber and was terminated once a localized zone of maximum plastic shear strain, interconnecting the chamber and surface, reached minimum value of 0.01. Such a localized zone can be considered as a potential site for development of a feeder dike causing a magma depletion and consequent depressurization of the chamber, which was the final stage. The chamber was gradually deflated until the onset of roof collapse due to underpressure.

In the loading cycle described above, it is assumed that the initial overpressurization of the chamber is terminated by eruption of magma through the dikes, which, however, does not lead to the caldera collapse. The collapse is then attributed to depressurization of the chamber. However, as we reviewed in Section 1.1, some authors argue against this mechanism and pursue the hypothesis that calderas form by explosive failure of the roof in response to high overpressure in the chamber at the moment of the collapse. The stress field conditions leading to the formation of ring faults are achieved prior to initiation of the eruption, when an overpressurized magma chamber is loaded by magmatic regional doming or subjected to regional extension. Therefore, a scenario leading to the overpressure collapse mechanism was also investigated for all the modeled configurations. The first stage was identical with the previous scenario, but in the second stage, the chamber was gradually inflated until the roof was unable to sustain any more increase of the chamber overpressure. This state manifested itself by notable reduction of the rate at which the chamber pressure was increasing with constant influx of magma and, eventually, inability to reach convergence of the nonlinear solution. The overpressure scenario could take place if feeder dikes either were not formed at all, or were not able to release sufficient amount of the overpressure. It should be noted that the deflation stage followed the inflation stage representing a single inflation-deflation cycle, whereas the maximum inflation stage was independent of the previous stages and started from an initial equilibrated state of the system. In the case of the vertically prolonged bell-jar chambers, the inflation led to an excessive radial deformation along the vertical chamber boundary and loss of convergence before significant deformations of the magma chamber roof could have been manifested. Therefore, the inflation stage when a feeder dike occurred was also the maximum reached inflation. The individual loading stages for both, under- and overpressure scenarios, can be observed in Figure 3.2, where a development of magma pressure in time is documented for a sill-like chamber. The pressure, measured in MPa, is evaluated within a fluid element on the roof-chamber contact.

It is noted that the overburden due to deposition of the erupted material was neglected in both scenarios.

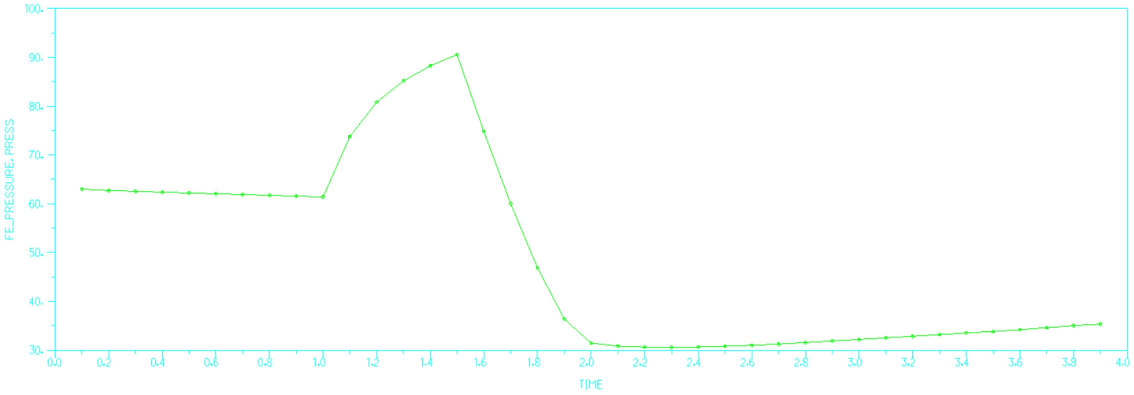

(a) underpressure scenario

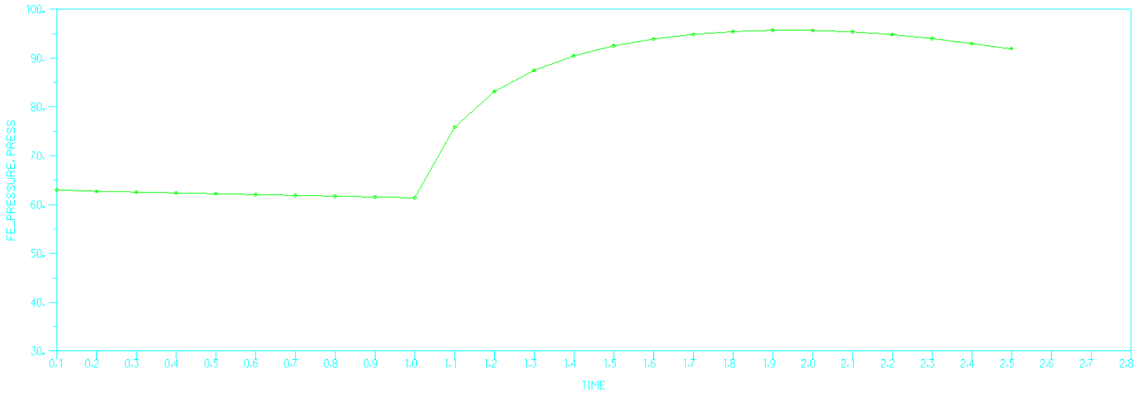

(b) overpressure scenario

Figure 3.2: Development of magma pressures in time.

In the model, the magma chamber pressurization was induced via a distributed potential flux prescribed at the bottom of the magma domain (representing magma inflow into a conduit feeding the chamber). Positive flux represented mass flowing into the fluid domain. The reduction of magma volume was simulated by applying the same flux magnitude, but with the opposite sign. It is noted that the induced pressure changes are uniform throughout the fluid domain. The flux can be prescribed directly onto potential-based fluid elements and is defined as unit mass flowing through unit area.

3.4 Finite element discretization

The analyzed domain was discretized by four-node quadrilateral and three-node triangular finite elements. The typical size of the finite elements assigned to the host rock near the magma chamber was 230 m, and a coarser mesh was used farther from the chamber, as shown in Figure 3.1. The large elements are a consequence of model dimensions with height ranging from 30 to 50 km and a radius ranging from 50 to 70 km. The dimensions of the host rock domain were chosen large enough to eliminate any boundary effects in the chamber vicinity. The typical element size of the magma domain was also 230 m to preserve the regularity of the mesh in a transition zone from magma to the host rock.

Chapter 4

Results

In order to investigate the effects of the shape, size, and depth of the magma chamber on the fracturing processes in the roof and neighboring host rock, several tens of cases were modeled and analyzed employing finite element method. In this chapter, we introduce an overview of the analyzed cases and provide reasoning for their selection. We also explain, in detail, the methodology adopted for interpretation of the calculation results (displacement, strain, and strain fields) in terms of geological phenomena and mechanisms. The present chapter sets the ground for the subsequent Chapter 5, where the results of calculations will be discussed and generalized from the geologic point of view. Kindly note that throughout this thesis, the positive sense of deformation is considered as tension and the negative as compression, and σ_1 is the maximum principal stress (tension or least compression) and σ_3 is the minimum principal stress (largest compression).

4.1 Analyzed configurations

The modeled cases covered a wide range of possible magma chamber types, geometries, and roof aspect ratios, but only 12 most representative ones (i.e., those providing unique results) are discussed hereafter and listed in Table 4.1. Next to the chamber and roof dimensions, also ratios comparing roof thickness to chamber diameter and roof thickness to chamber depth were evaluated. The former ratio is generally recognized as a threshold value dividing different collapse modes, and the latter ratio was introduced in this work to complement evaluation possibilities.

4.2 Results interpretation

The ADINA program generates a wide variety of results, e.g., stresses, displacements, reactions, fluxes. Hereafter, these results are interpreted by relating them to geological phenomena. Please recall that the ADINA program considers positive sense of deformation as tension and the negative as compression.

For the purposes of this work, three strain quantities were analyzed and plotted to the de-

Table 4.1: List of modeled cases and their dimensions. Case notations are composed from a letter denoting type of chamber geometry (S—sill-like and B—bell-jar) and two numbers standing for chamber diameter/roof thickness.

Chamber type	Case	Chamber diameter d [km]	Roof thickness t [km]	Chamber depth h [km]	Roof aspect ratio $R = \frac{t}{d}$ [-]
Sill-like	S-10/1.25	10.0	1.25	2.5	0.125
	S-10/2.5	10.0	2.5	2.5	0.25
	S-10/5	10.0	5.0	2.5	0.5
	S-10/7.5	10.0	7.5	2.5	0.75
	S-10/10	10.0	10.0	2.5	1.0
	S-50/5	50.0	5.0	2.5	0.1
	S-50/7.5	50.0	7.5	2.5	0.15
	S-50/10	50.0	10.0	2.5	0.2
Bell-jar	B-10/5	10.0	5.0	-	0.5
	B-10/10	10.0	10.0	-	1.0
	B-50/5	50.0	5.0	-	0.1
	B-50/10	50.0	10.0	-	0.2

formed outline of the domains in order to thoroughly describe the fracturing processes taking place in the host rock during inflation and deflation of a magma chamber. Since the Mohr-Coulomb model is based on the theory of plasticity, it does not explicitly treat fractures as discontinuities in the displacement field. Instead, fracturing phenomena are represented by means of plastic strain. However, the model is capable of predicting zones of localized plastic deformation, which can be interpreted as potential sites of initiation, propagation, and displacement of ring faults. Therefore, to capture fractures plausibly, only the plastic (irreversible) parts of the strains were taken into account. Namely, the analyzed quantities were: (1) the circumferential plastic normal strain, $\varepsilon^{\mathrm{p}}_{\mathrm{xx}}$, (2) the maximum plastic shear strain in the radial plane, $\gamma^{\mathrm{p}}_{\mathrm{max}}$, and (3) the principal plastic strains in the radial plane $\varepsilon^{\mathrm{p}}_{1,2}$, and their direction. The plots of the named quantities obtained by the FE calculations for all the evaluated cases and loading scenarios are depicted in the Appendix.

4.2.1 Circumferential plane

The circumferential plastic normal strain, $\varepsilon^{\mathrm{p}}_{\mathrm{xx}}$ is defined as:

$$\varepsilon^{\mathrm{p}}_{\mathrm{xx}} = \varepsilon_{\mathrm{xx}} - \varepsilon^{\mathrm{e}}_{\mathrm{xx}} = \varepsilon_{\mathrm{xx}} - \frac{1}{E}(\sigma_{\mathrm{xx}} - \nu\sigma_{\mathrm{yy}} - \nu\sigma_{\mathrm{zz}}) \tag{4.1}$$

where $\varepsilon_{\mathrm{xx}}$ is a circumferential total normal strain, $\varepsilon^{\mathrm{e}}_{\mathrm{xx}}$ is the elastic part a circumferential total normal strain, E is Young's modulus, ν is Poisson's ratio, and σ_{xx}, σ_{yy}, and σ_{zz} are normal stresses in directions denoted by their subscripts. This quantity was employed to capture sites of tension-induced radial fracturing, as illustrated in Figure 4.1. Radial fractures can occur on the surface (in a case of roof resurgence), but also on the roof-chamber contact (during the roof subsidence).

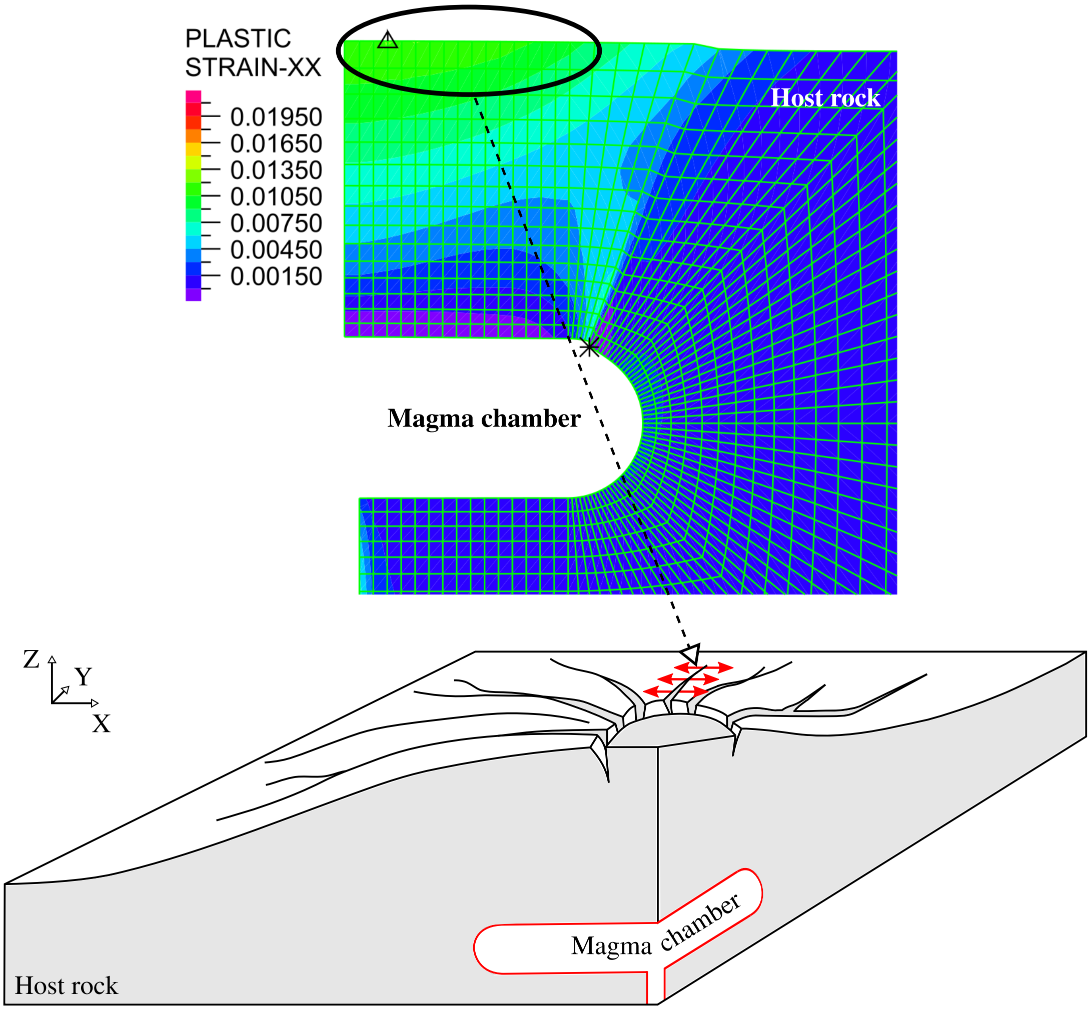

Figure 4.1: Interpretation of the circumferential plastic normal strain, $\varepsilon^{\mathrm{p}}_{\mathrm{xx}}$, as radial fracturing.

4.2.2 Radial plane

4.2.2.1 Plastic deformation quantities

The maximum plastic shear strain in the radial plane, $\gamma^{\mathrm{p}}_{\mathrm{max}}$, was the crucial quantity, as the Mohr-Coulomb model is primarily captures shear-driven fracturing of rocks. The quantity is calculated as:

$$\begin{gathered} \frac{\gamma^{\mathrm{p}}_{\mathrm{max}}}{2} = \sqrt{\left(\frac{\varepsilon^{\mathrm{p}}_{\mathrm{yy}} - \varepsilon^{\mathrm{p}}_{\mathrm{zz}}}{2}\right)^2 + \left(\frac{\gamma^{\mathrm{p}}_{\mathrm{yz}}}{2}\right)^2} \\ \text{and the rotation angle is} \\ \tan 2\theta_{\gamma^{\mathrm{p}}_{\mathrm{max}}} = -\left(\frac{\varepsilon^{\mathrm{p}}_{\mathrm{yy}} - \varepsilon^{\mathrm{p}}_{\mathrm{zz}}}{\gamma^{\mathrm{p}}_{\mathrm{yz}}}\right) \end{gathered} \tag{4.2}$$

where $\varepsilon^{\mathrm{p}}_{\mathrm{yy}}$ and $\varepsilon^{\mathrm{p}}_{\mathrm{zz}}$ are plastic normal strains in directions denoted by their subscripts, and $\gamma^{\mathrm{p}}_{\mathrm{yz}}$ is plastic shear strain in y-z (radial) plane. All these plastic strains are derived analogically to equation 4.1, i.e., $\boldsymbol{\varepsilon}^{\mathrm{p}} = \boldsymbol{\varepsilon} - \boldsymbol{\varepsilon}^{\mathrm{e}} = \boldsymbol{\varepsilon} - \mathbf{C}\boldsymbol{\sigma}$ where $\boldsymbol{\varepsilon}$, $\boldsymbol{\varepsilon}^{\mathrm{e}}$, and $\boldsymbol{\varepsilon}^{\mathrm{p}}$ are the strain tensors, $\mathbf{C}$ is the compliance tensor for axial symmetry, and $\boldsymbol{\sigma}$ is the stress tensor. However, the maximum plastic shear strain, $\gamma^{\mathrm{p}}_{\mathrm{max}}$, localized at locations, which were obviously exposed to different types of loading. It implies that analyzing this quantity alone is not sufficient for a proper assessment of fracturing modes. Therefore, in addition to $gamma_max^p$, the principal plastic strains in the radial plane, $\varepsilon^{\mathrm{p}}_{1,2}$, were examined as a complementary quantity. The principal plastic strains and their direction is determined as:

$$\begin{aligned} &\varepsilon^{\mathrm{p}}_{1,2} = \frac{\varepsilon^{\mathrm{p}}_{\mathrm{yy}} + \varepsilon^{\mathrm{p}}_{\mathrm{zz}}}{2} \pm \sqrt{\left(\frac{\varepsilon^{\mathrm{p}}_{\mathrm{yy}} - \varepsilon^{\mathrm{p}}_{\mathrm{zz}}}{2}\right)^2 + \left(\frac{\gamma^{\mathrm{p}}_{\mathrm{yz}}}{2}\right)^2} \\ &\text{and the principle rotation angle is} \\ &\tan 2\theta^{\mathrm{p}} = \frac{\gamma^{\mathrm{p}}_{\mathrm{yz}}}{\varepsilon^{\mathrm{p}}_{\mathrm{yy}} - \varepsilon^{\mathrm{p}}_{\mathrm{zz}}} \end{aligned} \tag{4.3}$$

where all the quantities have been defined in the previous paragraph.

4.2.2.2 Localized fracturing

Shape of dikes and/or ring faults can be associated with zones of localized maximum plastic shear strain interconnecting the chamber and surface, illustrated in Figure 4.2. However, the mode of their displacement, i.e., whether they behave as shear or extension fractures, was unclear. Therefore, the information provided by the iso-band plot of maximum plastic shear strain was complemented by the vector plot of principal plastic strains, which allowed us to distinguish and two fracturing mode.

The first mode is characterized by a negligible magnitude of the minimum (compressive) principal plastic strain, while the maximum (tensile) one is prevailing and is perpendicular to the fracture. This mode is described as a localized extension fracturing.

The other mode is typical by principal strains having similar magnitudes and direction at about 45° with respect to fracture orientation. This mode is denoted as a localized shear fracturing, see 4.3. The scheme in the right bottom corner of the Figure also represents a normal fault—shearing along the fracture, when the hanging wall moves downwards relative to footwall. The other sense of shearing is a reverse fault, where the hanging wall moves up relative to the footwall.

4.2.2.3 Multiple fracturing

Next to the localized zones of the maximum plastic shear strain, smeared zones, which could not be interpreted as neither of the previous fracturing modes, were observed in some calculated cases, occurring, for example, in the vicinity of the symmetry axis on the top and bottom surfaces of the magma chamber roof.

A pattern of the principal plastic strain vectors in the smeared zone close to the top surface of the chamber roof during the deflation stage resembled the vector pattern at the tensile fracturing. However, the tensile fracturing was not presumable in this case considering the location

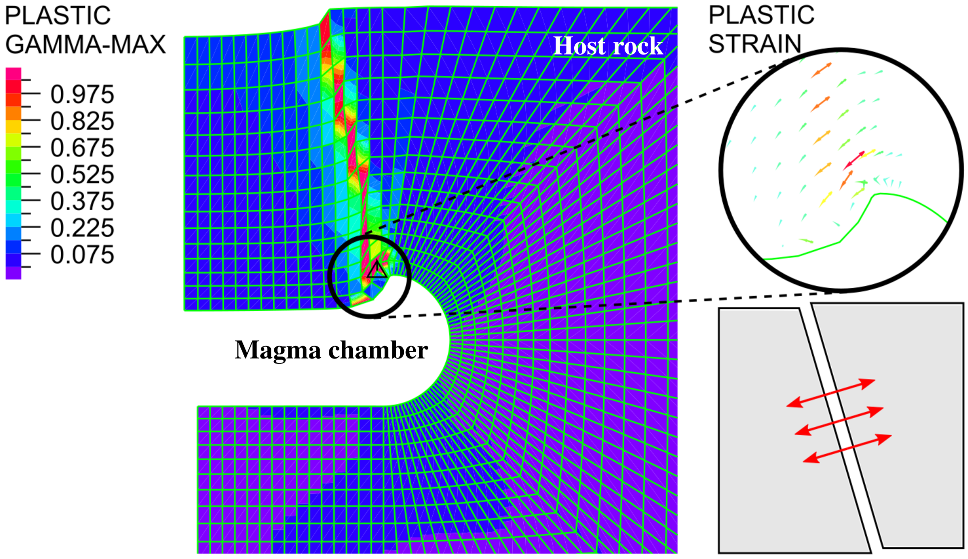

Figure 4.2: Scheme of the localized extension fracturing mode with the plots of maximum plastic shear strain (denoted as PLASTIC GAMMA-MAX) and prevailing vectors of tensile principal plastic strain (denoted as PLASTIC STRAIN) perpendicular to the fracture.

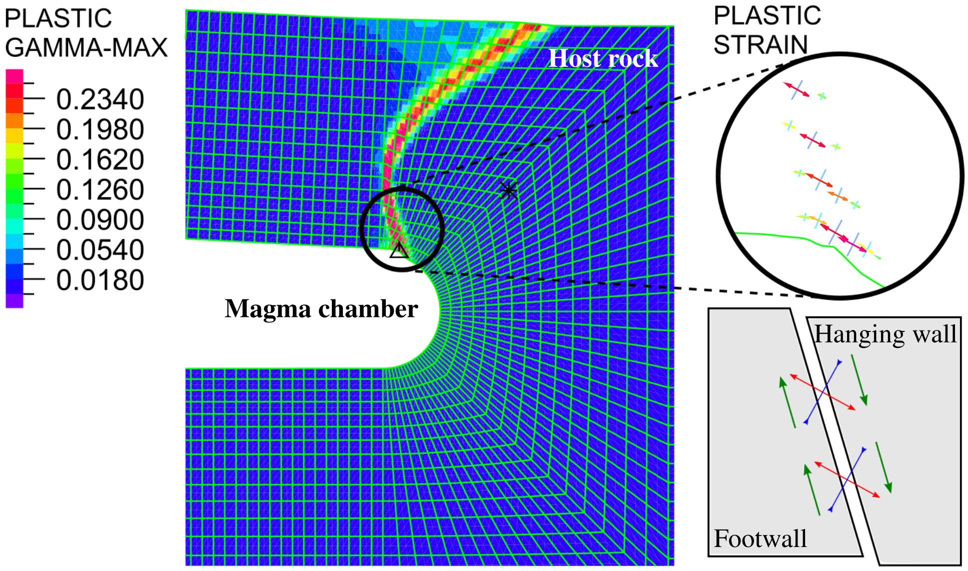

Figure 4.3: Scheme of the localized shear fracturing mode with the plots of maximum plastic shear strain (denoted as PLASTIC GAMMA-MAX) and principal plastic strain vectors of similar magnitudes (denoted as PLASTIC STRAIN) rotated by 45° with respect to fracture orientation. The scheme in the right bottom corner also represents a normal fault (as opposed to reverse fault).

and the stress state—significant principal compression in two directions (approximately in the horizontal (x-y) plane) and relatively low principal compression in the third (nearly vertical) direction due to self-weight, as shown in Figure 4.4. Hence, we inspected the non-associative plastic flow vector for the given stress state, as shown in Figure 4.6, point 1). It is seen that the largest and the only positive (extensive) component of the flow vector corresponds to the least compressive stress σ_1. As illustrated in Figure 4.4, the fractured rock mass contracts in direction of the largest compression (σ_2, σ_3) while it extends in the direction of the least compression σ_1. This behavior can be explained by presence of numerous randomly oriented fractures in the rock mass, sliding of which causes the dilation in the least confined direction. We call this mode multiple fracturing under high confinement.

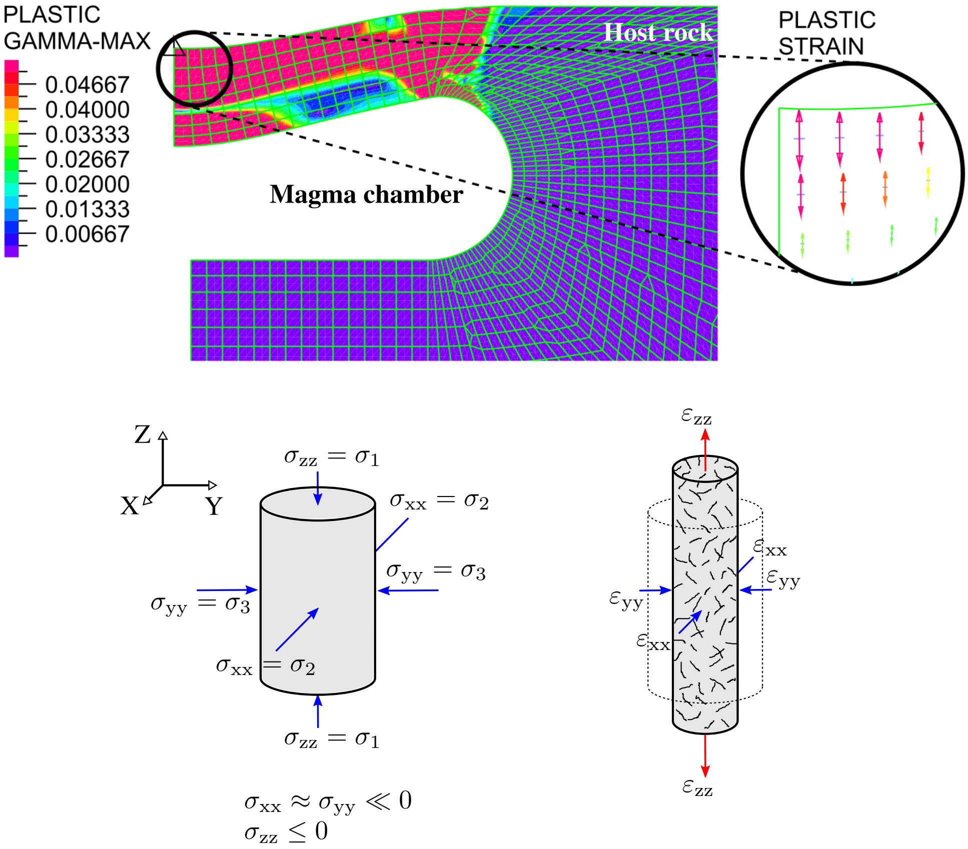

Figure 4.4: Scheme of the multiple fracturing under high confinement mode with the plots of maximum plastic shear strain (denoted as PLASTIC GAMMA-MAX) and prevailing vectors of tensile principal plastic strain (denoted as PLASTIC STRAIN).

On the other hand, the principal plastic strain vectors in the smeared zone close to the bottom surface of the chamber roof during the deflation stage had the similar magnitudes as in the case of the shear fracturing. However, the shear fracturing was not likely in this location and the stress state—relatively low principal compression in two directions (approximately in the horizontal (x-y) plane) and significant principal compression in third (nearly vertical) direction due to self-weight, see Figure 4.5. For this reason, we inspected the non-associative plastic flow vector for the given stress state, as illustrated in Figure 4.6, point 2). It is seen that all the three components of the flow vector had similar magnitudes, and the only negative (compressive) component of the flow vector corresponds to the most compressive stress σ_3. As illustrated in Figure 4.5, the fractured rock mass extends in direction of the least compression (σ_1, σ_2) while it contracts in the direction of the largest compression σ_3. This behavior can be again explained by presence of numerous randomly oriented fractures in the rock mass, sliding of which causes the contractin in the most confined direction. We call this mode multiple fracturing under low confinement.

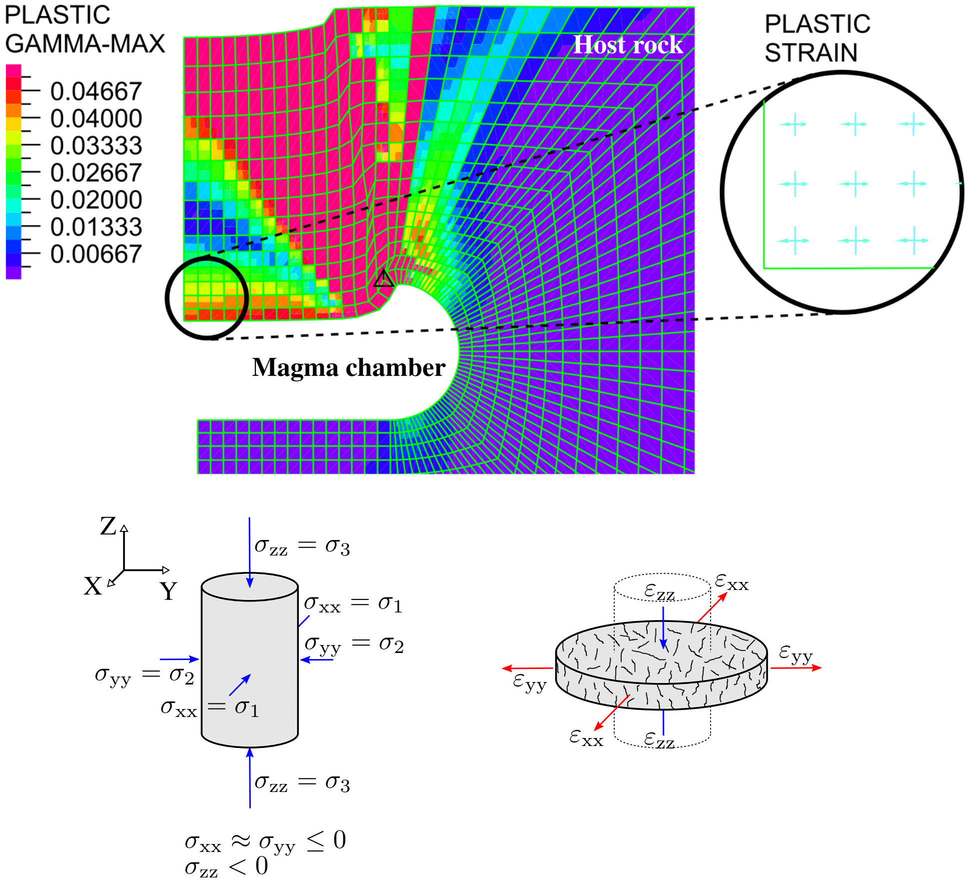

Figure 4.5: Scheme of the multiple fracturing under low confinement mode with the plots of maximum plastic shear strain (denoted as PLASTIC GAMMA-MAX) and principal plastic strain vectors of similar magnitudes (denoted as PLASTIC STRAIN).

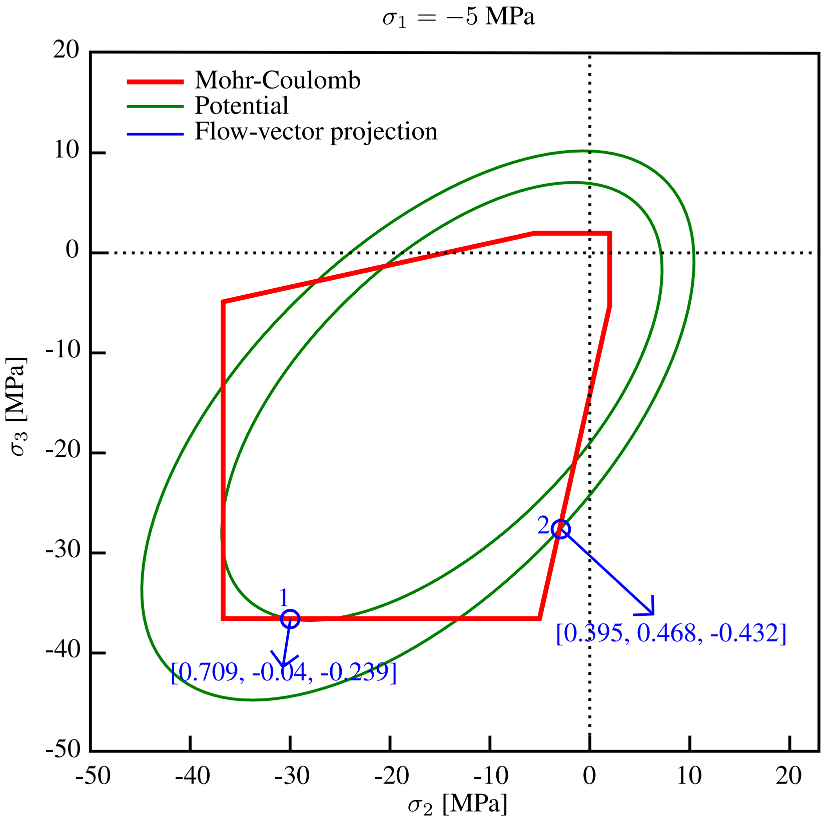

Figure 4.6: Graphical representation of Mohr-Coulomb yield function and plastic flow potential with projections of plastic flow vectors corresponding to the stress states of the multiple fracturing under high and low confinements.

Chapter 5

Discussion

The approach presented in this thesis predicts specific fracture orientations and localization, providing new views into the formation of calderas and related structures. It has been well established that major faults in nature form through reactivation and linkage of small-scale fractures (e.g., [171–173]). Hence, the zones of intense circumferential fracturing can be viewed as potential sites where the ring fault will localize. The position, orientation, and extent of the fractured domains around the chamber can be used to infer the general modes of downward roof-rock transport into the underlying magma, whether by piston subsidence/resurgence (for underpressure/overpressure scenarios) where the whole roof slides as a coherent block, or by magmatic stoping where the roof is dismembered into numerous smaller fracture-bounded blocks which can then incorporate into the magma. It is shown that these different roof failure modes are also related to the roof aspect ratio, curvature of the roof/wall transition, and pressure fluctuations within the chamber. Assuming that melts or hydrothermal fluids will be preferentially driven into the most intensely fractured, and thus the most permeable regions, the modeled fracture bands indicate the likely location and orientation of vents, radial dikes, ring dikes, cone sheets, and hydrothermal veins. The presented models can thus also predict location and progressive development of epithermal laccolith-caldera-related ore deposits.

The results generated by the FE calculations (all of them are presented in Appendix) were analyzed and interpreted as described in Section 4.2. The analysis outcomes were graphically summarized to schematic figures, which were drawn to deformed outlines of the magma chamber and host rock (without magnification). The figures display domains of radial fractures in a form of blue bands, while domains of multiple fracturing under high and low confinements and circumferential fractures (shear or dilation) in a form of yellow bands. The localized zones of the maximum plastic shear strain, representing potential sites for development of fractures/ring dikes and/or ring faults, are depicted as an orange/gray thick line—the orange thick line with arrowheads oriented upwards represents a part of the fracture propagating from a chamber, and the gray thick line with arrowheads oriented downwards represents a part of the fracture propagating from a surface, see, e.g., Figure 5.5. The thick lines are complemented by couples of arrows—the couple of arrows perpendicular to the line stands for the extension fracturing mode, and the couple of arrows parallel with the line describes the shear fracturing mode. The orientation of the parallel arrows also defines a sense of shearing (normal of reverse faults, recall the Section 4.2.2.2). The positions of the arrow couples approximately correspond to a location where the fracturing mode they describe prevails, and their sizes reflect an intensity of the fracturing mode they describe. Kindly note that the fracturing domains and localized zones developed in the inflation stage are not redrawn to figures describing the deflation stage, i.e., only newly developed structures are taken into account. Cases listed in the following sections are ordered with respect to roof aspect ratio, R, from the lowest to the highest value. The discussed fracturing processes are summarized in Table 5.1.

5.1 Tabular sill-like magma chambers

For each modeled case of the sill-like magma chamber, there are three schematic figures describing: (a) the inflation stage until a potential site for development of a feeder dike occurred, (b) the deflation stage till the onset of a roof collapse due to underpressure, and (c) the maximum inflation stage till the onset of a roof collapse due to overpressure. It should be noted that the deflation stage followed the inflation stage representing a single inflation-deflation cycle, whereas the maximum inflation stage was independent of the previous stages and started from an initial equilibrated state of the system.

Case S-50/5

During inflation, a large chamber (diameter 50 km) at intermediate depth (5 km), see Figure 5.1(a), produces a (sub)vertical damage zone of circumferential hybrid (shear and dilation) fractures propagating from the chamber margin, thus defining a potential site for development of a ring fault. However, after rising about 1/2 of roof height, the zone deviates sideways from the symmetry axis and passes into a near-surface zone of multiple fracturing under high confinement propagating from the surface. Also a near-surface flat domain of radial fractures expands above the center of the chamber. During the deflation stage, shown in Figure 5.1(b), the potential (sub)vertical ring fault turns into an outward-dipping reverse ring fault propagating from the chamber to the surface. Beneath the surface, a domain of multiple fracturing under high confinement expands above the center of the chamber, while a flat subtle zone of radial fractures occurs on the chamber/roof contact above the chamber center. The underpressure scenario would lead to an outward-dipping piston subsidence and collapse.

The maximum inflation stage, illustrated in Figure 5.1(c), is almost identical as the inflation stage, just the domain of radial fractures expands sideways from the symmetry axis and intersects the fractured domain above chamber margin. Also a domain of multiple fracturing under low confinement expands above the center of the chamber downwards and sideways approximately to halves of chamber radius and roof height. The overpressure scenario would result in an inward-dipping piston resurgence and collapse.

Case S-10/1.25

The inflation stage of a mid-size chamber (diameter 10 km) at very shallow depth (1.25 km), illustrated in Figure 5.2(a), generates a band of inward-dipping, circumferential hybrid (shear and dilation) fractures propagating upwards from the edge of the magma chamber and intersecting with a downward propagating domain of multiple fracturing under high confinement,

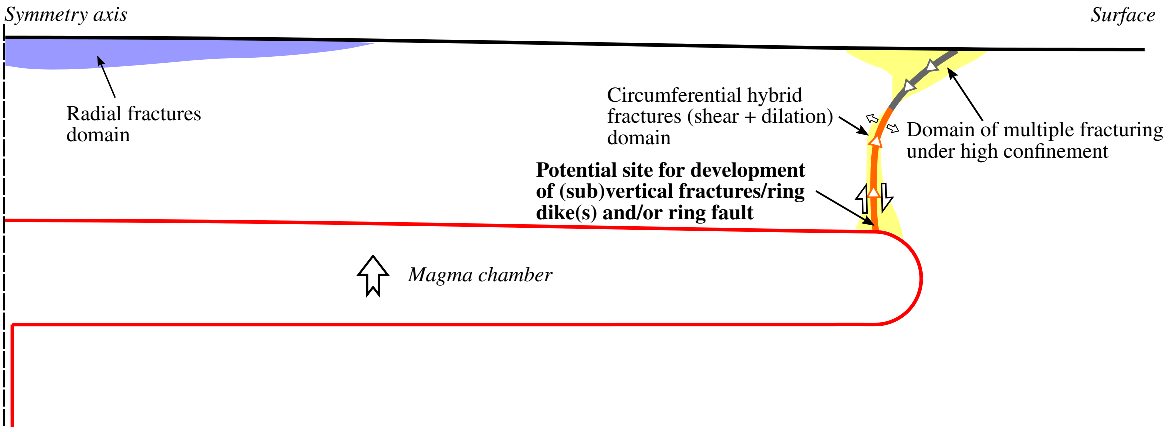

(a) inflation stage, until a potential site for development of a feeder dike occurred

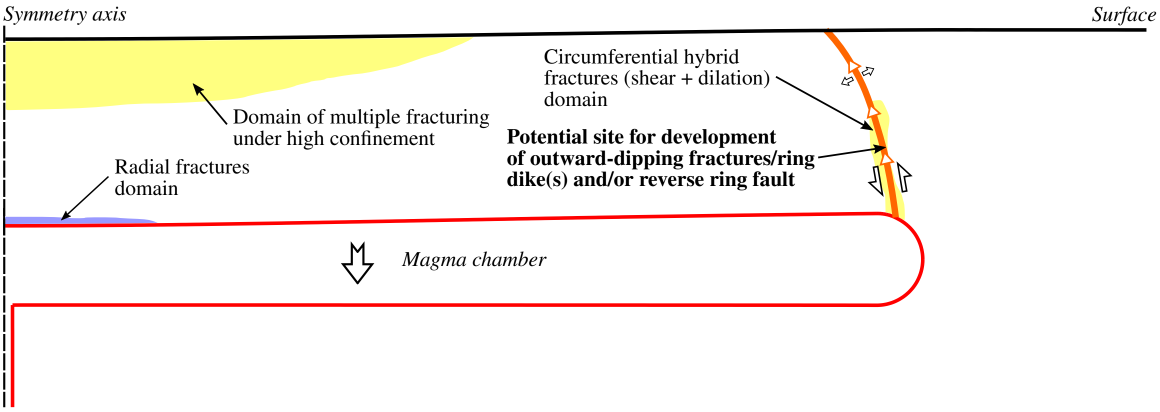

(b) deflation stage, till the onset of a roof collapse due to underpressure

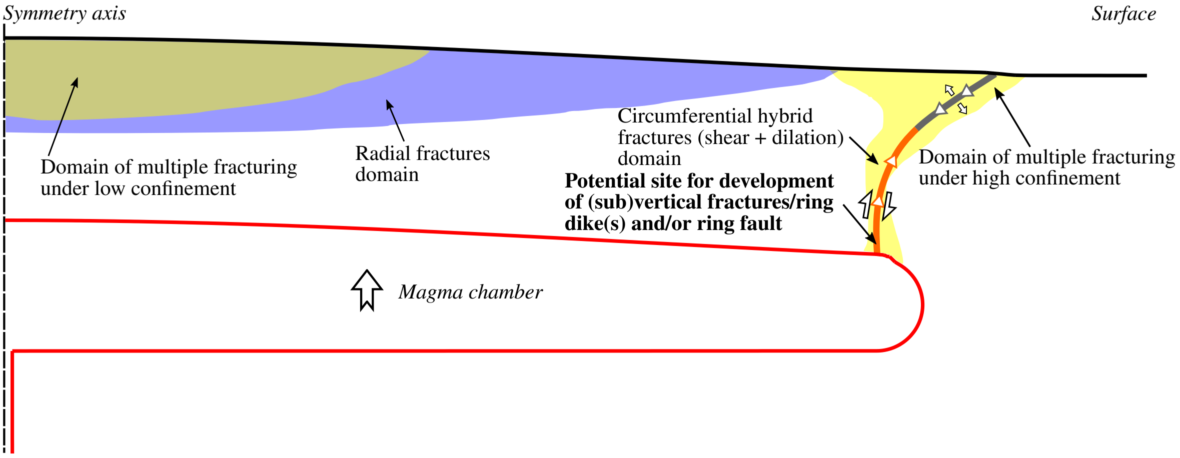

(c) maximum inflation stage, till the onset of a roof collapse due to overpressure

Figure 5.1: Schematic figures for a sill-like magma chamber with 50 km in diameter and 5 km beneath the surface at different loading stages (Case S-50/5).

thus indicating a potential site for development of a reverse ring fault. A radial fractures domain expands above the center of the chamber downwards and sideways, with the intensity of fracturing and magnitude of dilation being the largest close to the symmetry axis. In turn, during the deflation stage, shown in Figure 5.2(b), the most intense radial fracturing concentrates along the chamber-roof contact and is complemented by a domain of multiple fracturing under low confinement, while a domain of multiple fracturing under high confinement develops close to the surface. The potential site for development of reverse ring fault switches from inward- to outward-dipping and migrates from the chamber margin at an angle of about 45° towards the region of the maximum surface subsidence. Also a steeply-dipping tensile fracture above the chamber margin (in a place of largest surface curvature) propagates from the surface downwards. The underpressure scenario would lead to a downsag subsidence and collapse.

The maximum inflation stage, see Figure 5.2(c) evinces almost identical fracturing modes as the inflation stage, only the upper part of the chamber roof displays a broad domain of multiple fracturing under low confinement. The overpressure scenario would result in an inward-dipping piston resurgence and collapse.

Cases S-50/7.5 and S-50/10

For the sake of completeness, also two cases of deep-seated (7.5 and 10 km) large chambers (diameter 50 km) are examined, though enormous, and possibly unrealistic, magma overpressures would be necessary to develop feeder dikes without addition of tectonic forces. However, both cases, depicted in Figures 5.3(a) and 5.4(a), evince identical behavior in all stages. The inflation stages produce a (sub)vertical damage zones of circumferential hybrid (shear and dilation) fractures propagating from the chamber margins. After rising about 2/3 of roof height, the zones deviate sideways from symmetry axes and pass into a near-surface zones of multiple fracturing under high confinement propagating from the surfaces. Also flat domains of radial fractures expand above the center of the chamber. The only fractures occurring during the deflation stages, shown in Figures 5.3(b) and 5.4(b), are near-surface domains of multiple fracturing under high confinement expanding above the center of the chamber. The underpressure scenarios would not lead to any subsidence and/or collapse.

The maximum inflation stages, illustrated in Figures 5.3(c) and 5.4(c), are almost identical as the inflation stages, just the domains of radial fractures expand sideways from the symmetry axes and intersect the fractured domain above chamber margin. Also domains of multiple fracturing under low confinement expand above the center of the chamber downwards and sideways approximately to halves of chamber radius and roof height. The overpressure scenarios would result in an inward-dipping piston resurgence and collapse.

Case S-10/2.5

During the inflation of a mid-size chamber (diameter 10 km) at shallow depth (2.5 km), depicted in Figure 5.5(a), domains of radial fractures and multiple fracturing under low confinement develop. Both domains spread above the center of the chamber downwards and sideways, with the intensity of fracturing being the largest close to the symmetry axis. Also a band of inward-dipping, circumferential hybrid (shear and dilation) fractures is seen to propagate up-

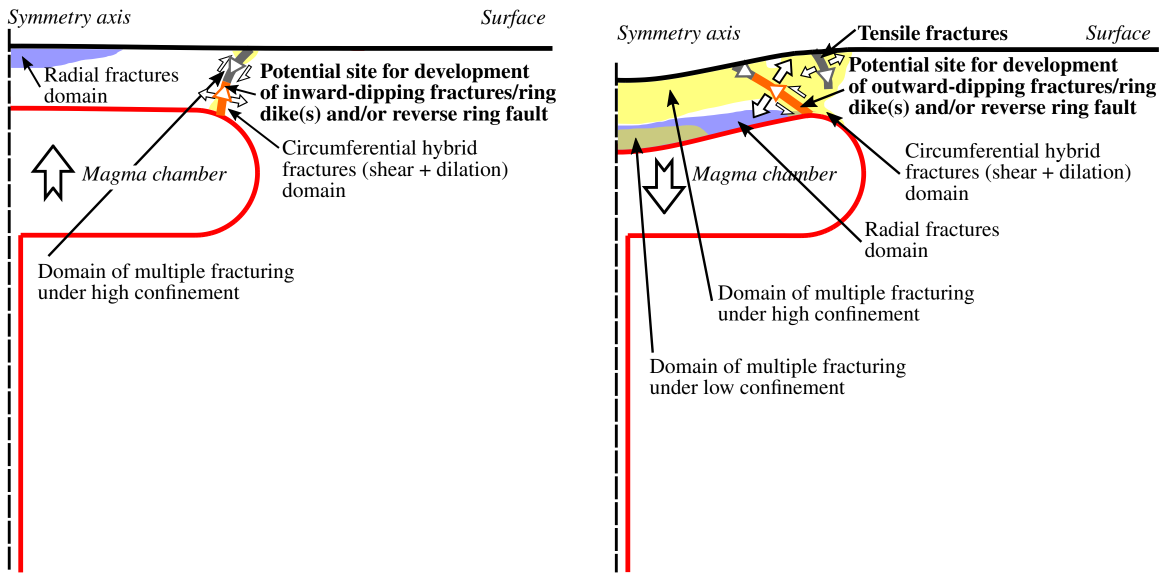

(a) inflation stage, until a potential site for development of a feeder dike occurred

(b) deflation stage, till the onset of a roof collapse due to underpressure

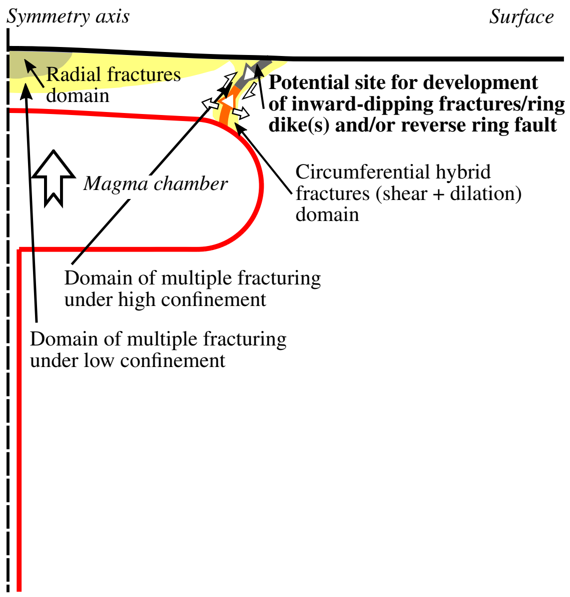

(c) maximum inflation stage, till the onset of a roof collapse due to overpressure

Figure 5.2: Schematic figures for a sill-like magma chamber with 10 km in diameter and 1.25 km beneath the surface at different loading stages (Case S-10/1.25).

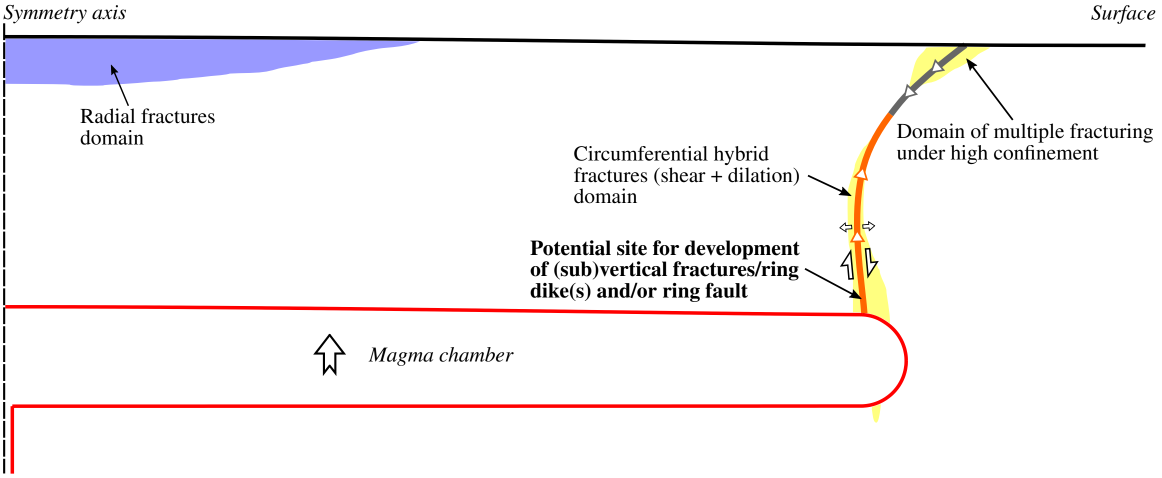

(a) inflation stage, until a potential site for development of a feeder dike occurred

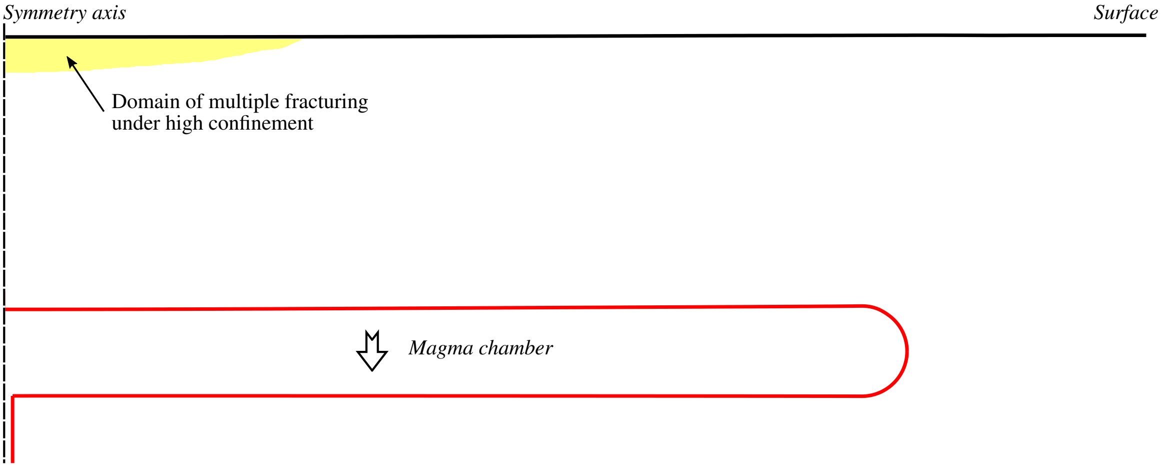

(b) deflation stage

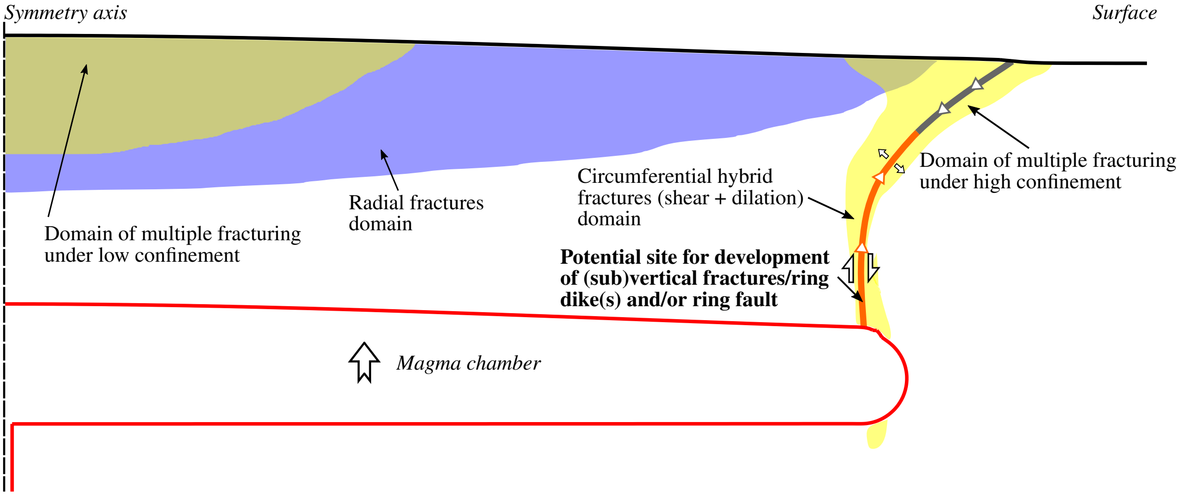

(c) maximum inflation stage, till the onset of a roof collapse due to overpressure

Figure 5.3: Schematic figures for a sill-like magma chamber with 50 km in diameter and 7.5 km beneath the surface at different loading stages (Case S-50/7.5).

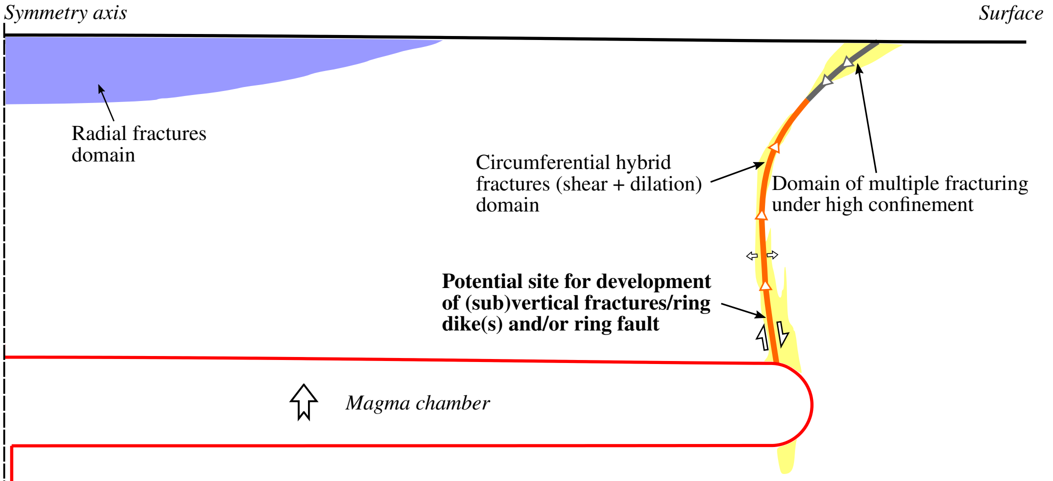

(a) inflation stage, until a potential site for development of a feeder dike occurred

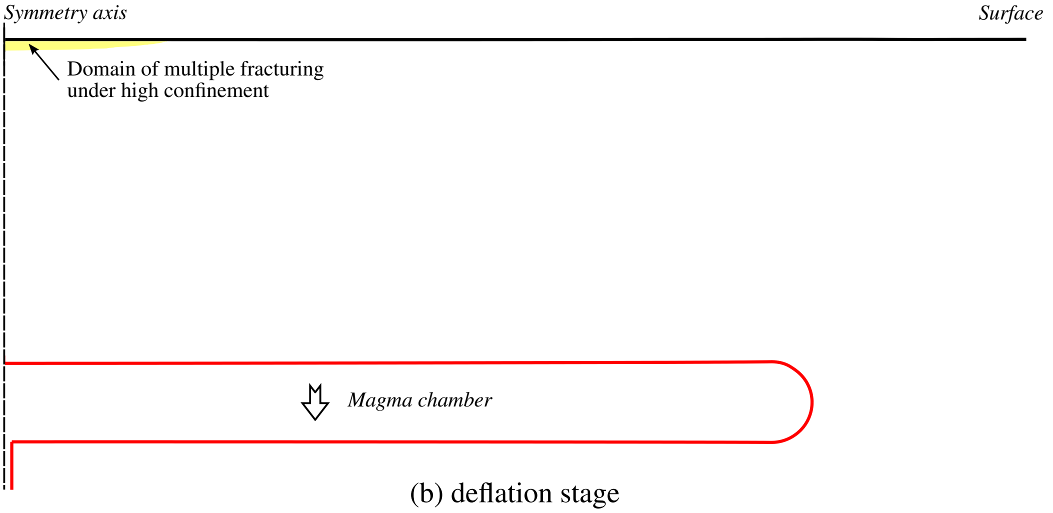

(b) deflation stage

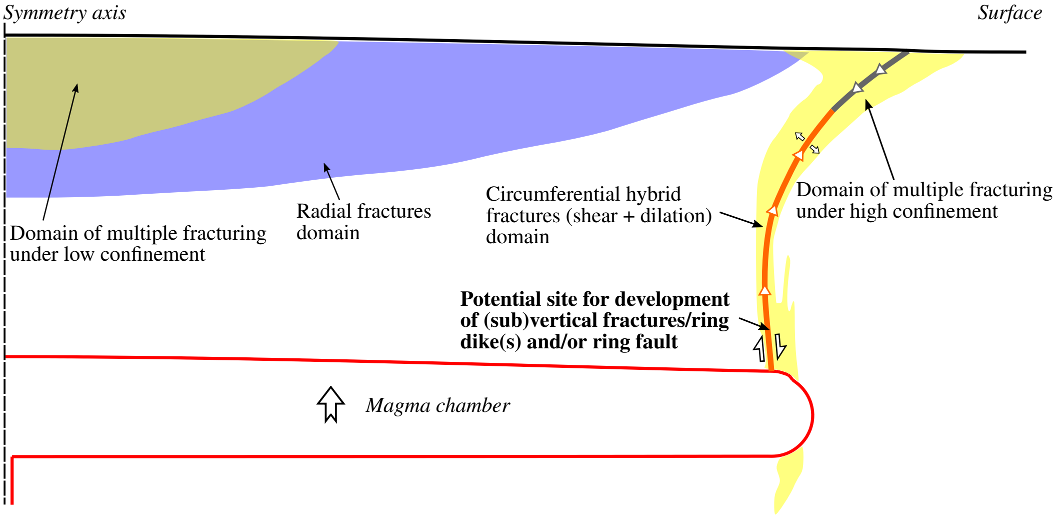

(c) maximum inflation stage, till the onset of a roof collapse due to overpressure

Figure 5.4: Schematic figures for a sill-like magma chamber with 50 km in diameter and 10 km beneath the surface at different loading stages (Case S-50/10).

wards from the edge of the magma chamber and to intersect with a downward propagating domain of multiple fracturing under high confinement indicating there a potential site for development of reverse ring fault. The deflation stage, see Figure 5.5(b), generates only a domain of circumferential hybrid (shear and dilation) fractures defining a potential site for development of an outward-dipping reverse ring fault, which propagates from the chamber margin towards the region of the maximum surface subsidence. The underpressure scenario would cause an outward-dipping piston subsidence and collapse.

The maximum inflation stage, shown in Figure 5.5(c), brings almost identical fracturing modes as the inflation stage, just the domain of radial fractures expands approximately two times. The overpressure scenario would lead to an inward-dipping piston resurgence and collapse.

Case S-10/5

The inflation stage of a mid-size chamber (diameter 10 km) at intermediate depth (5 km), illustrated in Figure 5.6(a), generates a band of inward-dipping, circumferential hybrid (shear and dilation) fractures propagating upwards from the edge of the magma chamber to the surface, indicating there a potential site for development of a reverse ring fault. Domains of radial fractures and multiple fracturing under low confinement expand above the center of the chamber downwards and sideways, with the largest intensity of fracturing near the symmetry axis. During the deflation stage, see Figure 5.6(b), the most intense radial fracturing concentrates along the chamber-roof contact together with a domain of multiple fracturing under low confinement, and the potential site for development of a reverse ring fault switches from inward- to outward-dipping. The underpressure scenario would lead to an outward-dipping piston subsidence and collapse.

The maximum inflation stage, shown in Figure 5.6(c), causes almost identical fracturing modes as the inflation stage, just the domains of radial fractures and multiple fracturing under low confinement expands nearly two times. The overpressure scenario would result in an inward-dipping piston resurgence and collapse.

Case S-10/7.5

During the inflation stage of a mid-size (diameter 10 km) deep (7.5 km) chamber, illustrated in Figure 5.7(a), a band of (sub)vertical, circumferential hybrid (shear and dilation) fractures propagates upwards from the edge of the magma chamber to the surface. This band indicates a potential site for development of a ring fault. A radial fractures domain expands above the center of the chamber downwards and sideways, with the largest intensity of fracturing and magnitude close to the symmetry axis. During the deflation stage, shown in Figure 5.7(b), only a domain of circumferential hybrid (shear and dilation) fractures defining a potential site for development of outward-dipping reverse ring fault propagates from the chamber margin to the surface. The underpressure scenario would cause an outward-dipping piston subsidence and collapse.

The maximum inflation stage, shown in Figure 5.7(c), brings almost identical fracturing modes as the inflation stage, just the domain of radial fractures expands sideways from the

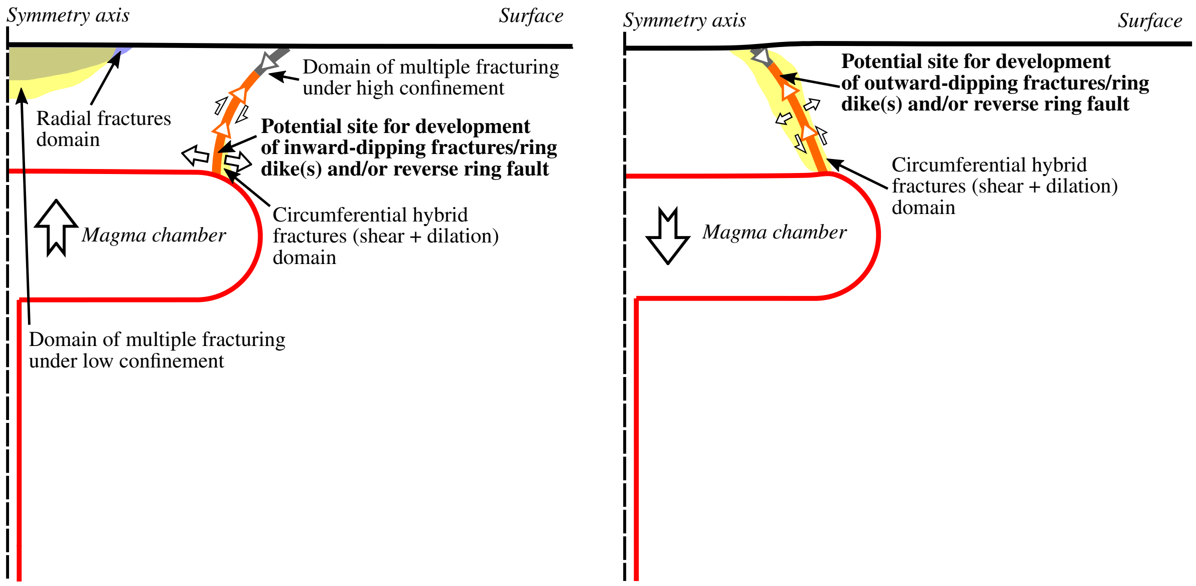

(a) inflation stage, until a potential site for development of a feeder dike occurred

(b) deflation stage, till the onset of a roof collapse due to underpressure

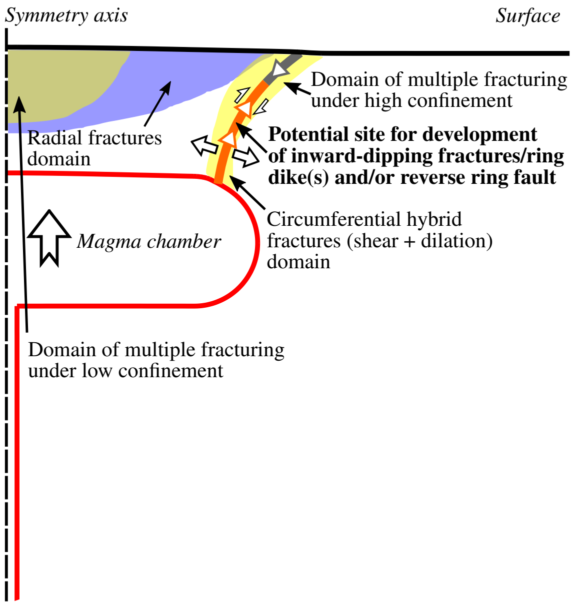

(c) maximum inflation stage, till the onset of a roof collapse due to overpressure

Figure 5.5: Schematic figures for a sill-like magma chamber with 10 km in diameter and 2.5 km beneath the surface at different loading stages (Case S-10/2.5).

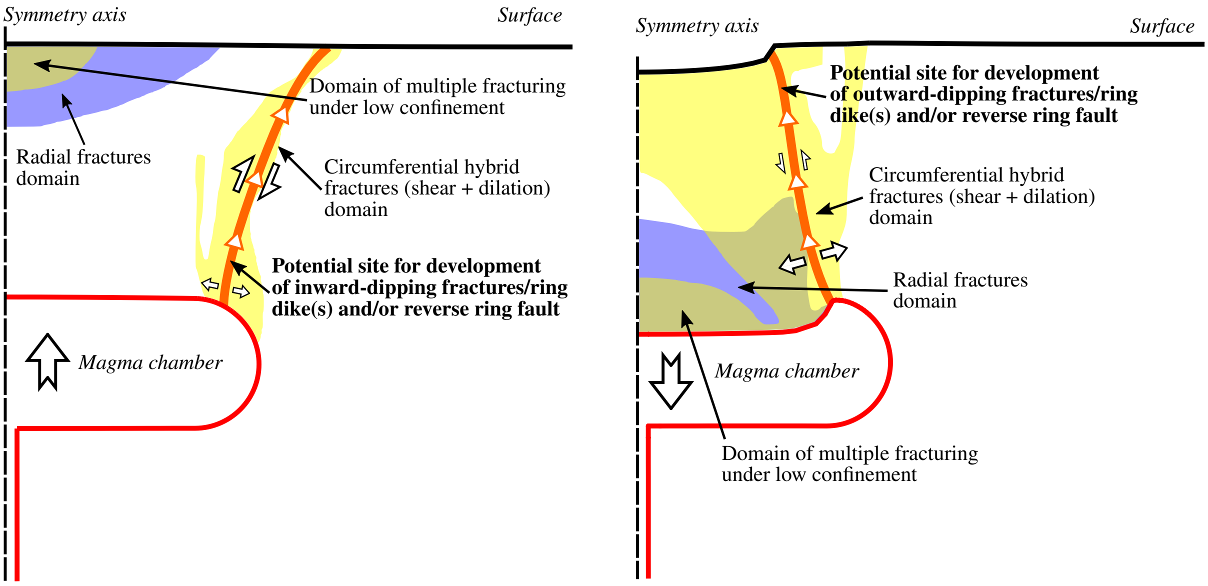

(a) inflation stage, until a potential site for development of a feeder dike occurred

(b) deflation stage, till the onset of a roof collapse due to underpressure

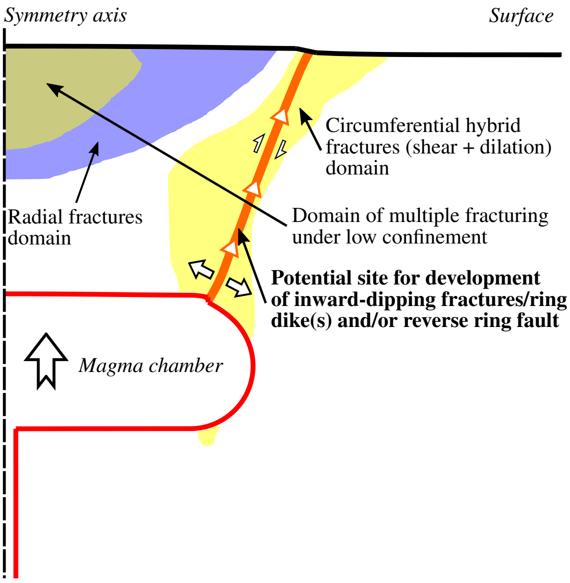

(c) maximum inflation stage, till the onset of a roof collapse due to overpressure

Figure 5.6: Schematic figures for a sill-like magma chamber with 10 km in diameter and 5 km beneath the surface at different loading stages (Case S-10/5).

symmetry axis beyond the potential vertical ring fault. The overpressure scenario would lead to a (sub)vertical piston resurgence and collapse.

Case S-10/10

Similarly to the previous case S-10/7.5, the inflation stage of a mid-size (diameter 10 km) deep-seated (10 km) chamber, illustrated in Figure 5.8(a), generates a band of (sub)vertical, circumferential hybrid (shear and dilation) fractures propagating upwards from the edge of the magma chamber to the surface. The band determines a potential site for development of a ring fault. A radial fractures domain expands above the center of the chamber downwards and sideways reaching the band of circumferential hybrid fractures, with the largest intensity of fracturing and magnitude close to the symmetry axis. During the deflation stage, shown in Figure 5.8(b), only a broad domain of outward-dipping, circumferential hybrid (shear and dilation) fractures defines an arch-like zone propagating from the chamber margin to 3/4 of the roof height. The underpressure scenario would cause a cauldron subsidence without collapse.

The maximum inflation stage, depicted in Figure 5.8(c), brings almost identical fracturing modes as the inflation stage, but the upper part of circumferential hybrid fractures domain enlarges farther from the symmetry axis defining a potential site for development of steeply inward-dipping reverse ring fault. The overpressure scenario would lead to an inward-dipping piston resurgence and collapse.

5.2 Cylindrical bell-jar magma chambers

Each case of the bell-jar magma chamber was discussed considering two stages only: (a) the inflation stage until a potential site for development of a feeder dike occurred and (b) the deflation stage till the onset of a roof collapse due to underpressure. The third stage, maximum inflation, was not modeled and the overpressure scenario not considered, recall Section 3.3.

Case B-50/5

During inflation, a large chamber (diameter 50 km) at intermediate depth (5 km), see Figure 5.9(a), produces a (sub)vertical damage zone of circumferential hybrid (shear and dilation) fractures propagating from the chamber margin, thus defining a potential site for development of a ring fault. However, after rising about 2/3 of roof height, the zone deviates sideways from the symmetry axis and passes into a near-surface zone of multiple fracturing under high confinement propagating from the surface. Also a flat domain of radial fractures expands above the center of the chamber. During the deflation stage, shown in Figure 5.9(b), the band of (sub)vertical fractures deviates towards the symmetry axis, where it connects with a domain of tensile fractures propagating from the surface. Beneath the surface, a domain of multiple fracturing under high confinement expands above the center of the chamber, while a flat subtle zone of radial fractures occurs on the chamber/roof contact above the chamber center. The underpressure scenario would lead to an outward-dipping piston subsidence and collapse.

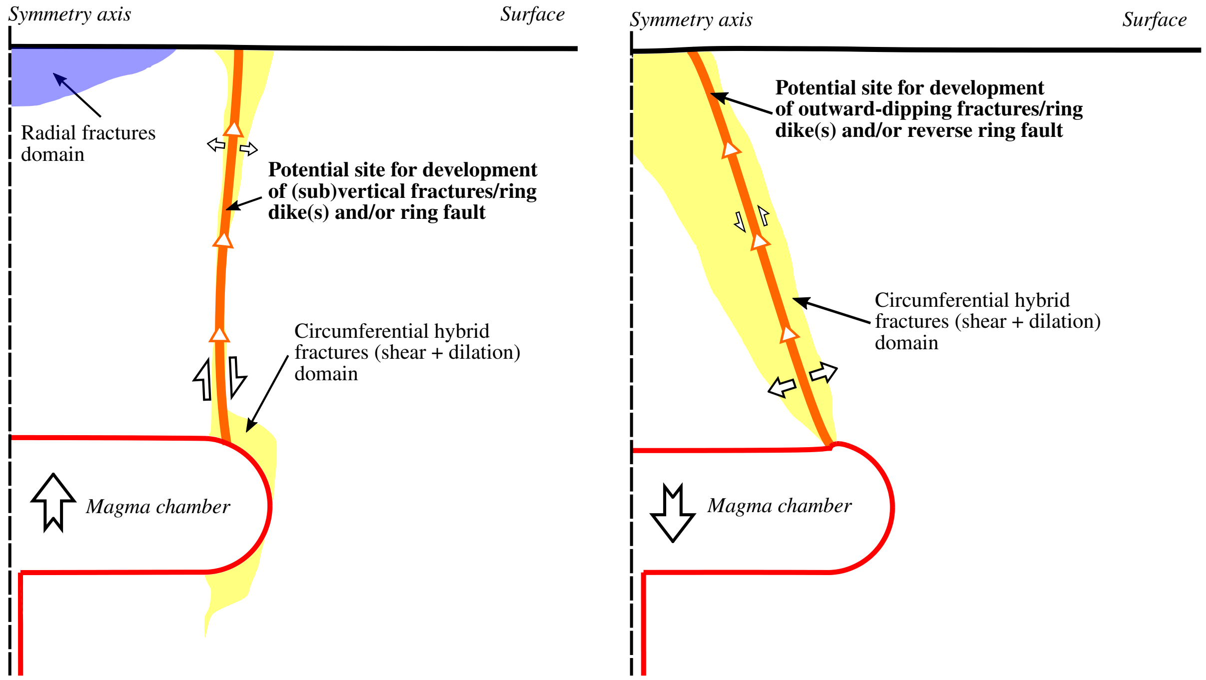

(a) inflation stage, until a potential site for development of a feeder dike occurred

(b) deflation stage, till the onset of a roof collapse due to underpressure

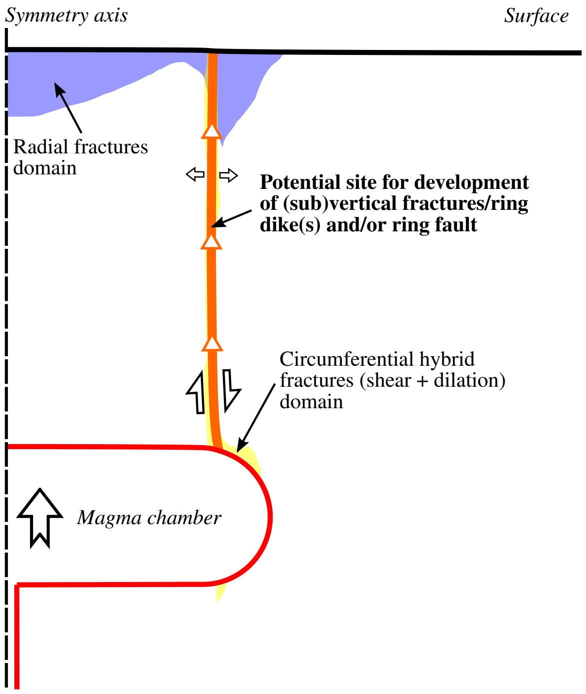

(c) maximum inflation stage, till the onset of a roof collapse due to overpressure

Figure 5.7: Schematic figures for a sill-like magma chamber with 10 km in diameter and 7.5 km beneath the surface at different loading stages (Case S-10/7.5).

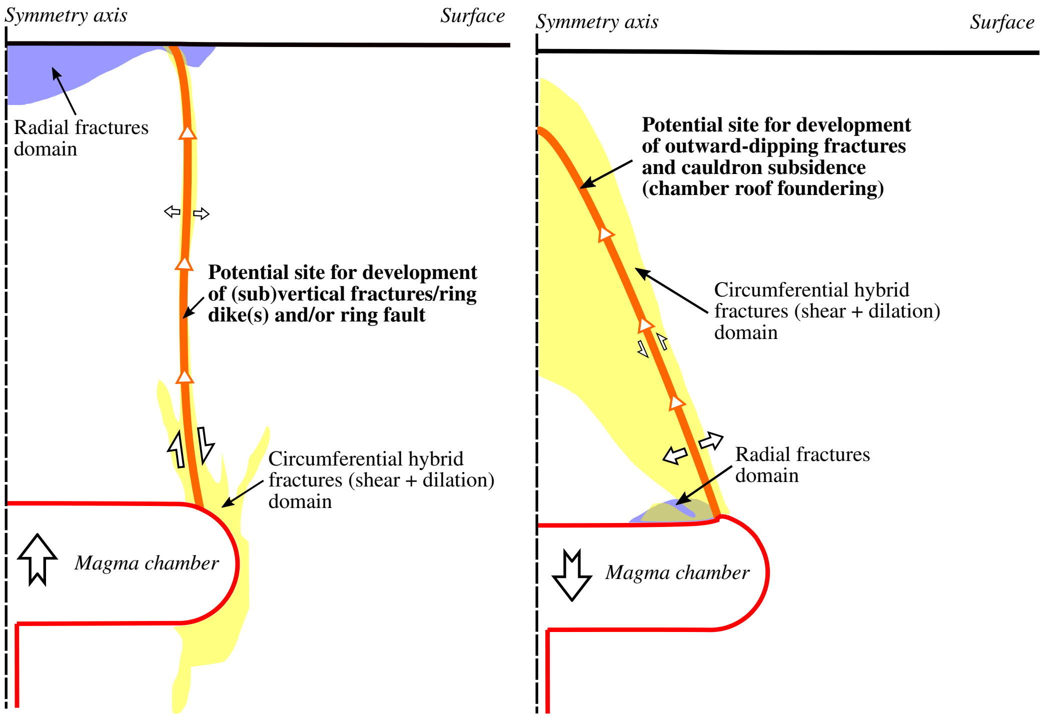

(a) inflation stage, until a potential site for development of a feeder dike occurred

(b) deflation stage, till the onset of a roof collapse due to underpressure

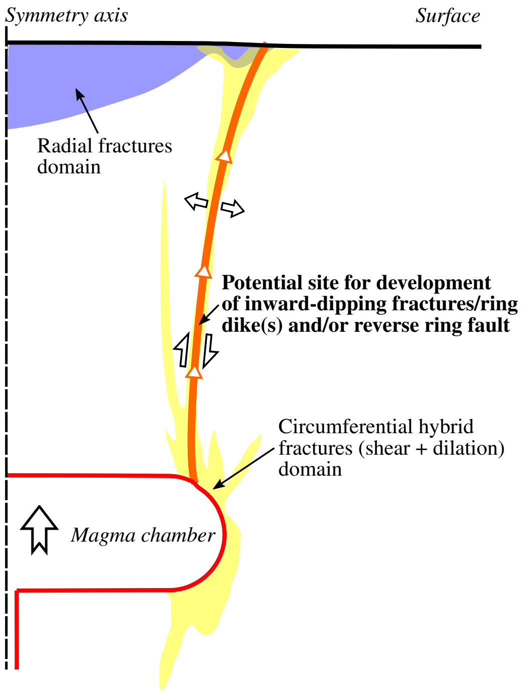

(c) maximum inflation stage, till the onset of a roof collapse due to overpressure

Figure 5.8: Schematic figures for a sill-like magma chamber with 10 km in diameter and 10 km beneath the surface at different loading stages (Case S-10/10).

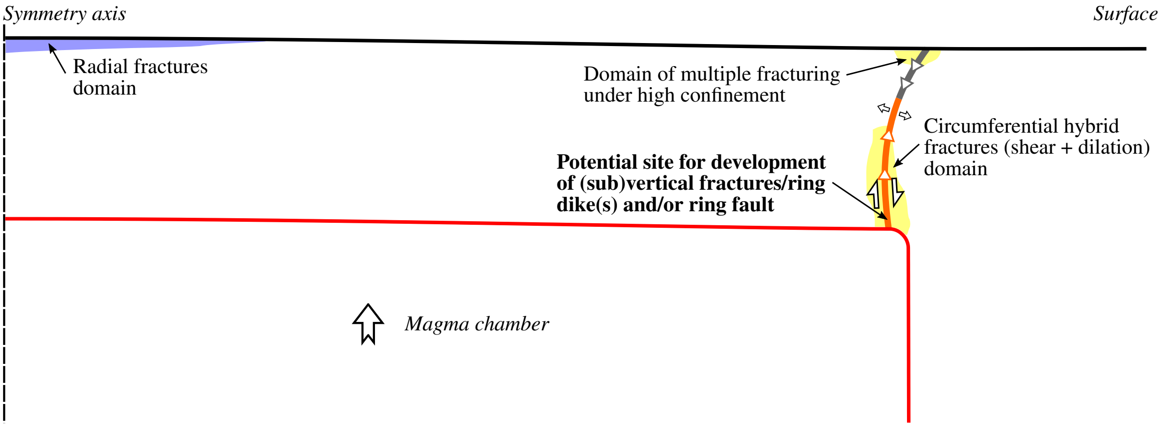

(a) inflation stage, until a potential site for development of a feeder dike occurred

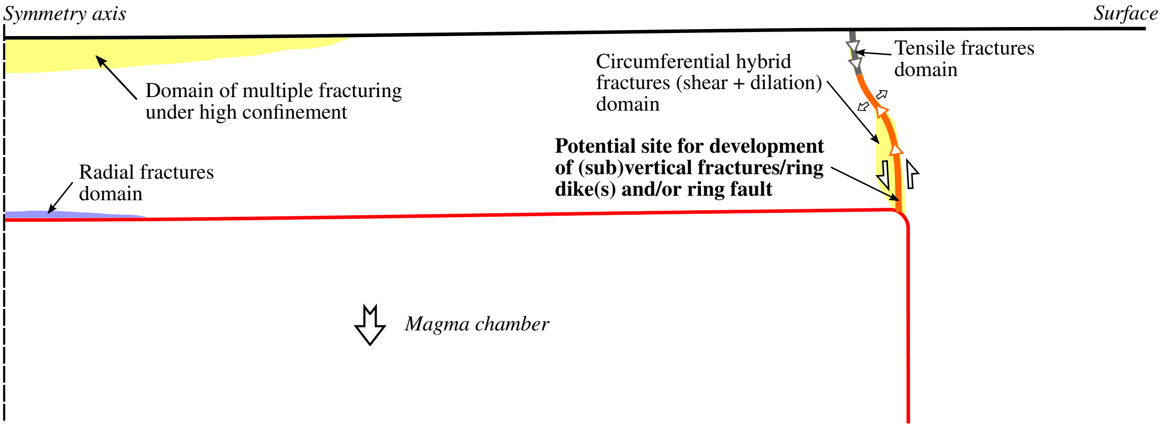

(b) deflation stage, till the onset of a roof collapse due to underpressure

Figure 5.9: Schematic figures for a bell-jar magma chamber with 50 km in diameter and 5 km beneath the surface at different loading stages (Case B-50/5).

Case B-50/10

Similarly to sill-like chambers, also a deep-seated (10 km) large chamber (diameter 50 km), illustrated in Figure 5.10(a), is examined, though enormous, and possibly unrealistic, magma overpressures would be necessary to develop feeder dikes without addition of tectonic forces. Nevertheless, the inflation stage generates a band of outward-dipping, circumferential hybrid (shear and dilation) fractures propagating upwards from the edge of the magma chamber. The band determines a potential site for development of a non-feeder dike as the band does not reach the surface, thus releasing the overpressure through it and consequent deflation is questionable. However, if the deflation stage, depicted in Figure 5.10(b), hypothetically comes, the band of (sub)vertical fractures deviates sideways from the symmetry axis, where it connects with a domain of tensile fractures propagating from the surface. Beneath the surface, a domain of multiple fracturing under high confinement expands above the center of the chamber, while a zone of radial fractures occurs on the chamber/roof contact above the chamber center. The underpressure scenario would lead to a (sub)vertical piston subsidence and collapse.

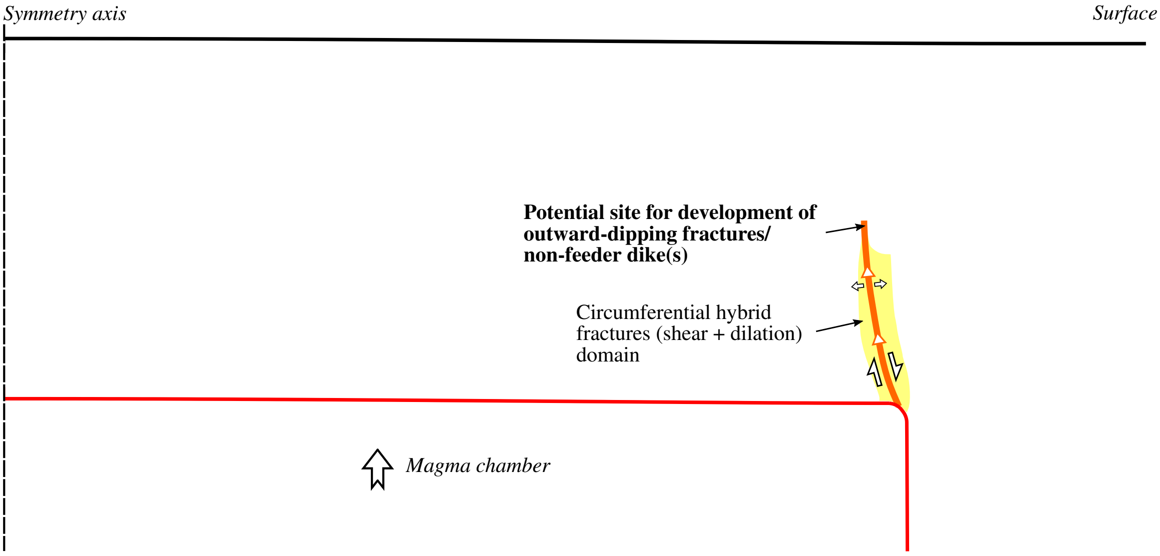

(a) inflation stage, until a potential site for development of a feeder dike occurred

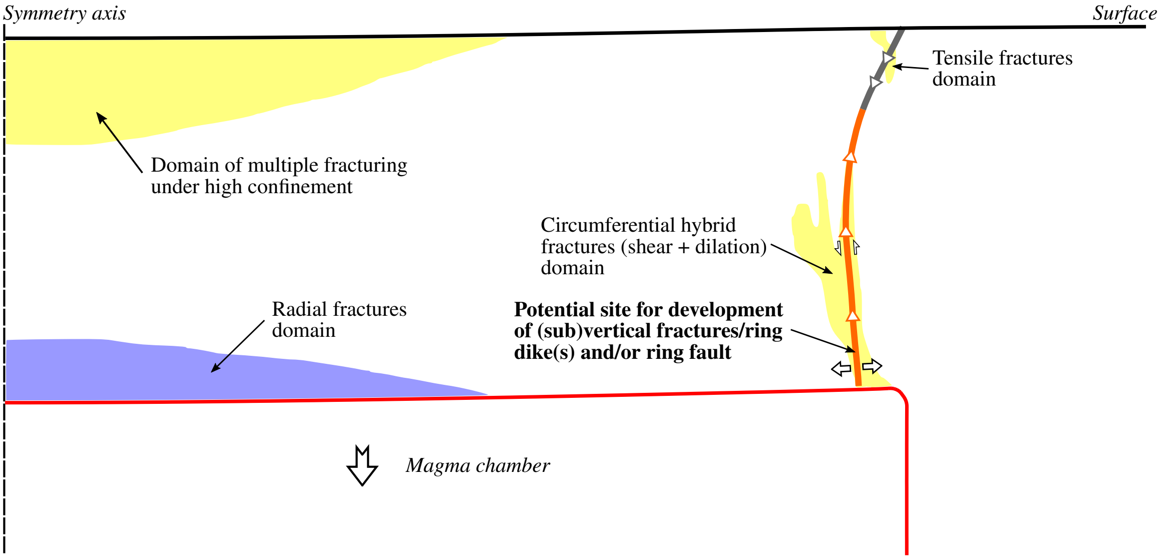

(b) deflation stage, till the onset of a roof collapse due to underpressure

Figure 5.10: Schematic figures for a bell-jar magma chamber with 50 km in diameter and 10 km beneath the surface at different loading stages (Case B-50/10).

Case B-10/5

The inflation stage of a mid-size chamber (diameter 10 km) at intermediate depth (5 km), illustrated in Figure 5.11(a), generates a band of inward-dipping, circumferential hybrid (shear and dilation) fractures propagating upwards from the edge of the magma chamber to the surface, indicating there a potential site for development of a reverse ring fault. One domain of radial fractures expands above the center of the chamber downwards and sideways, with the largest intensity of fracturing near the symmetry axis, and the other domain is along a chamber side and farther away from the chamber, with the magnitude of dilation increasing with depth and decreasing with distance from the chamber/host rock contact. During the deflation stage, see Figure 5.11(b), only a domain of circumferential hybrid (shear and dilation) fractures defining a potential site for development of outward-dipping reverse ring fault propagates from the chamber margin to the surface. The underpressure scenario would cause an outward-dipping piston subsidence and collapse.

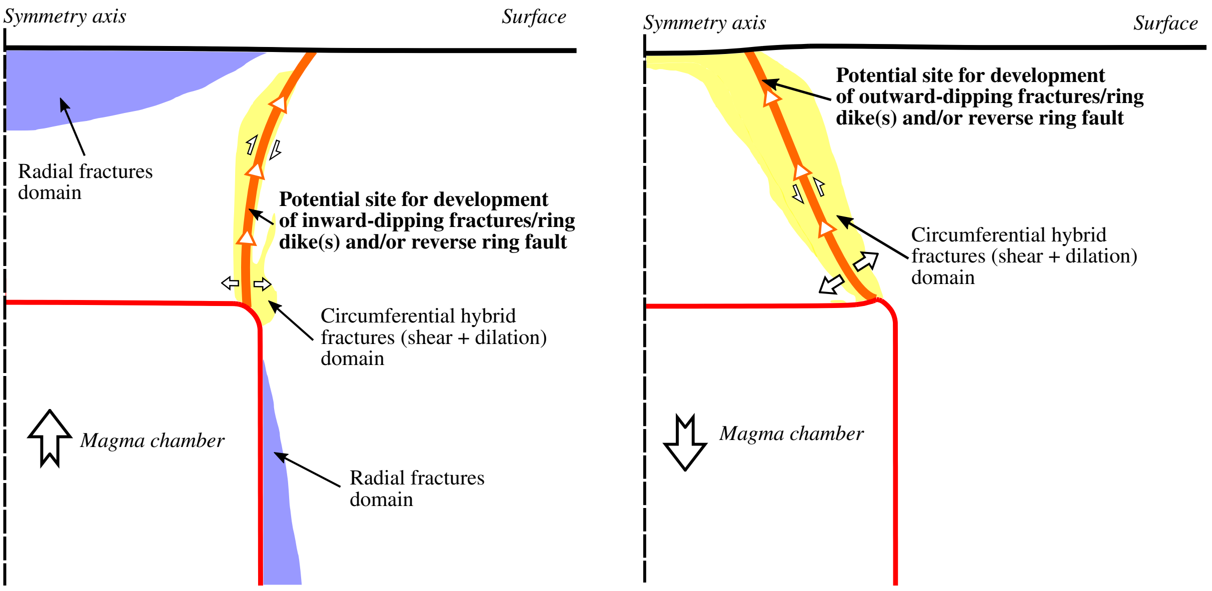

(a) inflation stage, until a potential site for development of a feeder dike occurred

(b) deflation stage, till the onset of a roof collapse due to underpressure

Figure 5.11: Schematic figures for a bell-jar magma chamber with 10 km in diameter and 5 km beneath the surface at different loading stages (Case B-10/5).

Case B-10/10

The inflation stage of a mid-size (diameter 10 km) deep-seated (10 km) chamber, illustrated in Figure 5.12(a), generates a band of (sub)vertical, circumferential hybrid (shear and dilation) fractures propagating upwards from the edge of the magma chamber. The band determines a potential site for development of a non-feeder dike as the band does not reach the surface, thus releasing the overpressure through it and consequent deflation is questionable. Also, one domain of radial fractures expands above the center of the chamber downwards and sideways, with the largest intensity of fracturing near the symmetry axis, and the other radial fractures domain is along a chamber side and farther away from the chamber, with the magnitude of dilation increasing with depth and decreasing with distance from the chamber/host rock contact. If the deflation stage, depicted in Figure 5.12(b), comes, only a broad domain of outward-dipping, circumferential hybrid (shear and dilation) fractures would define an arch-like zone propagating from the chamber margin to 1/2 of the roof height. The underpressure scenario would cause a cauldron subsidence without collapse.

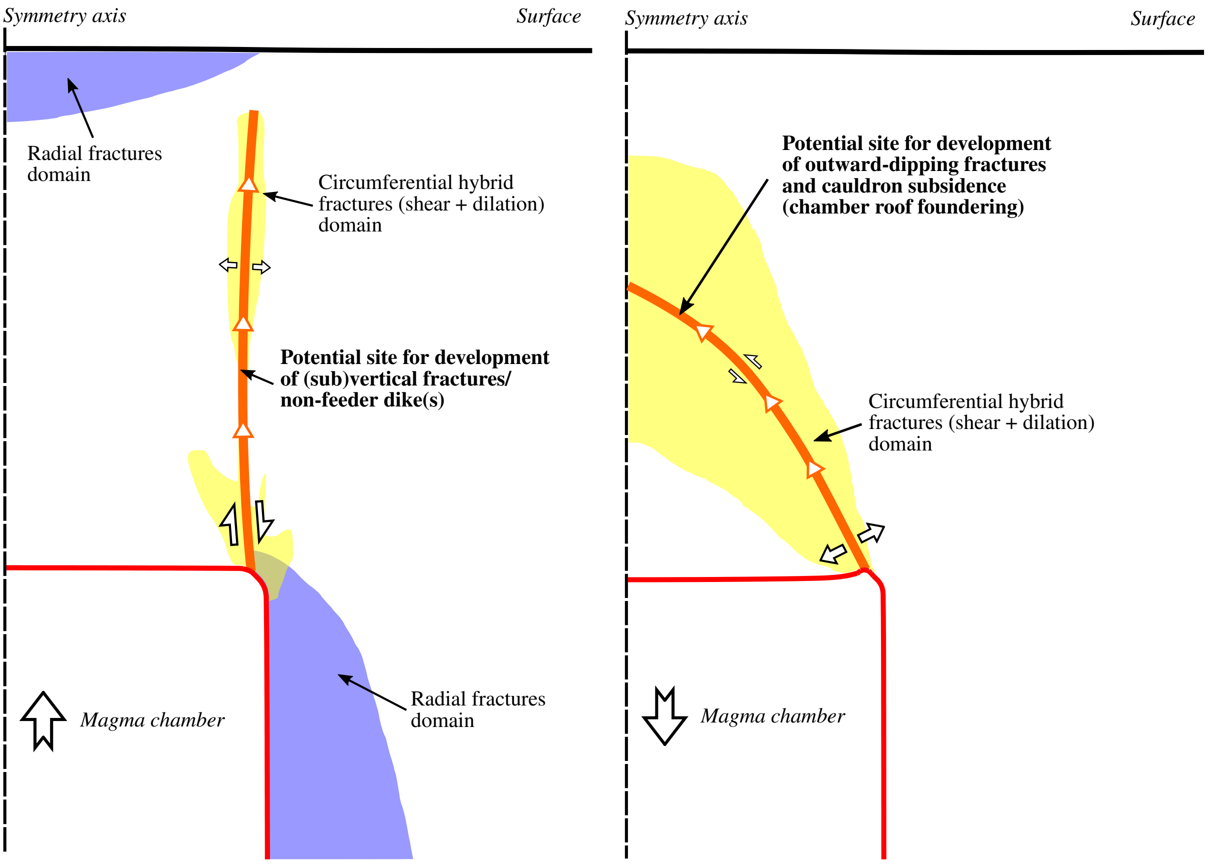

(a) inflation stage, until a potential site for development of a feeder dike occurred

(b) deflation stage, till the onset of a roof collapse due to underpressure

Figure 5.12: Schematic figures for a bell-jar magma chamber with 10 km in diameter and 10 km beneath the surface at different loading stages (Case B-10/10).

5.3 Summary

General implications of the modeling are summarized based on the above presented figures, which highlight how the most important geometric parameters control fracture development around magma chambers. The modeled cases allow to explore a range of conditions which lead to various competing roof fracturing and collapse mechanisms during the magma chamber inflation-deflation cycle and maximum inflation stage.

During the maximum inflation stage, leading to a roof resurgence and collapse due to overpressure, all sill-like chambers (with low roof-wall transition curvature) revealed a trend of reducing the near-surface, propagating sideways from the symmetry axis, fracturing as the roof aspect ratio, R, increased, particularly for $R > 0.5$. Consequently, with increasing R a region of non-fractured roof rock above the chamber was progressively enlarging. Throughgoing ring faults formed in all the cases of the modeled sill-like chambers. These were either inward-dipping reverse or (sub)vertical faults. For the cases with $R \leq 0.25$, the faults were significantly curved in an inward-dipping manner, however, the part propagating from the chamber upwards was (sub)vertical or steeply inward-dipping with mostly dominant shearing (rather than extending). Approximately in 1/2 of the roof height, the faults bent sideways from the symmetry axis and connected with near-surface downward propagating domains of multiple fracturing under high confinement. Cases with $R \geq 0.5$ evinced straight, inward-dipping or (sub)vertical, ring faults propagating solely upwards, and for $R \geq 0.75$, near-surface domains of fracturing under low confinement did not develop. Regardless of R, all the cases manifested a piston resurgence leading eventually to collapse.

During the inflation stage of the inflation-deflation cycle, leading to a collapse due to underpressure, all sill-like chambers performed almost identically as in the case of the maximum inflation stage, only the fracturing was less pronounced. For the bell-jar chambers (with high curvature of roof-wall transition), the roof height played bigger role than R. The fracturing above chambers at the intermediate depth reached surface in a (sub)vertical or steeply inward-dipping manner accompanied by near-surface, propagating sideways from the symmetry axis, radial fractures. However, (sub)vertical or deeply outward-dipping fractures above the deep-seated bell-jar chambers did not reach surface forming thus non-feeder dikes.

As the roof aspect ratio, R, increased, particularly for $R \geq 0.25$, the consequent deflation stage revealed, for sill-like chambers, a trend of diminishing the near-surface fracturing. All the throughgoing fractures developed outward-dipping reverse ring faults propagating almost exclusively from chamber margin upwards to the surface. Nevertheless, no fractures propagating from or to the magma chamber developed for two cases of large deep-seated chambers, thus representing cases which do not encourage caldera formation. With increasing R, the area on the surface bounded by the ring faults progressively decreased, and for $R = 1.0$, the fractures defined an arch-like zone propagating from the chamber margin to 3/4 of the roof height causing a cauldron subsidence without caldera collapse. However, if the ring faults were formed, they resulted in an outward-dipping piston subsidence and collapse, with the exception of very low-R and very shallow chamber, which demonstrated a downsag subsidence and collapse. With increasing R, the bell-jar chambers tended to rotate the ring faults from (sub)vertical or steeply inward-dipping (interconnected with near-surface downward propagating domains of tensile fractures) to outward-dipping reverse ones, all encouraging piston subsidence and collapse. Finally, for $R = 1.0$, the fractures again defined an arch-like zone propagating from the chamber margin to 1/2 of the roof height causing a cauldron subsidence without caldera collapse. However, it is important to bear in mind that the deep-seated bell-jar chambers did not develop feeder dikes, therefore they were not able to release magma pressure and initiate deflation stage and their further analyses were rather hypothetical.

Another process indicated by the presented modeling is magmatic stoping. While a common view is that stoping is predominantly driven by thermal stresses due to heating and differential expansion of the roof rock (e.g., [57, 133]), it was demonstrated here that it can also be facilitated by fracturing due to pressure fluctuations inside the magma chamber. It can be expected that piecemeal stoping will happen where a fractured domain develops at the roof-chamber contact, as depicted in Figures 5.1(b), 5.2(b), and 5.9(b). Furthermore, the analysis showed that stoping is particularly favored during the deflation stage regardless of magma chamber type. In some cases, magmatic stoping could be another means of the chamber roof collapse during magma pressure drop. This finding fits well the field observations which propose stoping as the main magma emplacement process in plutons with discordant, gently-dipping roofs abruptly rolling over into a steep wall (e.g., [174, 175]).

In summary, it has been shown that the host rock deformation around the simulated sill-like magma chambers undergoing maximum inflation always results in a piston resurgence and consequent caldera collapse (either along (sub)vertical or inward-dipping reverse ring faults) regardless of the roof aspect ratio, R. Deformation around inflating-deflating magma chambers (both types, sill-like and bell-jar) can be viewed as a competition of three limit processes controlled by the chamber-host rock system geometry: (1) the piston subsidence and consequent caldera collapse (either along (sub)vertical or outward-dipping reverse ring faults) is most likely to develop above chambers with $R \leq 0.75$, (2) chambers with very low R (≤ 0.125) favor roof bending and type of subsidence leading to collapse shifts from (sub)vertical or outward-dipping piston for large chambers, to downsag for mid-size chambers, and (3) cauldron subsidence for chambers with $R \approx 1.0$.

Table 5.1: Summary of the characteristic features formed during over- and underpressure scenarios. The cases are ordered with respect to roof aspect ratio, R. The table describes ring fault orientation (inward-dipping, outward-dipping, (sub)vertical), sense (normal, reverse), mode (shear, extension—as the mode is always mixed, the primary mode is stated first and the secondary mode is then in parentheses, if equal, stated with slash), propagation direction (upwards, downwards), subsidence/resurgence (for underpressure/overpressure scenarios) type, and whether collapse is likely to occur.

	Case	R	Ring fault					
			Orientation	Sense	Mode	Propagation	Subsidence/resurgence	Collapse
Underpressure	B-50/5	0.1	(sub)vertical	-	shear(extension)	upward/downward	piston	yes
	S-50/5	0.1	outward-dipping	reverse	shear(extension)	upward	piston	yes
	S-10/1.25	0.125	outward-dipping	reverse	extension(shear)	upward/downward	downsag	yes
	S-50/7.5	0.15	-	-	-	-	-	no
	B-50/10	0.2	(sub)vertical	-	extension(shear)	upward/downward	piston	yes
	S-50/10	0.2	-	-	-	-	-	no
	S-10/2.5	0.25	outward-dipping	reverse	shear/extension	upward/downward	piston	yes
	B-10/5	0.5	outward-dipping	reverse	extension(shear)	upward	piston	yes
	S-10/5	0.5	outward-dipping	reverse	extension(shear)	upward	piston	yes
	S-10/7.5	0.75	outward-dipping	reverse	extension(shear)	upward	piston	yes
	B-10/10	1.0	outward-dipping	reverse	extension(shear)	upward	cauldron	no
	S-10/10	1.0	outward-dipping	reverse	extension(shear)	upward	cauldron	no
Overpressure	S-50/5	0.1	(sub)vertical	-	shear(extension)	upward/downward	piston	yes
	S-10/1.25	0.125	inward-dipping	reverse	shear/extension	upward/downward	piston	yes
	S-50/7.5	0.15	(sub)vertical	-	shear(extension)	upward/downward	piston	yes
	S-50/10	0.2	(sub)vertical	-	shear(extension)	upward/downward	piston	yes
	S-10/2.5	0.25	inward-dipping	reverse	extension(shear)	upward/downward	piston	yes
	S-10/5	0.5	inward-dipping	reverse	extension(shear)	upward	piston	yes
	S-10/7.5	0.75	(sub)vertical	-	shear(extension)	upward	piston	yes
	S-10/10	1.0	inward-dipping	reverse	extension/shear	upward	piston	yes

Chapter 6

Conclusions and final remarks

The main goal of the presented work was to advance the knowledge and bring new views on fracturing processes pre- ceding caldera collapse through mathematical modeling, numerical simulations, and analysis. It was accomplished by combining plasticity solid model for a host rock and fluid model for magma within a finite element method framework. The objectives of the thesis were fulfilled as follows:

The loci and direction of a ring fault initiation and growth, i.e., whether it propagates from the surface downwards or from the magma chamber upwards.

Regardless chamber type (sill-like or bell-jar) and collapse scenario (over- or underpressure), the ring faults are always initiated at the chamber margin and propagate upwards. However, the cases with low roof aspect ratio, $R \leq 0.25$, also evince a formation of near-surface fracturing domains above the chamber margin, which propagate downwards and eventually interconnect with the upward propagating fractures.

The mode of a ring faults propagation, i.e., whether it propagates as shear, or extension fractures.

The ring faults manifest a mixed-mode propagation for all the modeled cases. Nevertheless, a general trend is that cases with $R \leq 0.25$ dominantly propagate as shear fractures, while the other as extension fractures.

The orientation (inward-dipping, vertical, outward-dipping) and sense of shear (normal, reverse) along ring faults.

The ring faults formed above undepressurized chambers have dominantly outward-dipping or (sub)vertical orientations. On the other hand, those formed above overpressurized chambers are either inward-dipping or (sub)vertical.

Concerning the sense of shearing, all the cases with dipping ring faults (as opposed to (sub)vertical faults, which can be neither normal nor reverse) are exclusively reverse. It should be noted here that most authors state that caldera collapse is reached via normal ring faults (e.g., [42, 43, 87, 99]). Even though Acocella et al. [45] confirm this, they also particularize that this is true for late stages of collapse, while the early stages are dominated by reverse faults. Since the calculations presented in this work stop in the early stages of the collapse, with its onset, the findings stated above are not in contradiction to the works of other researchers.

Influence of the roof aspect ratio, R, on formation of particular types of fractures to predetermine the subsequent collapse mode.

The sill-like magma chambers during the maximum inflation stage, leading to a roof resurgence and collapse due to overpressure, displayed the following response to increasing R:

- $R \leq 0.25$—the ring faults were significantly curved in an inward-dipping manner, however, the part propagating from the chamber upwards was (sub)vertical or steeply inward-dipping; approximately in 1/2 of the roof height, the faults bent sideways from the symmetry axis and connected with near-surface downward propagating domains of multiple fracturing under high confinement,
- $R \geq 0.5$—the near-surface, propagating sideways from the symmetry axis, extensive radial fracturing and fracturing under low confinement were less prominent, and the bent ring faults gradually turned to straight, inward-dipping or (sub)vertical, propagating solely upwards,
- $R \geq 0.75$—near-surface domains of fracturing under low confinement did not develop.

The sill-like magma chambers during the deflation stage, leading to a roof subsidence and collapse due to underpressure, displayed the following response to increasing R:

- $R \geq 0.25$—the near-surface, propagating sideways from the symmetry axis, extensive fracturing under high confinement were less prominent,
- R increasing—the area of the circular rim on the surface (formed by the outward-dipping reverse ring faults) progressively decreased,
- $R = 1.0$—the area of the circular rim on the surface (formed by the outward-dipping reverse ring faults) diminished and the fractures defined an arch-like zone forming a cauldron subsidence without caldera collapse.

The bell-jar magma chambers during the deflation stage, leading to a roof subsidence and collapse due to underpressure, displayed the following response to increasing R (however, the deep-seated bell-jar chambers did not develop feeder dikes, therefore their further analysis was rather hypothetical):

- R increasing—the ring faults showed a tendency to change orientation from (sub)vertical or steeply inward-dipping (interconnected with near-surface downward propagating domains of tensile fractures) to outward-dipping reverse ones, all encouraging piston subsidence and collapse,
- $R = 1.0$—fractures defined an arch-like zone forming a cauldron subsidence without caldera collapse.

Effect of a roof-wall transition (rounded blunt edges vs. abrupt bend with a significantly smaller radius) on the fracture propagation.

The effect of a roof-wall transition (the sill-like chambers had rounded blunt edges whereas the bell-jar bodies had their roofs taking an abrupt bend with a significantly smaller radius into the wall) on the fracture propagation was negligible. Moreover, the geometrically corresponding cases (e.g., Case B-10/5 and Case S-10/5) evinced almost identical fracturing patterns and subsidence types.

Future research should integrate the proposed modeling approach to caldera collapse with the thermal analysis and should involve temperature effects on the mechanical behavior of host rock during repeated magma injection into the chamber and its oscillating cooling and withdrawal by volcanic eruptions.

The thesis proves that the finite element method as an excellent tool for prediction of fracture orientations and localization above inflating and deflating magma chambers in the Earth's upper crust. While most of the previous studies of caldera collapse rely on the elastic stress analysis of host rock around an empty cavity, the presented thesis advances modeling of the process by incorporating non-linear failure phenomena and nearly incompressible fluid behavior of magma. This leads to a more realistic representation of the fracture processes prior to caldera formation. Moreover, to the best of author's knowledge, this is the first time to analyze fracturing processes preceding caldera collapse employing an identical non-linear modeling approach for both, over- and underpressure scenarios. It provides a unique view on this topic and facilitates direct comparison of the scenarios.

References

[1] P. W. Lipman. Subsidence of ash-flow calderas: relation to caldera size and magma-chamber geometry. *Bulletin of Volcanology*, 59(3):198–218, 1997. doi: 10.1007/s004450050186.

[2] A. Geyer and J. Martí. The new worldwide collapse caldera database (CCDB): A tool for studying and understanding caldera processes. *Journal of Volcanology and Geothermal Research*, 175(3):334–354, 2008. doi: 10.1016/j.jvolgeores.2008.03.017.

[3] H. Sigurdsson. *Encyclopedia of Volcanoes*. Academic Press, San Francisco, 2000. ISBN 978-0126431407. doi: 10.1063/1.1325206.

[4] R. J. Blong. *Volcanic hazard and risk management – Encyclopedia of Volcanoes*. Academic Press, San Francisco, 2000. ISBN 978-0126431407. doi: 10.1063/1.1325206.

[5] R. J. Blong. Building damage in Rabaul, Papua New Guinea, 1994. *Bulletin of Volcanology*, 65(1):43–54, 2002. doi: 10.1007/s00445-002-0238-x.

[6] C. Witham. Volcanic disasters and incidents: a new database. *Journal of Volcanology and Geothermal Research*, 148:191–233, 2005. doi: 10.1016/j.jvolgeores.2005.04.017.

[7] L. Guillou-Frottier, E. B. Burov, and J. P. Milési. Genetic links between ash-flow calderas and associated ore deposits as revealed by large scale thermo-mechanical modeling. *Journal of Volcanology and Geothermal Research*, 102:339–361, 2000. doi: 10.1016/s0377-0273(00)00246-8.

[8] C. L. Ping. *Volcanic soils – Encyclopedia of Volcanoes*. Academic Press, San Francisco, 2000. ISBN 978-0126431407. doi: 10.1063/1.1325206.

[9] G. P. L. Walker. Downsag calderas, ringfaults, caldera sizes, and incremental growth. *Journal of Geophysical Research*, 89:8407–8416, 1984. doi: 10.1029/jb089ib10p08407.

[10] P. W. Lipman. *Calderas – Encyclopedia of Volcanoes*. Academic Press, San Francisco, 2000. ISBN 978-0126431407. doi: 10.1063/1.1325206.

[11] H. Williams. *Volcanoes*. Scientific American, 1951.

[12] M. J. Branney. Downsag and extension at calderas: new perspectives on collapse geometries from ice-melt, mining, and volcanic subsidence. *Bulletin of Volcanology*, 57 (5):303–318, 1995. doi: 10.1007/s004450050096.

[13] J. Cole, D. Milner, and K. Spinks. Calderas and caldera structures: a review. *Earth-Science Reviews*, 69(1-2):1–26, 2005. doi: 10.1016/j.earscirev.2004.06.004.

[14] V. Acocella. Correction to "Caldera types: How end-members relate to evolutionary stages of collapse". *Geophysical Research Letters*, 33(20), 2006. doi: 10.1029/2006gl028390.

[15] V. Acocella. Understanding caldera structure and development: An overview of analogue models compared to natural calderas. *Earth-Science Reviews*, 85(3-4): 125–160, 2007. doi: 10.1016/j.earscirev.2007.08.004.

[16] H. C. Hardee. Incipient magma chamber formation as a result of repetitive intrusions. *Bulletin Volcanologique*, 45(1):41–49, 1982. doi: 10.1007/bf02600388.

[17] A. M. Jellinek and D. J. DePaolo. A model for the origin of large silicic magma chambers: precursors of caldera-forming eruptions. *Bulletin of Volcanology*, 65(5): 363–381, 2003. doi: 10.1007/s00445-003-0277-y.

[18] A.F. Glazner, J.M. Bartley, and D.S. Coleman. Are plutons assembled over millions of years by amalgamation from small magma chambers? *GSA Today*, 14:4–11, 2004. doi: 10.1130/1052-5173(2004)014¡0004:APAOMO¿2.0.CO;2.

[19] B.A. Walker, C.F. Miller, L. Lowery Claiborne, J.L. Wooden, and J.S. Miller. Geology and geochronology of the Spirit Mountain batholith, southern Nevada: Implications for timescales and physical processes of batholith construction. *Journal of Volcanology and Geothermal Research*, 167(1-4):239–262, 2007. doi: 10.1016/j.jvolgeores.2006.12.008.

[20] S. L. de Silva and W. D. Gosnold. Episodic construction of batholiths: Insights from the spatiotemporal development of an ignimbrite flare-up. *Journal of Volcanology and Geothermal Research*, 167(1-4):320–335, 2007. doi: 10.1016/j.jvolgeores.2007.07.015.

[21] J. Michel, L. Baumgartner, B. Putlitz, U. Schaltegger, and M. Ovtcharova. Incremental growth of the Patagonian Torres del Paine laccolith over 90 k.y. *Geology*, 36(6):459, 2008. doi: 10.1130/g24546a.1.

[22] C. Annen. From plutons to magma chambers: Thermal constraints on the accumulation of eruptible silicic magma in the upper crust. *Earth and Planetary Science Letters*, 284 (3-4):409–416, 2009. doi: 10.1016/j.epsl.2009.05.006.

[23] M. de Saint Blanquat, E. Horsman, G. Habert, S. Morgan, O. Vanderhaeghe, R. Law, and B. Tikoff. Multiscale magmatic cyclicity, duration of pluton construction, and the paradoxical relationship between tectonism and plutonism in continental arcs. *Tectonophysics*, 500(1-4):20–33, 2011. doi: 10.1016/j.tecto.2009.12.009.

[24] C. Michaut and C. Jaupart. Two models for the formation of magma reservoirs by small increments. *Tectonophysics*, 500(1-4):34–49, 2011. doi: 10.1016/j.tecto.2009.08.019.

[25] S. R. Paterson, D. Okaya, V. Memeti, R. Economos, and R. B. Miller. Magma addition and flux calculations of incrementally constructed magma chambers in continental margin arcs: Combined field, geochronologic, and thermal modeling studies. *Geosphere*, 7(6):1439–1468, 2011. doi: 10.1130/ges00696.1.

[26] P. W. Lipman and O. Bachmann. Ignimbrites to batholiths: Integrating perspectives from geological, geophysical, and geochronological data. *Geosphere*, 11(3):705–743, 2015. doi: 10.1130/ges01091.1.

[27] K. Aizawa, V. Acocella, and T. Yoshida. How the development of magma chambers affects collapse calderas: Insights from an overview. *Geological Society, London, Special Publications*, 269(1):65–81, 2006. doi: 10.1144/gsl.sp.2006.269.01.05.

[28] J. Marti, A. Geyer, and A. Folch. A genetic classification of collapse calderas based on field studies, and analogue and theoretical modelling. In *Studies in Volcanology: The Legacy of George Walker*, pages 249–266. The Geological Society of London on behalf of The International Association of Volcanology and Chemistry of the Earths Interior, 2009. doi: 10.1144/iavcel002.13.

[29] O. Galland. Experimental modelling of ground deformation associated with shallow magma intrusions. *Earth and Planetary Science Letters*, 317-318:145–156, 2012. doi: 10.1016/j.epsl.2011.10.017.

[30] C. Magee, F. Briggs, and C. A.-L. Jackson. Lithological controls on igneous intrusion-induced ground deformation. *Journal of the Geological Society*, 170(6): 853–856, 2013. doi: 10.1144/jgs2013-029.

[31] T. R. Walter and M. Motagh. Deflation and inflation of a large magma body beneath Uturuncu volcano, Bolivia? insights from InSAR data, surface lineaments and stress modelling. *Geophysical Journal International*, 198(1):462–473, 2014. doi: 10.1093/gji/ggu080.

[32] C. D. Henry, M. J. Kunk, W. R. Muehlberger, and W. C. McIntosh. Igneous evolution of a complex laccolith-caldera, the Solitario, Trans-Pecos Texas: Implications for calderas and subjacent plutons. *Geological Society of America Bulletin*, 109, 1997. doi: 10.1130/0016-7606(1997)109¡1036:IEOACL¿2.3.CO;2.

[33] V. Acocella and G. Mulugeta. Experiments simulating surface deformation induced by pluton emplacement. *Tectonophysics*, 352(3-4):275–293, 2002. doi: 10.1016/s0040-1951(02)00218-4.

[34] B. W. Davy and T. G. Caldwell. Gravity, magnetic and seismic surveys of the caldera complex, lake Taupo, North Island, New Zealand. *Journal of Volcanology and Geothermal Research*, 81:69–89, 1998. doi: 10.1016/s0377-0273(97)00074-7.

[35] D. M. Milner, C. P. Cole, and C. P. Wood. Assymetric, multiple-block, collapse at Rotorua caldera, Taupo Volcanic Zone, New Zealand. *Bulletin of Volcanology*, 64(2): 134–149, 2002. doi: 10.1007/s00445-001-0191-0.

[36] C. Troise, F. Pingue, and G. De Natale. Coulomb stress changes at calderas: modeling the seismicity of Campi Flegrei (southern Italy). *Journal of Geophysical Research*, 108: 2156–2202, 2003. doi: 10.1029/2002jb002006.

[37] P. W. Francis, R. S. J. Sparks, C. J. Hawkesworth, R. S. Thorpe, D. M. Pyle, S. R. Tait, M. S. Mantovani, and F. McDermott. Petrology and Geochemistry of Volcanic Rocks of the Cerro Galan Caldera, Northwest Argentina. *Geology Magazine*, 126:515–547, 1989. doi: 10.1017/s0016756800022834.

[38] C. J. Edgar, J. A. Wolff, H. J. Nichols, R. A. F. Cas, and J. Martí. A complex quaternary ignimbrite-forming phonolitic eruption: the Poris member of the Diego Hernández Formation (Tenerife, Canary Islands). *Journal of Volcanology and Geothermal Research*, 118:99–130, 2002. doi: 10.1016/s0377-0273(02)00252-4.

[39] V. R. Troll, C. H. Emeleus, and C. H. Donaldson. Caldera formation in the Rum Central Igneous complex, Scotland. *Bulletin of Volcanology*, 62(4–5):301–317, 2000. doi: 10.1007/s004450000099.

[40] P. T. Leat, R. MacDonald, and R. L. Smith. Geochemical evolution of the Menengai Caldera Volcano, Kenya. *Journal of Geophysical Research*, 89:8571–8592, 1984. doi: 10.1029/jb089ib10p08571.

[41] T. H. Druitt and R. S. J. Sparks. On the formation of calderas during ignimbrite eruptions. *Nature*, 310:679–681, 1984. doi: 10.1038/310679a0.

[42] H. Komuro, Y. Fujita, and K. Kodama. Numerical and experimental models on the formation mechanism of collapse basins during the Green Tuff orogenesis of Japan. *Bulletin of Volcanology*, 47:649–666, 1984. doi: 10.1007/bf01961233.

[43] A. Gudmundsson, J. Martí, and E. Turón. Stress fields generating ring-faults in volcanoes. *Geophysical Research Letters*, 24:1559–1562, 1997. doi: 10.1029/97gl01494.

[44] E. B. Burov and L. Guillou-Frottier. Thermomechanical behavior of large ash-flow calderas. *Journal of Geophysical Research*, 104(B10):23081–23109, 1999. doi: 10.1029/1999jb900227.

[45] V. Acocella, F. Cifelli, and R. Funiciello. Analogue models of collapse calderas and resurgent domes. *Journal of Volcanology and Geothermal Research*, 104(1-4):81–96, 2000. doi: 10.1016/s0377-0273(00)00201-8.

[46] T. R. Walter and V. R. Troll. Formation of caldera periphery faults: an experimental study. *Bulletin of Volcanology*, 63(2-3):191–203, 2001. doi: 10.1007/s004450100135.

[47] A. Folch and J. Martí. Geometrical and mechanical constraints on the formation of ring-fault calderas. *Earth and Planetary Science Letters*, 221:215–225, 2004. doi: 10.1016/s0012-821x(04)00101-3.

[48] J. P. Gray and J. J. Monaghan. Numerical modeling of stress fields and fracture around magma chambers. *Journal of Volcanology and Geothermal Research*, 135:259–283, 2004. doi: 10.1016/j.jvolgeores.2004.03.005.

[49] B. Kennedy, J. Stix, J. W. Vallance, Y. Lavallée, and M.-A. Longpré. Controls on caldera structure: Results from analogue sandbox modeling. *Geological Society of America Bulletin*, 116(5):515, 2004. doi: 10.1130/b25228.1.

[50] S. J. Saunders. The possible contribution of circumferential fault intrusion to caldera resurgence. *Bulletin of Volcanology*, 67(1):57–71, 2004. doi: 10.1007/s00445-004-0360-z.

[51] J. Martí, A. Geyer, A. Folch, and J. Gottsmann. Chapter 6 A review on collapse caldera modelling. In *Caldera Volcanism: Analysis, Modelling and Response*, pages 233–283. Elsevier, 2008. doi: 10.1016/s1871-644x(07)00006-x.

[52] S. Hardy. Structural evolution of calderas: Insights from two-dimensional discrete element simulations. *Geology*, 36(12):927, 2008. doi: 10.1130/g25133a.1.

[53] H. S. Kinvig, A. Geyer, and J. Gottsmann. On the effect of crustal layering on ring-fault initiation and the formation of collapse calderas. *Journal of Volcanology and Geothermal Research*, 186(3-4):293–304, 2009. doi: 10.1016/j.jvolgeores.2009.07.007.

[54] A. G. Simakin and A. Ghassemi. The role of magma chamber-fault interaction in caldera forming eruptions. *Bulletin of Volcanology*, 72(1):85–101, 2009. doi: 10.1007/s00445-009-0306-6.

[55] P. M. Gregg, S. L. de Silva, E. B. Grosfils, and J. P. Parmigiani. Catastrophic caldera-forming eruptions: Thermomechanics and implications for eruption triggering and maximum caldera dimensions on Earth. *Journal of Volcanology and Geothermal Research*, 241-242:1–12, 2012. doi: 10.1016/j.jvolgeores.2012.06.009.

[56] E. P. Holohan, M. P. J. Schpfer, and J. J. Walsh. Stress evolution during caldera collapse. *Earth and Planetary Science Letters*, 421:139–151, 2015. doi: 10.1016/j.epsl.2015.03.003.

[57] K. P. Furlong and J. D. Myers. Thermal-mechanical modeling of the role of thermal stresses and stoping in magma contamination. *Journal of Volcanology and Geothermal Research*, 24(1-2):179–191, 1985. doi: 10.1016/0377-0273(85)90032-0.

[58] D. B. Clarke, A. S. Henry, and M. A. White. Exploding xenoliths and the absence of ‘elephants graveyards’ in granite batholiths. *Journal of Structural Geology*, 20(9-10): 1325–1343, 1998. doi: 10.1016/s0191-8141(98)00082-0.

[59] D. P. Hawkins and R. A. Wiebe. Discrete stoping events in granite plutons: A signature of eruptions from silicic magma chambers? *Geology*, 32(12):1021, 2004. doi: 10.1130/g21083.1.

[60] G. S. Pignotta and S. R. Paterson. Voluminous stoping in the Mitchell Peak granodiorite, Sierra Nevada batholith, California, USA. *The Canadian Mineralogist*, 45 (1):87–106, 2007. doi: 10.2113/gscanmin.45.1.87.

[61] A. K. Petraske, D. S. Hodge, and R. Shaw. Mechanics of emplacement of basic intrusions. *Tectonophysics*, 46(1-2):41–63, 1978. doi: 10.1016/0040-1951(78)90104-x.

[62] C. E. Corry. Laccoliths, mechanics of emplacement and growth. In *Geological Society of America Special Papers*, pages 1–114. Geological Society of America, 1988. doi: 10.1130/spe220-p1.

[63] A.D. Kerr and D. D. Pollard. Toward more realistic formulations for the analysis of laccoliths. *Journal of Structural Geology*, 20(12):1783–1793, 1998. doi: 10.1016/s0191-8141(98)00071-6.

[64] O. Galland and J. Scheibert. Analytical model of surface uplift above axisymmetric flat-lying magma intrusions: Implications for sill emplacement and geodesy. *Journal of Volcanology and Geothermal Research*, 253:114–130, 2013. doi: 10.1016/j.jvolgeores.2012.12.006.

[65] G. A. MacDonald. Volcanoes. A discussion of volcanoes, volcanic products, and volcanic phenomena. *Geological Magazine*, 110(01):87, 1973. doi: 10.1017/s0016756800047476.

[66] A. Gudmundsson. Effect of tensile stress concentration around magma chambers on intrusion and extrusion frequencies. *Journal of Volcanology and Geothermal Research*, 35(3):179–194, 1988. doi: 10.1016/0377-0273(88)90015-7.

[67] A. Gudmundsson. Formation and development of normal-fault calderas and initiation of large explosive eruptions. *Bulletin of Volcanology*, 60:160–171, 1998. doi: 10.1007/s004450050224.

[68] J. Martí, A. Folch, A. Neri, and G. Macedonio. Pressure evolution during caldera-forming eruptions. *Earth and Planetary Science Letters*, 175:275–287, 2000. doi: 10.1016/s0012-821x(99)00296-4.

[69] A. Gudmundsson. Conceptual and numerical models of ring-fault formation. *Journal of Volcanology and Geothermal Research*, 164(3):142–160, 2007. doi: 10.1016/j.jvolgeores.2007.04.018.

[70] A. Gudmundsson. Chapter 8 magma: Chamber geometry, fluid transport, local stresses and rock behaviour during collapse caldera formation. In *Caldera Volcanism: Analysis, Modelling and Response*, pages 313–349. Elsevier, 2008. doi: 10.1016/s1871-644x(07)00008-3.

[71] S. L. de Silva and P. M. Gregg. Thermomechanical feedbacks in magmatic systems: Implications for growth, longevity, and evolution of large caldera-forming magma reservoirs and their supereruptions. *Journal of Volcanology and Geothermal Research*, 282:77–91, 2014. doi: 10.1016/j.jvolgeores.2014.06.001.

[72] R. Scandone. Chaotic collapse of calderas. *Journal of Volcanology and Geothermal Research*, 42(3):285–302, 1990. doi: 10.1016/0377-0273(90)90005-z.

[73] J. Martí. Caldera-like structures related to Permo-Carboniferous volcanism of the Catalan Pyrenees (NE Spain). *Journal of Volcanology and Geothermal Research*, 45 (3-4):173–186, 1991. doi: 10.1016/0377-0273(91)90057-7.

[74] O. Roche, T. H. Druitt, and O. Merle. Experimental study of caldera formation. *Journal of Geophysical Research: Solid Earth*, 105(B1):395–416, 2000. doi: 10.1029/1999jb900298.

[75] A. Geyer, A. Folch, and J. Martí. Relationship between caldera collapse and magma chamber withdrawal: An experimental approach. *Journal of Volcanology and Geothermal Research*, 157(4):375–386, 2006. doi: 10.1016/j.jvolgeores.2006.05.001.

[76] E. P. Holohan, M. P. J. Schpfer, and J. J. Walsh. Mechanical and geometric controls on the structural evolution of pit crater and caldera subsidence. *Journal of Geophysical Research*, 116(B7), 2011. doi: 10.1029/2010jb008032.

[77] A. Gudmundsson and K. Nilsen. Ring-faults in composite volcanoes: structures, models and stress fields associated with their formation. *Geological Society, London, Special Publications*, 269(1):83–108, 2006. doi: 10.1144/gsl.sp.2006.269.01.06.

[78] V. Pinel and C. Jaupart. Caldera formation by magma withdrawal from a reservoir beneath a volcanic edifice. *Earth and Planetary Science Letters*, 230(3-4):273–287, 2005. doi: 10.1016/j.epsl.2004.11.016.

[79] R. V. Fisher and H.-U. Schmincke. Stratigraphic problems of pyroclastic rocks. In *Pyroclastic Rocks*, pages 346–382. Springer Berlin Heidelberg, 1984. doi: 10.1007/978-3-642-74864-6-13.

[80] D. L. Turcotte, H. Ockendon, J. R. Ockendon, and S. J. Cowley. A mathematical model of vulcanian eruptions. *Geophysical Journal International*, 103(1):211–217, 1990. doi: 10.1111/j.1365-246x.1990.tb01763.x.

[81] P. Francis, C. Oppenheimer, and D. Stevenson. Endogenous growth of persistently active volcanoes. *Nature*, 366(6455):554–557, 1993. doi: 10.1038/366554a0.

[82] K. V. Cashman and G. Giordano. Calderas and magma reservoirs. *Journal of Volcanology and Geothermal Research*, 288:28–45, 2014. doi: 10.1016/j.jvolgeores.2014.09.007.

[83] D. C. Munro and S. K. Rowland. Caldera morphology in the western Galápagos and implications for volcano eruptive behavior and mechanisms of caldera formation. *Journal of Volcanology and Geothermal Research*, 72(1-2):85–100, 1996. doi: 10.1016/0377-0273(95)00076-3.

[84] G. A. Mahood. Pyroclastic rocks and calderas associated with strongly peralkaline magmatism. *Journal of Geophysical Research*, 89(B10):8540, 1984. doi: 10.1029/jb089ib10p08540.

[85] R. Cioni, R. Santacroce, and A. Sbrana. Pyroclastic deposits as a guide for reconstructing the multi-stage evolution of the Somma-Vesuvius Caldera. *Bulletin of Volcanology*, 61(4):207–222, 1999. doi: 10.1007/s004450050272.

[86] E. P. Holohan, B. van Wyk de Vries, and V. R. Troll. Analogue models of caldera collapse in strike-slip tectonic regimes. *Bulletin of Volcanology*, 70(7):773–796, 2007. doi: 10.1007/s00445-007-0166-x.

[87] E. P. Holohan, T. R. Walter, M. P. J. Schpfer, J. J. Walsh, B. van Wyk de Vries, and V. R. Troll. Origins of oblique-slip faulting during caldera subsidence. *Journal of Geophysical Research: Solid Earth*, 118(4):1778–1794, 2013. doi: 10.1002/jgrb.50057.

[88] S. Jónsson. Stress interaction between magma accumulation and trapdoor faulting on Sierra Negra volcano, Galápagos. *Tectonophysics*, 471(1-2):36–44, 2009. doi: 10.1016/j.tecto.2008.08.005.

[89] J. Mori and C. McKee. Outward-dipping ring-fault structure at Rabaul caldera as shown by earthquake locations. *Science*, 235(4785):193–195, 1987. doi: 10.1126/science.235.4785.193.

[90] L. Michon and F. Saint-Ange. Morphology of Piton de la Fournaise basaltic shield volcano (La Réunion island): Characterization and implication in the volcano evolution. *Journal of Geophysical Research*, 113(B3), 2008. doi: 10.1029/2005jb004118.

[91] N. Geshi. Asymmetric growth of collapsed caldera by oblique subsidence during the 2000 eruption of Miyakejima, Japan. *Earth and Planetary Science Letters*, 280(1-4): 149–158, 2009. doi: 10.1016/j.epsl.2009.01.027.

[92] I. A. N. Moore and P. Kokelaar. Tectonic influences in piecemeal caldera collapse at Glencoe Volcano, Scotland. *Journal of the Geological Society*, 154(5):765–768, 1997. doi: 10.1144/gsjgs.154.5.0765.

[93] M. J. Branney and P. Kokelaar. Volcanotectonic faulting,soft-state deformation, and rheomorphism of tuffs during development of a piecemeal caldera, English Lake District. *Bulletin of the Geological Society of America*, 106:507–530, 1994. doi: 10.1130/0016-7606(1994)106¡0507:VFSSDA¿2.3.CO;2.

[94] P. Kokelaar, P. Raine, and M. J. Branney. Incursion of a large-volume, spatter-bearing pyroclastic density current into a caldera lake: Pavey Ark ignimbrite, Scafell caldera, England. *Bulletin of Volcanology*, 70(1):23–54, 2007. doi: 10.1007/s00445-007-0118-5.

[95] S. Burchardt and T. R. Walter. Propagation, linkage, and interaction of caldera ring-faults: comparison between analogue experiments and caldera collapse at Miyakejima, Japan, in 2000. *Bulletin of Volcanology*, 72(3):297–308, 2009. doi: 10.1007/s00445-009-0321-7.

[96] A. Geyer and J. Martí. A short review of our current understanding of the development of ring faults during collapse caldera formation. *Frontiers in Earth Science*, 2, 2014. doi: 10.3389/feart.2014.00022.

[97] J. Martí, G. J. Ablay, L. T. Redshaw, and R. S. J. Sparks. Experimental studies of collapse calderas. *Journal of the Geological Society*, 151(6):919–929, 1994. doi: 10.1144/gsjgs.151.6.0919.

[98] V. Acocella, F. Cifelli, and R. Funiciello. The control of overburden thickness on resurgent domes: insights from analogue models. *Journal of Volcanology and Geothermal Research*, 111(1-4):137–153, 2001. doi: 10.1016/s0377-0273(01)00224-4.

[99] O. Roche and T. H. Druitt. Onset of caldera collapse during ignimbrite eruption. *Earth and Planetary Science Letters*, 191:191–202, 2001. doi: 10.1016/s0012-821x(01)00428-9.

[100] Y. Lavallée, J. Stix, B. Kennedy, M. Richer, and M.-A. Longpré. Caldera subsidence in areas of variable topographic relief: results from analogue modeling. *Journal of Volcanology and Geothermal Research*, 129(1-3):219–236, 2004. doi: 10.1016/s0377-0273(03)00241-5.

[101] J. Ruch, V. Acocella, N. Geshi, A. Nobile, and F. Corbi. Kinematic analysis of vertical collapse on volcanoes using experimental models time series. *Journal of Geophysical Research: Solid Earth*, 117(B07301), 2012. doi: 10.1029/2012jb009229.

[102] S. Kusumoto and K. Takemura. Numerical simulation of caldera formation due to collapse of a magma chamber. *Geophysical Research Letters*, 30(24), 2003. doi: 10.1029/2003gl018380.

[103] S. Kusumoto and K. Takemura. Caldera geometry by the depth of the magma chamber. *Earth, Planets and Space*, 57:e17–e20, 2005. doi: 10.1186/bf03351879.

[104] A. Geyer and J. Martí. Stress fields controlling the formation of nested and overlapping calderas: Implications for the understanding of caldera unrest. *Journal of Volcanology and Geothermal Research*, 181(3-4):185–195, 2009. doi: 10.1016/j.jvolgeores.2009.01.018.

[105] N. Geshi, T. Shimano, T. Chiba, and S. Nakada. Caldera collapse during the 2000 eruption of Miyakejima Volcano, Japan. *Bulletin of Volcanology*, 64(1):55–68, 2001. doi: 10.1007/s00445-001-0184-z.

[106] S. Jónsson, H. Zebker, and F. Amelung. On trapdoor faulting at Sierra Negra volcano, Galápagos. *Journal of Volcanology and Geothermal Research*, 144(1-4):59–71, 2005. doi: 10.1016/j.jvolgeores.2004.11.029.

[107] L. Michon, F. Saint-Ange, P. Bachelery, N. Villeneuve, and T. Staudacher. Role of the structural inheritance of the oceanic lithosphere in the magmato-tectonic evolution of Piton de la Fournaise volcano (La Réunion Island). *Journal of Geophysical Research: Solid Earth*, 112(B04205), 2007. doi: 10.1029/2006jb004598.

[108] L. Michon, T. Staudacher, V. Ferrazzini, P. Bachèlery, and J. Martí. April 2007 collapse of Piton de la Fournaise: A new example of caldera formation. *Geophysical Research Letters*, 34(21), 2007. doi: 10.1029/2007gl031248.

[109] A. Geyer. *Dynamics and structural evolution of collapse calderas: A comparison between field evidence, analogue and mathematical models*. PhD thesis, Facultat de Geologia, Universitat de Barcelona, 2007.

[110] A. Folch and J. Martí. Time-dependent chamber and vent conditions during explosive caldera-forming eruptions. *Earth and Planetary Science Letters*, 280(1-4):246–253, 2009. doi: 10.1016/j.epsl.2009.01.035.

[111] A. Geyer and I. Bindeman. Glacial influence on caldera-forming eruptions. *Journal of Volcanology and Geothermal Research*, 202(1-2):127–142, 2011. doi: 10.1016/j.jvolgeores.2011.02.001.

[112] L. Karlstrom, M. L. Rudolph, and M. Manga. Caldera size modulated by the yield stress within a crystal-rich magma reservoir. *Nature Geoscience*, 5(6):402–405, 2012. doi: 10.1038/ngeo1453.

[113] A. Gudmundsson and I. F. Loetveit. Dyke emplacement in a layered and faulted rift zone. *Journal of Volcanology and Geothermal Research*, 144(1-4):311–327, 2005. doi: 10.1016/j.jvolgeores.2004.11.027.

[114] J. Chery, A. Bonneville, J. P. Villote, and D. Yuen. Numerical modelling of caldera dynamical behavior. *Geophysical Journal International*, 105:365–379, 1991. doi: 10.1111/j.1365-246x.1991.tb06719.x.

[115] E. Eberhardt. From cause to effect: using numerical modelling to understand rock slope instability mechanisms. In *NATO Science Series*, pages 85–101. Springer Netherlands, 2006. doi: 10.1007/978-1-4020-4037-5_4.

[116] S. Tait, C. Jaupart, and S. Vergniolle. Pressure, gas content and eruption periodicity of a shallow crystallizing magma chamber. *Earth and Planetary Science Letters*, 92: 107–123, 1989. doi: 10.1016/0012-821x(89)90025-3.

[117] J. Martí and A. Folch. Anticipating volcanic eruptions. In J. Martí and G. Ernst, editors, *Volcanoes and the Environment*, pages 90–120, Cambridge, 2005. Cambridge University Press. doi: 10.1017/cbo9780511614767.004.

[118] A. Folch and J. Martí. The generation of overpressure infelsic magma chamber by replenishment. *Earth and Planetary Science Letters*, 163:301–314, 1998. doi: 10.1016/s0012-821x(98)00196-4.

[119] G. I. Taylor. Instability of liquid surfaces when accelerated in a direction perpendicular to their planes. i. *1st Proceedings of the Royal Society of London A*, 201:192–196, 1950. doi: 10.1098/rspa.1950.0052.

[120] R. Hide and S. Chandrasekhar. The character of the equilibrium of an incompressible heavy viscous fluid of variable density: an approximate theory. *Mathematical Proceedings of the Cambridge Philosophical Society*, 51:178–197, 1955. doi: 10.1017/s030500410003005x.

[121] S. Chandrasekhar. The character of the equilibrium of an incompressible heavy viscous fluid of variable density. *Proceedings of Cambridge Philosophical Society*, 51: 162–178, 1955. doi: 10.1017/s0305004100030048.

[122] Z. F. Daneš. Mathematical formulation of salt-dome dynamics. *Geophysics*, 29: 414–424, 1964. doi: 10.1190/1.1439374.

[123] M. A. Biot and H. Odé. Theory of gravity instability with variable overburden and compaction. *Geophysics*, 30:213–227, 1965. doi: 10.1190/1.1439558.

[124] H. Odé. Gravitational instability of a multilayered system of high viscosity. *Koninklijke Nederlandse Akademie van Wetenschappen*, 24(1):96, 1965.

[125] H. Ramberg. Fluid dynamics of layered systems in the field of gravity, a theoretical basis for certain global structures and isostatic adjustment. *Physics of the Earth and Planetary Interiors*, 1:63–87, 1968. doi: 10.1016/0031-9201(68)90051-4.

[126] H. Ramberg. Instability of layered systems in the field of gravity, I. *Physics of the Earth and Planetary Interiors*, 1:427–447, 1968. doi: 10.1016/0031-9201(68)90014-9.

[127] F. F. Grout. Scale models of structures related to batholiths. *American Journal of Science*, 243:260–284, 1945.

[128] H. Ramberg. Model studies in relation to plutonic bodies. *Mechanism of igneous intrusion: Geological Journal Special Issue*, 2:261–286, 1970.

[129] H. Ramberg. *Gravity, Deformation and the Earth's Crust*. Academic Press, London, 1981.

[130] H. Berner, H. Ramberg, and O. Stephanson. Diapirism in theory and experiment. *Tectonophysics*, 15:197–218, 1972. doi: 10.1016/0040-1951(72)90085-6.

[131] W. D. Woidt. Finite element calculations applied to salt dome analysis. *Tectonophysics*, 50:369–386, 1978. doi: 10.1016/0040-1951(78)90143-9.

[132] J. A. Whitehead and D. S. Luther. Dynamics of laboratory diapir and plume models. *Journal of Geophysical Research*, 80:705–717, 1975. doi: 10.1029/jb080i005p00705.

[133] B. D. Marsh. On the mechanics of igneous diapirism, stoping and zone melting. *American Journal of Science*, 282:808–855, 1982. doi: 10.2475/ajs.282.6.808.

[134] N. M. Ribe. Diapirism in the Earth's mantle: Experiments on the motion of a hot sphere moving in a fluid with temperature-dependent viscosity. *Journal of Volcanology and Geothermal Research*, 16:221–245, 1983. doi: 10.1016/0377-0273(83)90031-8.

[135] S. F. Daly and A. Raefsky. On the penetration of a hot diapir through a strongly temperature-dependent medium. *Geophysical Journal of the Royal Astronomical Society*, 83:657–681, 1985. doi: 10.1111/j.1365-246x.1985.tb04331.x.

[136] A. Ansari and S. Morris. The effects of astrongly temperature-dependent viscosity on stokes drag law: experiments and theory. *Journal of Fluid Mechanics*, 159:459–476, 1985. doi: 10.1017/s0022112085003299.

[137] H. Schmeling, A. R. Cruden, and G. Marquart. Finite deformation in and around a fluid sphere moving through a viscous medium: implications for diapiric ascent. *Tectonophysics*, 149:17–34, 1988. doi: 10.1016/0040-1951(88)90116-3.

[138] A. R. Cruden. Deformation around a rising diapir modeled by creeping flow past a sphere. *Tectonics*, 7:1091–1101, 1988. doi: 10.1029/tc007i005p01091.

[139] J. P. Brun and J. Pons. Strain patterns of pluton emplacement in a crust undergoing non-coaxial deformation, Sierra Morena, S. Spain. *Journal of Structural Geology*, 3: 219–229, 1981. doi: 10.1016/0191-8141(81)90018-3.

[140] D. W. H. Hutton. Granite emplacement mechanisms and tectonic controls: inferences from deformation studies. *Transactions of the Royal Society of Edinburgh-Earth Sciences*, 79:245–255, 1988. doi: 10.1017/s0263593300014255.

[141] S. R. Paterson, R. H. Vernon, and O. T. Tobisch. A review of criteria for the identification of magmatic and tectonic foliations in granitoids. *Journal of Structural Geology*, 11:349–363, 1989. doi: 10.1016/0191-8141(89)90074-6.

[142] O. Stephansson. Polydiapirism of granitic rocks in the Svecofennian of central Sweden. *Precambrian Research*, 2:189–214, 1975. doi: 10.1016/0301-9268(75)90003-0.

[143] W. M. Schwerdtner. Salt stocks as natural analogues of Archaean gneiss diapirs. *Geologische Rundschau*, 71:370–379, 1982. doi: 10.1007/bf01825048.

[144] W. J. Collins. Polydiapirism of the Archaean Mount Edgar batholith, Pilbara block, Western Australia. *Precambrian Research*, 43:41–62, 1989. doi: 10.1016/0301-9268(89)90004-1.

[145] S. R. Paterson, R. H. Vernon, and T. K. Fowler. Chapter 13. aureole tectonics. In Derrill M. Kerrick, editor, *Contact Metamorphism*, pages 673–722. De Gruyter, 1991. doi: 10.1515/9781501509612-016.

[146] J. D. Clemens and C. K. Mawer. Granitic magma transport by fracture propagation. *Tectonophysics*, 204:339–360, 1992. doi: 10.1016/0040-1951(92)90316-x.

[147] D. D. Pollard. Elementary fracture mechanics applied to the structural interpretation of dykes. *Geological Association of Canada Special Paper*, 34:5–24, 1987.

[148] J. G. Goodchild. IV.—note on a granite junction in the Ross of Mull. *Geological Magazine*, 9:447–451, 1892. doi: 10.1017/s0016756800190764.

[149] A. C. Lawson. The eruptive sequence. *Science*, 3:635–637, 1896. doi: 10.1126/science.3.69.635-b.

[150] R. A. Daly. Mechanics of igneous intrusion. *American Journal of Science*, s4-16(92): 107–126, 1903. doi: 10.2475/ajs.s4-16.92.107.

[151] R. A. Daly. *Geology of Ascutney Mountain, Vermont*. Government Printing Office, Washington, 1903. doi: 10.5962/bhl.title.46303.

[152] R. A. Daly. *Igneous rocks and their origin*. McGraw-Hill Book Co., New York, 1914.

[153] R. A. Daly. *Igneous rocks and the depths of the Earth*. McGraw-Hill Book Co., New York, 1933.

[154] W. Pitcher. The nature, ascent and emplacement of granite magmas. *Journal of the Geological Society, London*, 136:627–662, 1979. doi: 10.1144/gsjgs.136.6.0627.

[155] ADINA R&D, Inc. Theory and Modeling Guide, Volume I: ADINA Solids & Structures. *ADINA R&D, Inc.*, pages 1–1322, 2017.

[156] P. Kabele, J. Žák, and M. Somr. Finite-element modeling of magma chamber-host rock interactions prior to caldera collapse. *Geophysical Journal International*, 209(3): 1851–1865, 2017. doi: 10.1093/gji/ggx121.

[157] S. R. Paterson, T. K. Fowler, and R. B. Miller. Pluton emplacement in arcs: a crustal-scale exchange process. In *Special Paper 315: The Third Hutton Symposium on the Origin of Granites and Related Rocks*, pages 115–123. Geological Society of America, 1996. doi: 10.1130/0-8137-2315-9.115.

[158] K. J. W. McCaffrey and N. Petford. Are granitic intrusions scale invariant? *Journal of the Geological Society*, 154(1):1–4, 1997. doi: 10.1144/gsjgs.154.1.0001.

[159] A. R. Cruden. On the emplacement of tabular granites. *Journal of the Geological Society*, 155(5):853–862, 1998. doi: 10.1144/gsjgs.155.5.0853.

[160] N. Petford, A. R. Cruden, K. J. W. McCaffrey, and J.-L. Vigneresse. Granite magma formation, transport and emplacement in the earths crust. *Nature*, 408:669–673, 2000. doi: 10.1038/35047000.

[161] P. W. Lipman. The roots of ash-flow calderas in western North America: Windows into the tops of granitic batholiths. *Journal of Geophysical Research*, 89:8801–8841, 1984.

[162] J. B. Lowenstern and S. Hurwitz. Monitoring a Supervolcano in Repose: Heat and Volatile Flux at the Yellowstone Caldera. *Elements*, 4(1):35–40, 2008. doi: 10.2113/gselements.4.1.35.

[163] C. A. Chesner. The Toba Caldera Complex. *Quaternary International*, 258:5–18, 2012. doi: 10.1016/j.quaint.2011.09.025.

[164] J. S. Myers. Cauldron Subsidence and Fluidization: Mechanisms of Intrusion of the Coastal Batholith of Peru into Its Own Volcanic Ejecta. *Geological Society of America Bulletin*, 86(9):1209–1220, 1975. doi: 10.1130/0016-7606(1975)86¡1209:CSAFMO¿2.0.CO;2.

[165] M. A. Bussell and C. D. V. Wilson. A gravity traverse across the Coastal Batholith, Peru. *Journal of the Geological Society*, 142(4):633–641, 1985. doi: 10.1144/gsjgs.142.4.0633.

[166] M. J. Roobol and D. L. White. Cauldron-subsidence structures and calderas above Arabian felsic plutons, a preliminary survey. *Journal of African Earth Sciences (1983)*, 4:123–134, 1986. doi: 10.1016/s0899-5362(86)80073-2.

[167] L.B Colmenares and M.D Zoback. A statistical evaluation of intact rock failure criteria constrained by polyaxial test data for five different rocks. *International Journal of Rock Mechanics and Mining Sciences*, 39(6):695–729, 2002. doi: 10.1016/s1365-1609(02)00048-5.

[168] S. J. Lutz, S. Hickman, N. Davatzes, E. Zemach, P. Drakos, and A. Robertson-Tait. Rock mechanical testing and petrologic analysis in support of well stimulation activities at the Desert peak geothermal field, Nevada. In *Proceedings of Thirty-Fifth Workshop on Geothermal Reservoir Engineering*, Stanford, California, 2010. Stanford University.

[169] Rocscience Inc. RS2 software online help - Theory. 2019. URL `https://www.rocscience.com/help/rs2/#t=FAQs%2FPhase2_FAQs__Theory.htm`.

[170] Y. Bottinga and D. F. Weill. Densities of liquid silicate systems calculated from partial molar volumes of oxide components. *American Journal of Science*, 269(2):169–182, 1970. doi: 10.2475/ajs.269.2.169.

[171] P. Segall and D. D. Pollard. Nucleation and growth of strike slip faults in granite. *Journal of Geophysical Research*, 88(B1):555, 1983. doi: 10.1029/jb088ib01p00555.

[172] D. C. P. Peacock. Propagation, interaction and linkage in normal fault systems. *Earth-Science Reviews*, 58(1-2):121–142, 2002. doi: 10.1016/s0012-8252(01)00085-x.

[173] J. G. Crider. The initiation of brittle faults in crystalline rock. *Journal of Structural Geology*, 77:159–174, 2015. doi: 10.1016/j.jsg.2015.05.001.

[174] A. S. Yoshinobu, T.K. Fowler, S. R. Paterson, E. Llambias, H. Tickyj, and A. M. Sato. A view from the roof: magmatic stoping in the shallow crust, Chita pluton, Argentina. *Journal of Structural Geology*, 25(7):1037–1048, 2003. doi: 10.1016/s0191-8141(02)00149-9.

[175] Scott R. Paterson and David W. Farris. Downward host rock transport and the formation of rim monoclines during the emplacement of Cordilleran batholiths. *Transactions of the Royal Society of Edinburgh: Earth Sciences*, 97(04):397–413, 2006. doi: 10.1017/s026359330000153x.

Appendix

The appendix provides a complete set of plots generated by the ADINA program for the FE calculations of all the evaluated cases and loading scenarios. To make the plots comparable, scales for the same stages of different cases have identical ranges. These plots were analyzed and interpreted as described in Section 4.2 in order to create the schematic figures, which were discussed in Chapter 5.

Case S-10/1.25

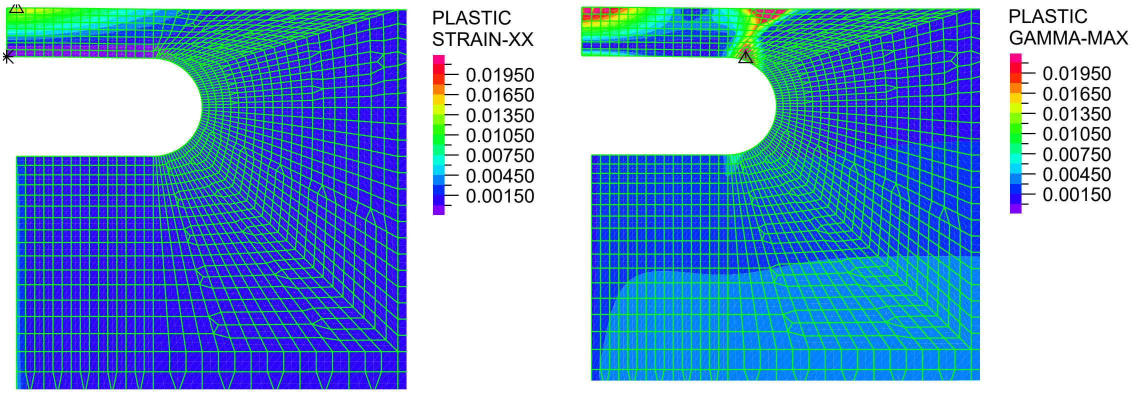

(a) iso-bands of the circumferential plastic normal strain

(b) iso-bands of the maximum plastic shear strain in the radial plane

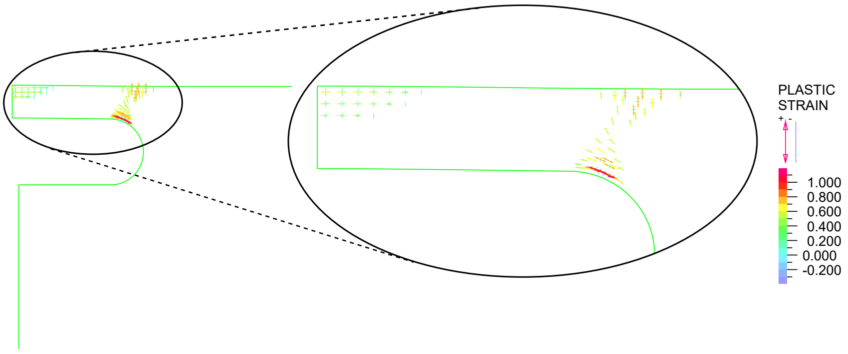

(c) vector plot of directions and magnitudes of the principal plastic strains

Figure A.1: The graphical output of the FE analysis for a sill-like magma chamber with 10 km in diameter and 1.25 km beneath surface, inflated till a localized zone of maximum plastic shear strain interconnected the chamber and surface.

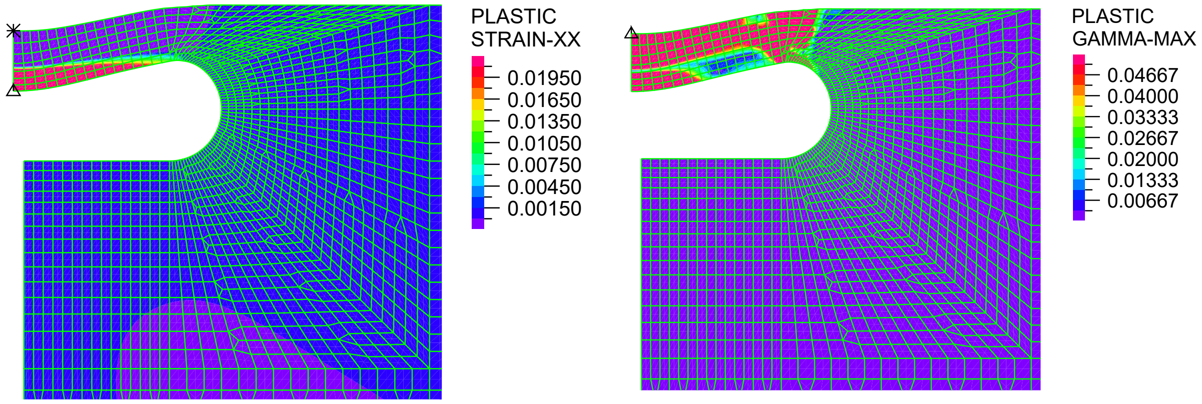

(a) iso-bands of the circumferential plastic normal strain

(b) iso-bands of the maximum plastic shear strain in the radial plane

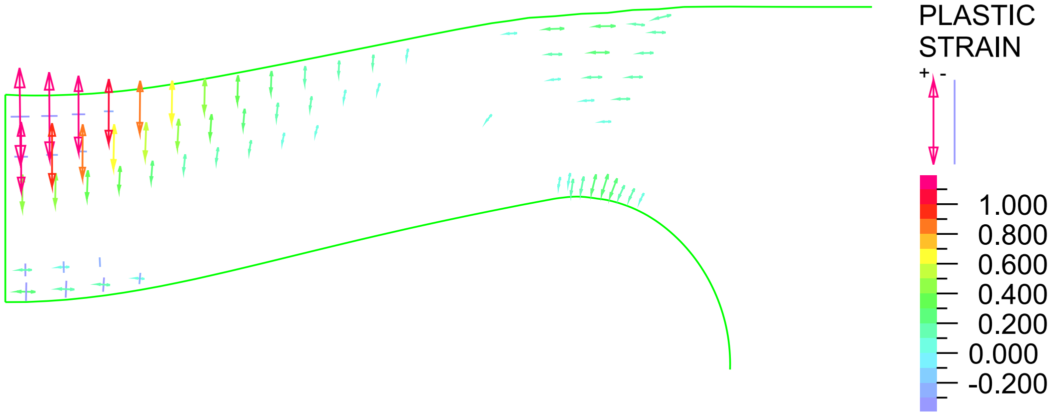

(c) vector plot of directions and magnitudes of the principal plastic strains

Figure A.2: The graphical output of the FE analysis for a sill-like magma chamber with 10 km in diameter and 1.25 km beneath surface, deflated till the onset of underpressure collapse.

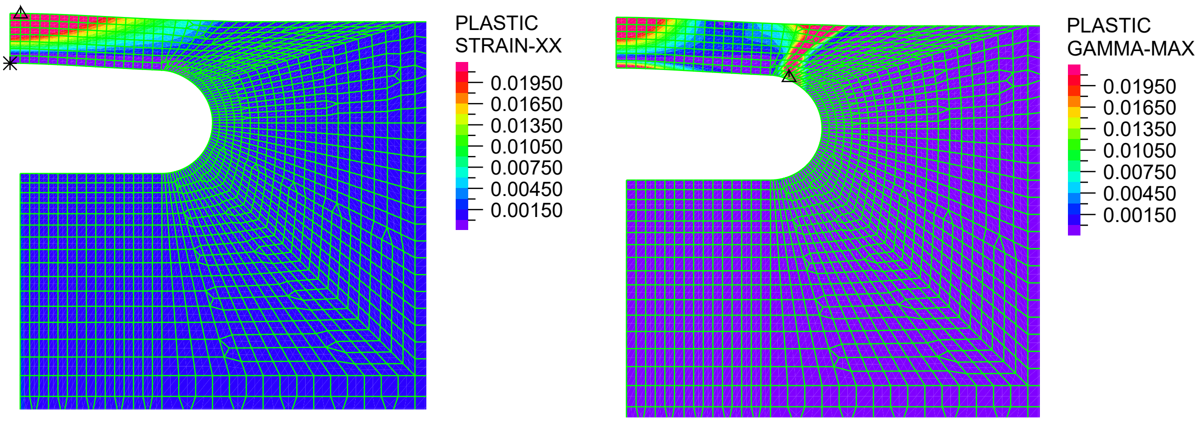

(a) iso-bands of the circumferential plastic normal strain

(b) iso-bands of the maximum plastic shear strain in the radial plane

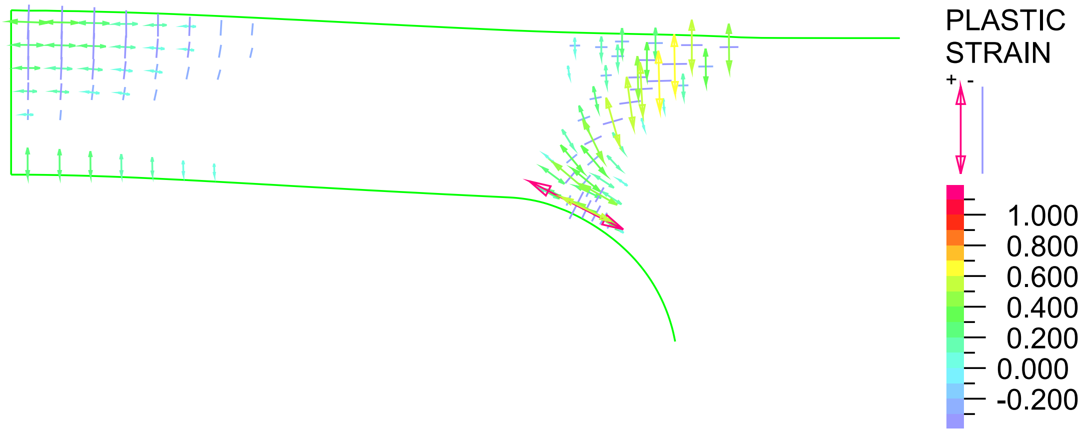

(c) vector plot of directions and magnitudes of the principal plastic strains

Figure A.3: The graphical output of the FE analysis for a sill-like magma chamber with 10 km in diameter and 1.25 km beneath surface, inflated till the onset of overpressure collapse.

Case S-10/2.5

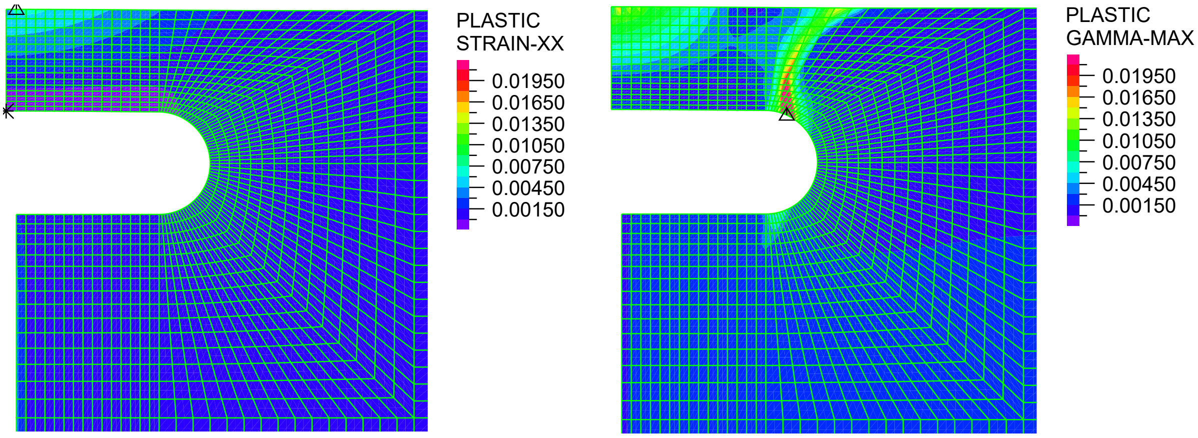

(a) iso-bands of the circumferential plastic normal strain

(b) iso-bands of the maximum plastic shear strain in the radial plane

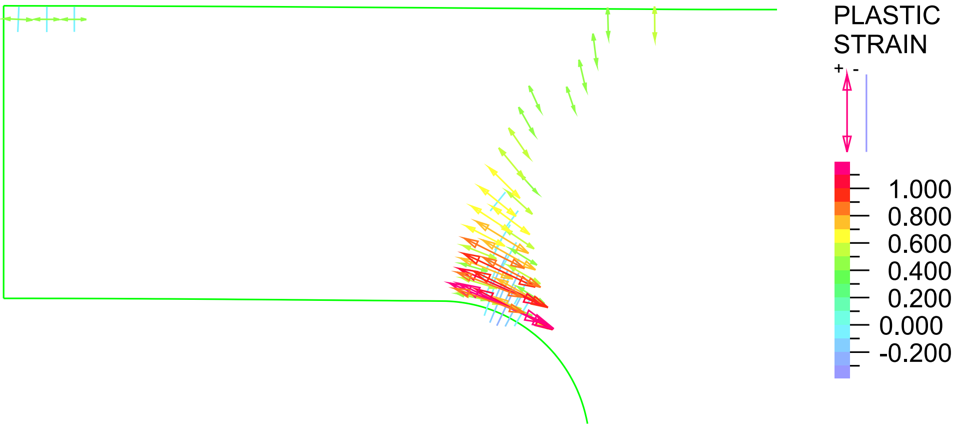

(c) vector plot of directions and magnitudes of the principal plastic strains

Figure A.4: The graphical output of the FE analysis for a sill-like magma chamber with 10 km in diameter and 2.5 km beneath surface, inflated till a localized zone of maximum plastic shear strain interconnected the chamber and surface.

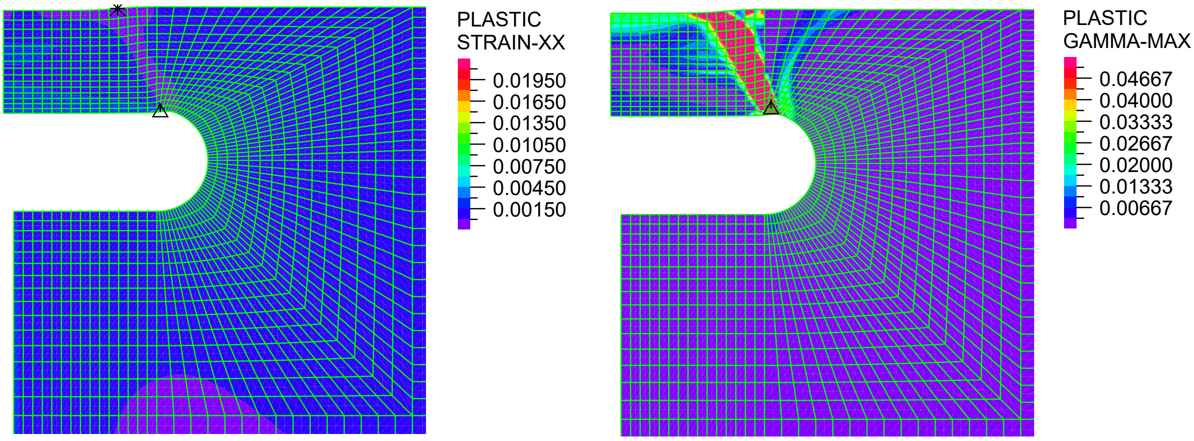

(a) iso-bands of the circumferential plastic normal strain

(b) iso-bands of the maximum plastic shear strain in the radial plane

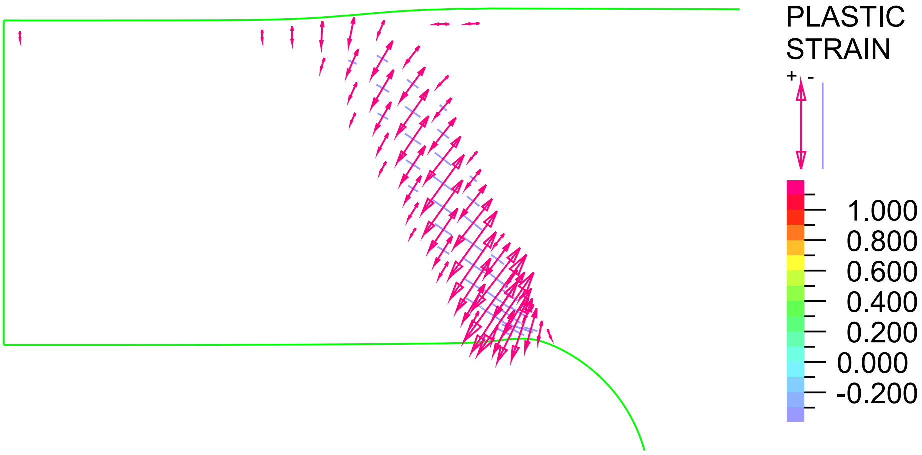

(c) vector plot of directions and magnitudes of the principal plastic strains

Figure A.5: The graphical output of the FE analysis for a sill-like magma chamber with 10 km in diameter and 2.5 km beneath surface, deflated till the onset of underpressure collapse.

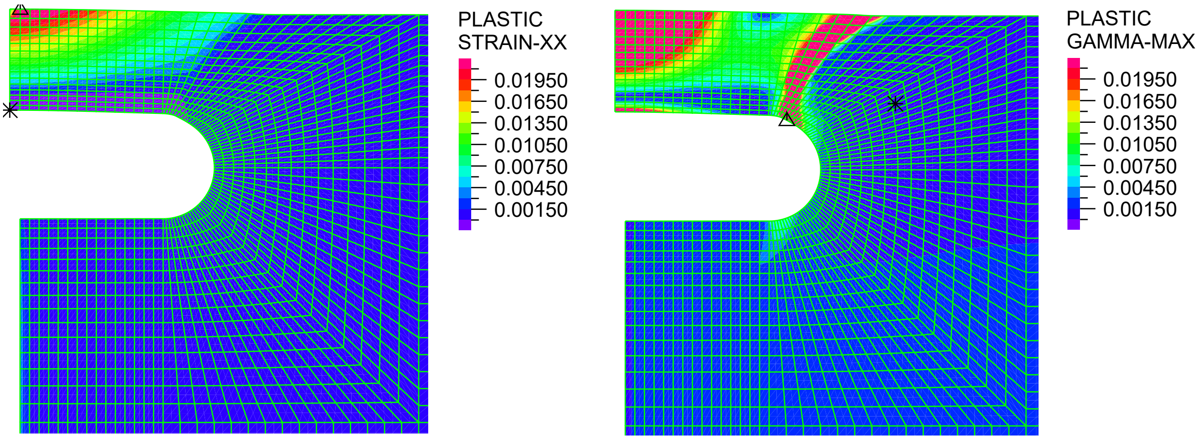

(a) iso-bands of the circumferential plastic normal strain

(b) iso-bands of the maximum plastic shear strain in the radial plane

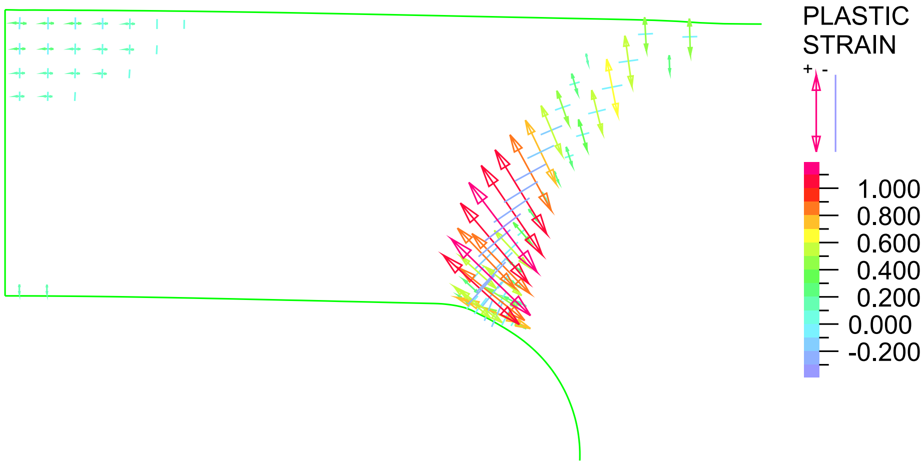

(c) vector plot of directions and magnitudes of the principal plastic strains

Figure A.6: The graphical output of the FE analysis for a sill-like magma chamber with 10 km in diameter and 2.5 km beneath surface, inflated till the onset of overpressure collapse.

Case S-10/5

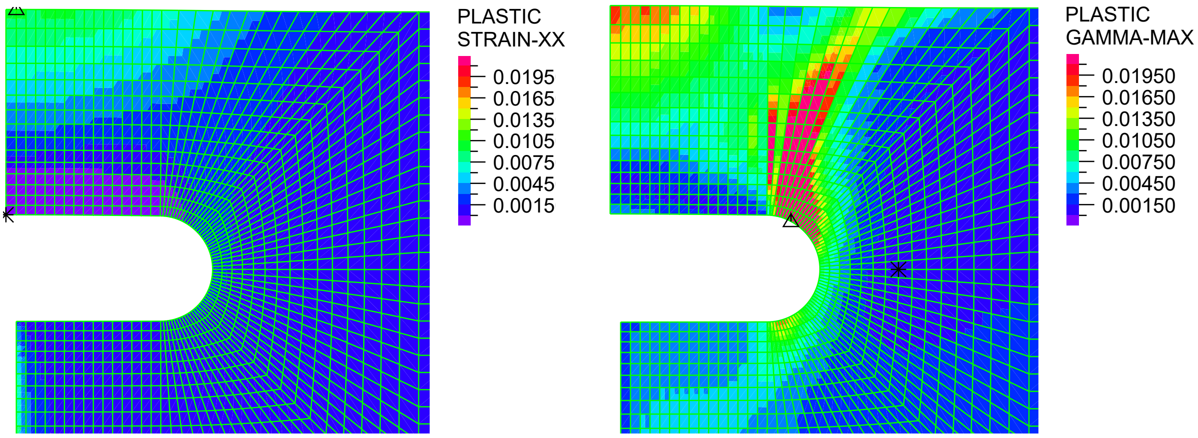

(a) iso-bands of the circumferential plastic normal strain

(b) iso-bands of the maximum plastic shear strain in the radial plane

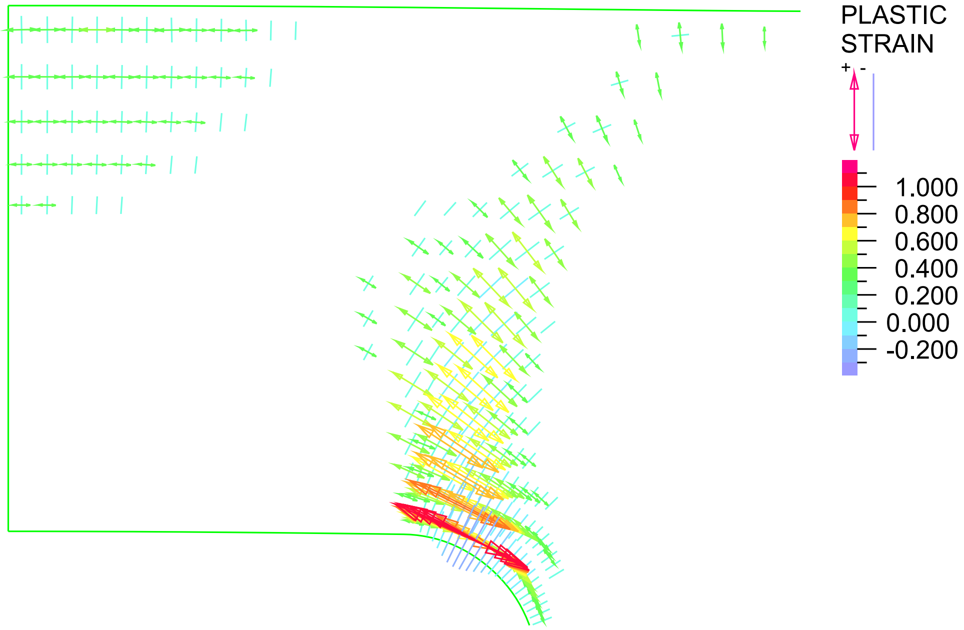

(c) vector plot of directions and magnitudes of the principal plastic strains

Figure A.7: The graphical output of the FE analysis for a sill-like magma chamber with 10 km in diameter and 5 km beneath surface, inflated till a localized zone of maximum plastic shear strain interconnected the chamber and surface.

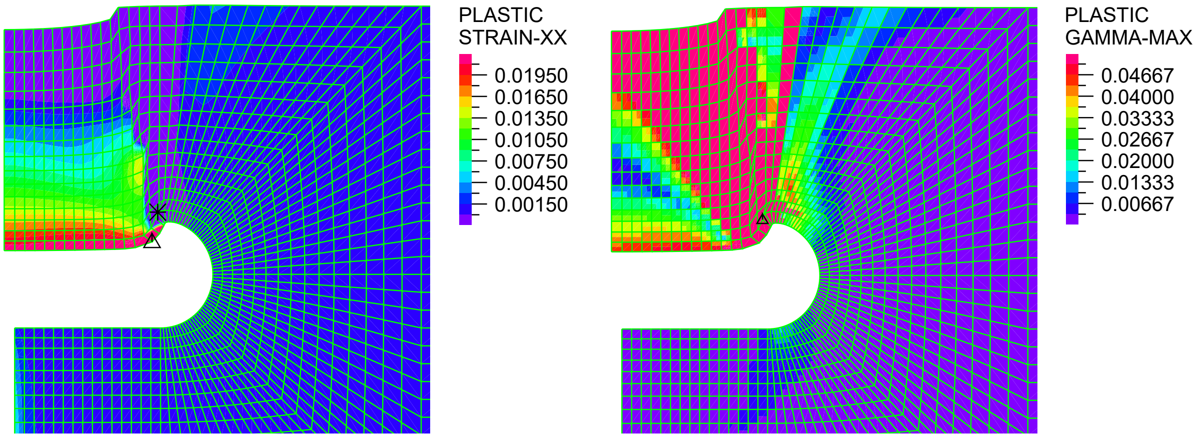

(a) iso-bands of the circumferential plastic normal strain

(b) iso-bands of the maximum plastic shear strain in the radial plane

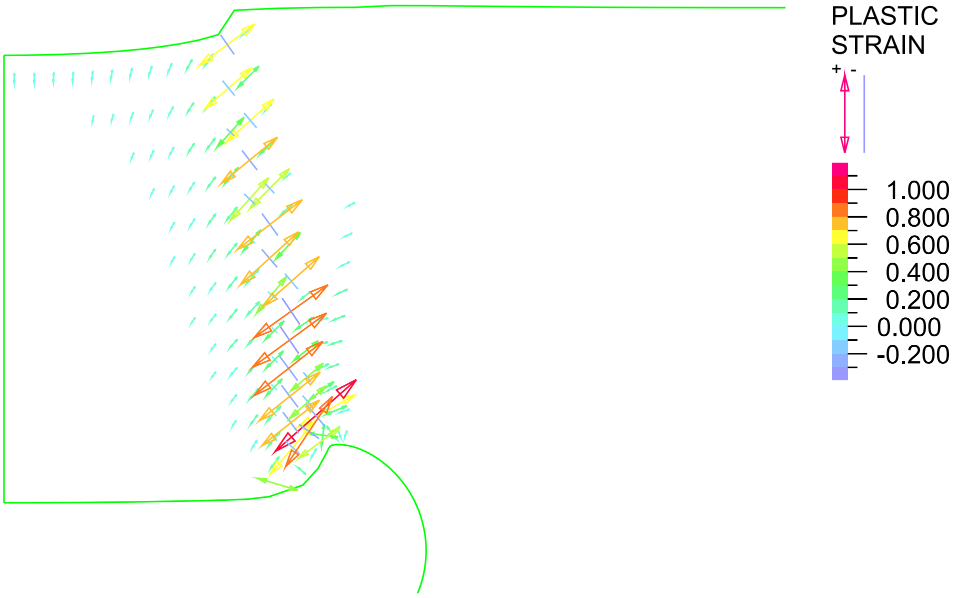

(c) vector plot of directions and magnitudes of the principal plastic strains

Figure A.8: The graphical output of the FE analysis for a sill-like magma chamber with 10 km in diameter and 5 km beneath surface, deflated till the onset of underpressure collapse.

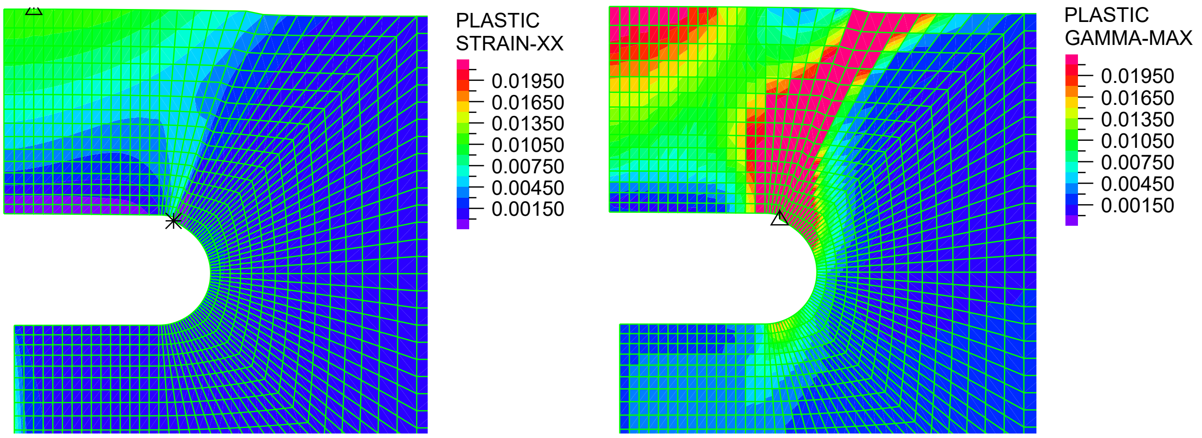

(a) iso-bands of the circumferential plastic normal strain

(b) iso-bands of the maximum plastic shear strain in the radial plane

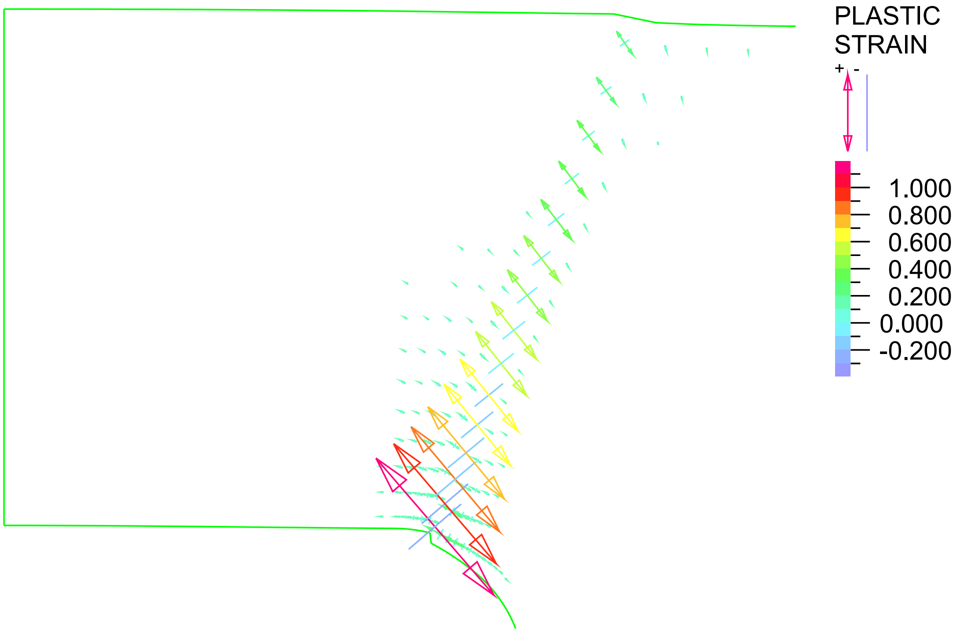

(c) vector plot of directions and magnitudes of the principal plastic strains

Figure A.9: The graphical output of the FE analysis for a sill-like magma chamber with 10 km in diameter and 5 km beneath surface, inflated till the onset of overpressure collapse.

Case S-10/7.5

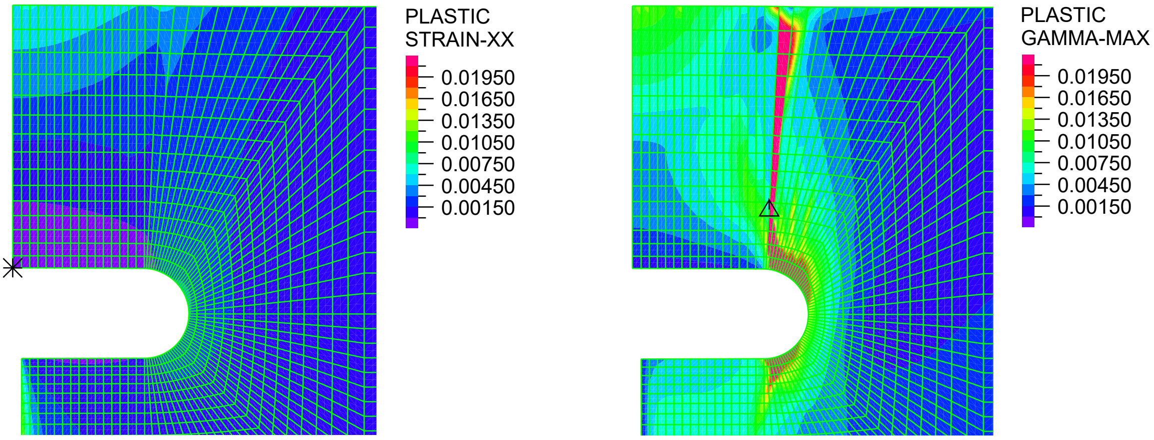

(a) iso-bands of the circumferential plastic normal strain

(b) iso-bands of the maximum plastic shear strain in the radial plane

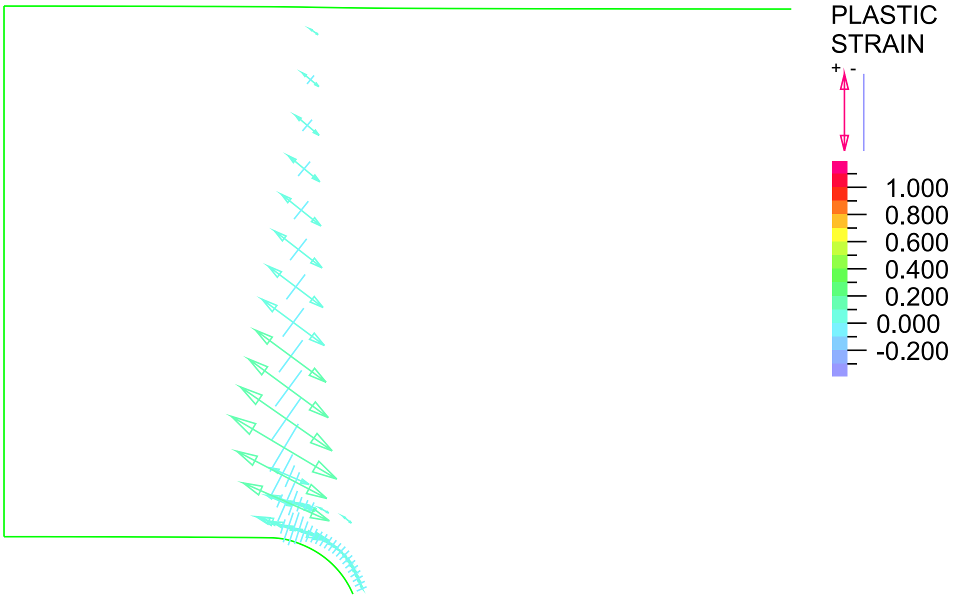

(c) vector plot of directions and magnitudes of the principal plastic strains

Figure A.10: The graphical output of the FE analysis for a sill-like magma chamber with 10 km in diameter and 7.5 km beneath surface, inflated till a localized zone of maximum plastic shear strain interconnected the chamber and surface.

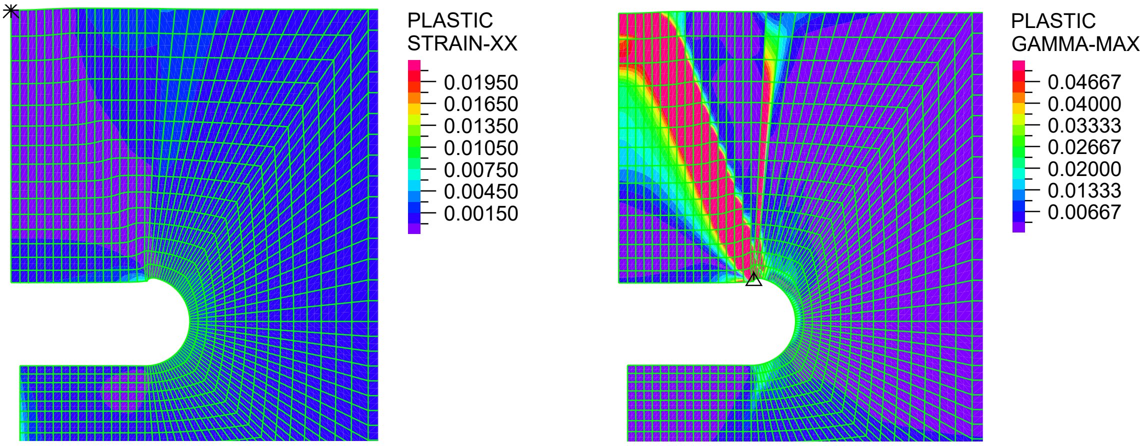

(a) iso-bands of the circumferential plastic normal strain

(b) iso-bands of the maximum plastic shear strain in the radial plane

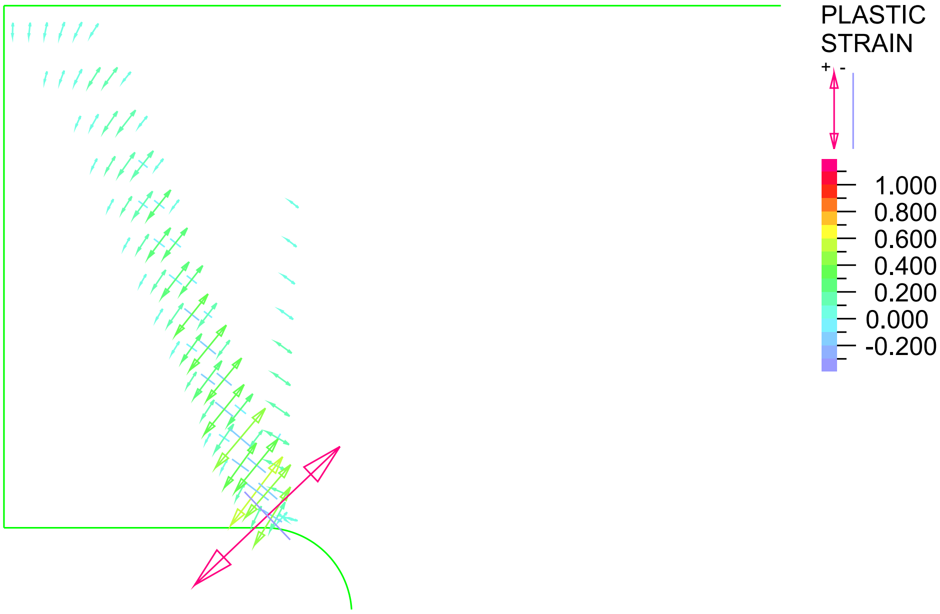

(c) vector plot of directions and magnitudes of the principal plastic strains

Figure A.11: The graphical output of the FE analysis for a sill-like magma chamber with 10 km in diameter and 7.5 km beneath surface, deflated till the onset of underpressure collapse.

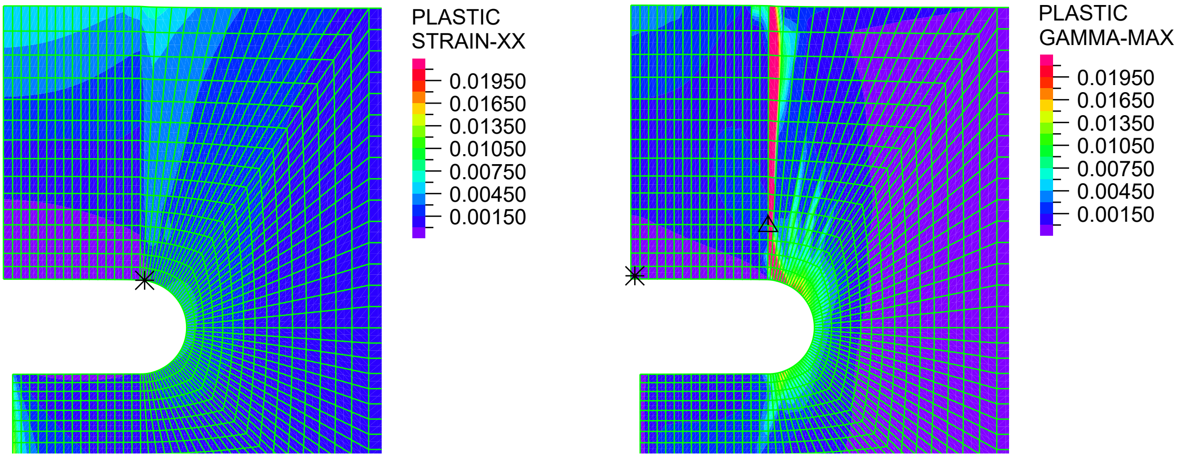

(a) iso-bands of the circumferential plastic normal strain

(b) iso-bands of the maximum plastic shear strain in the radial plane

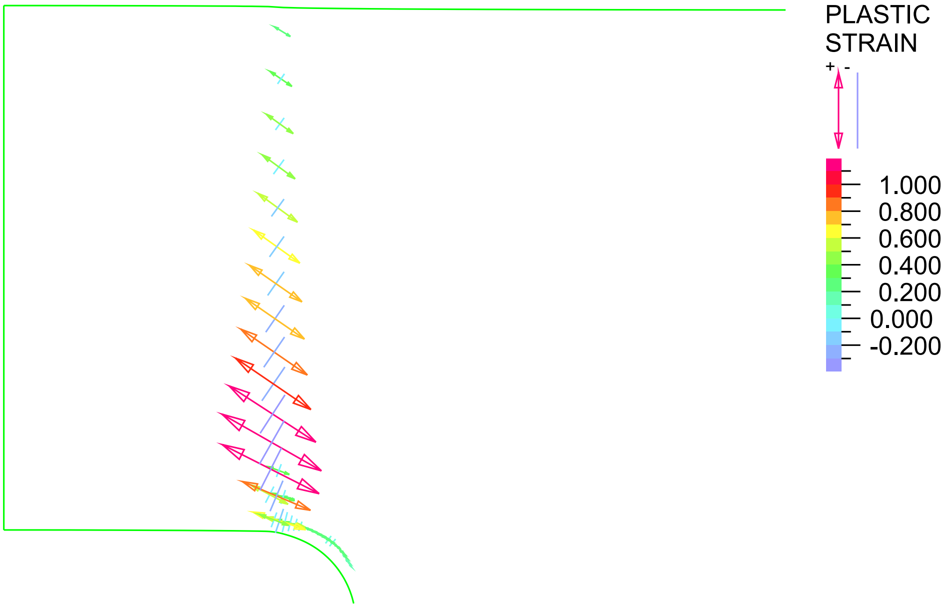

(c) vector plot of directions and magnitudes of the principal plastic strains

Figure A.12: The graphical output of the FE analysis for a sill-like magma chamber with 10 km in diameter and 7.5 km beneath surface, inflated till the onset of overpressure collapse.

Case S-10/10

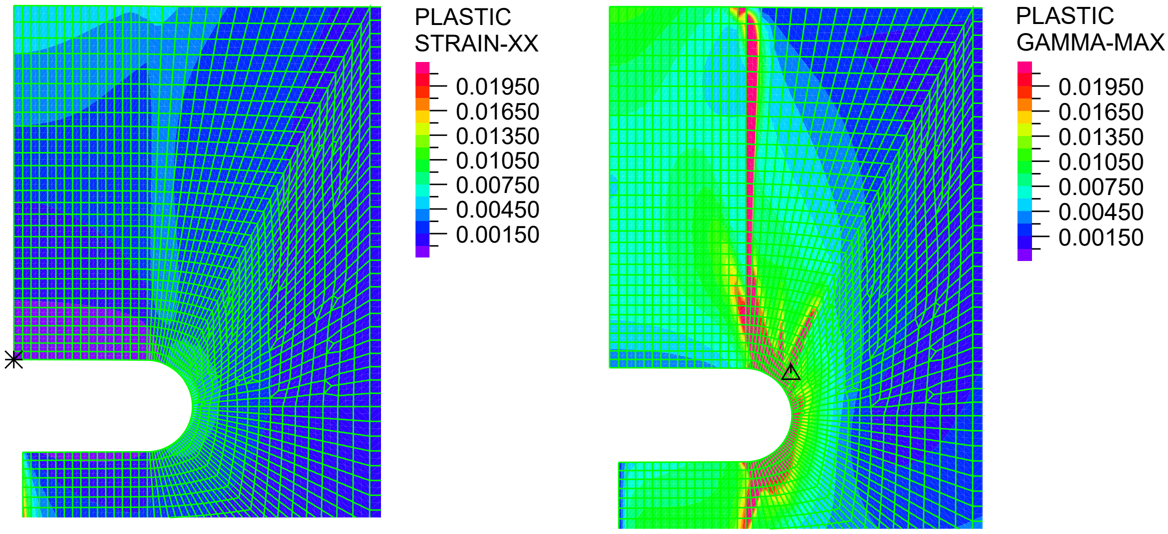

(a) iso-bands of the circumferential plastic normal strain

(b) iso-bands of the maximum plastic shear strain in the radial plane

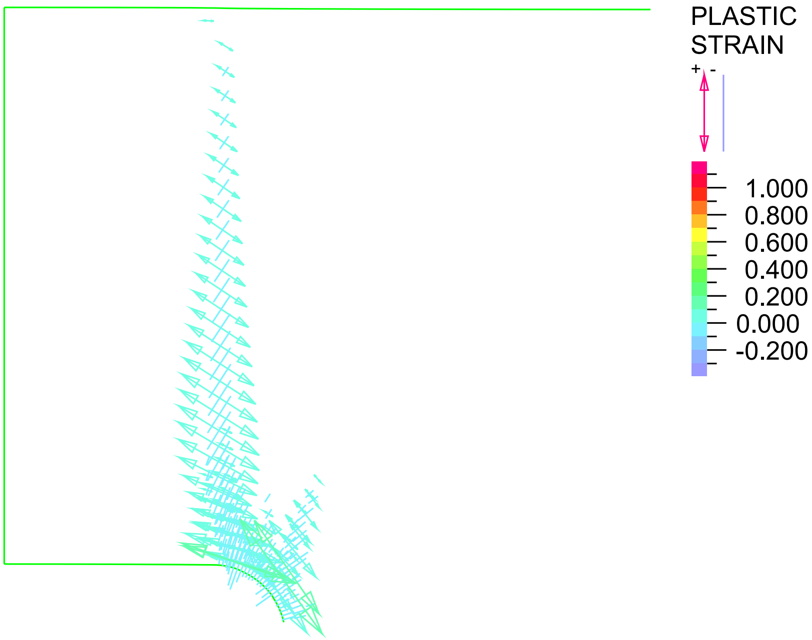

(c) vector plot of directions and magnitudes of the principal plastic strains

Figure A.13: The graphical output of the FE analysis for a sill-like magma chamber with 10 km in diameter and 10 km beneath surface, inflated till a localized zone of maximum plastic shear strain interconnected the chamber and surface.

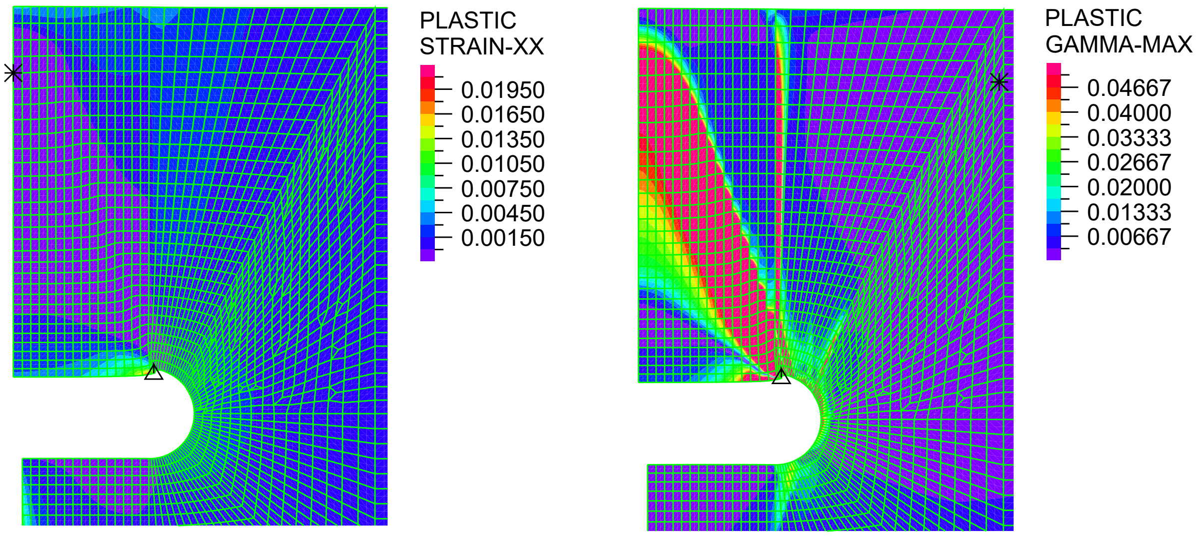

(a) iso-bands of the circumferential plastic normal strain

(b) iso-bands of the maximum plastic shear strain in the radial plane

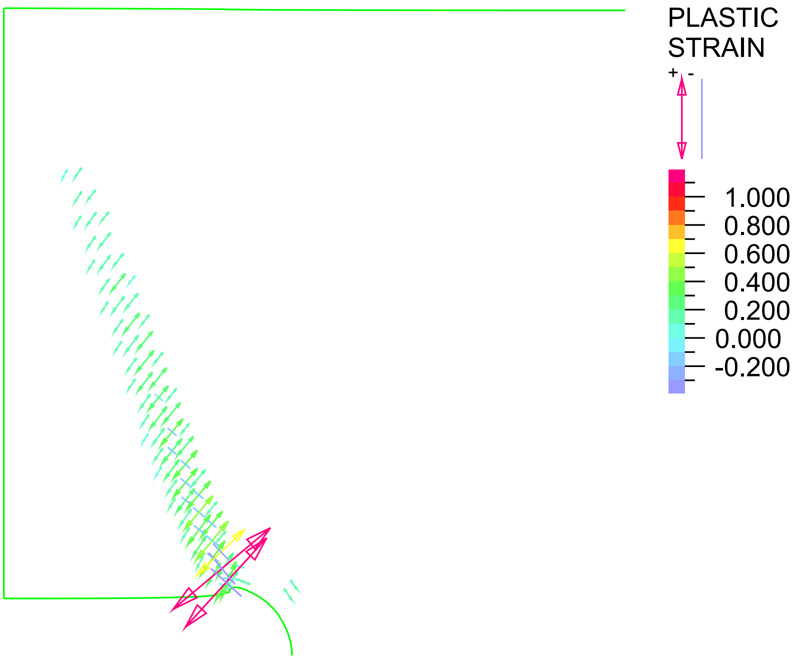

(c) vector plot of directions and magnitudes of the principal plastic strains

Figure A.14: The graphical output of the FE analysis for a sill-like magma chamber with 10 km in diameter and 10 km beneath surface, deflated till the onset of underpressure collapse.

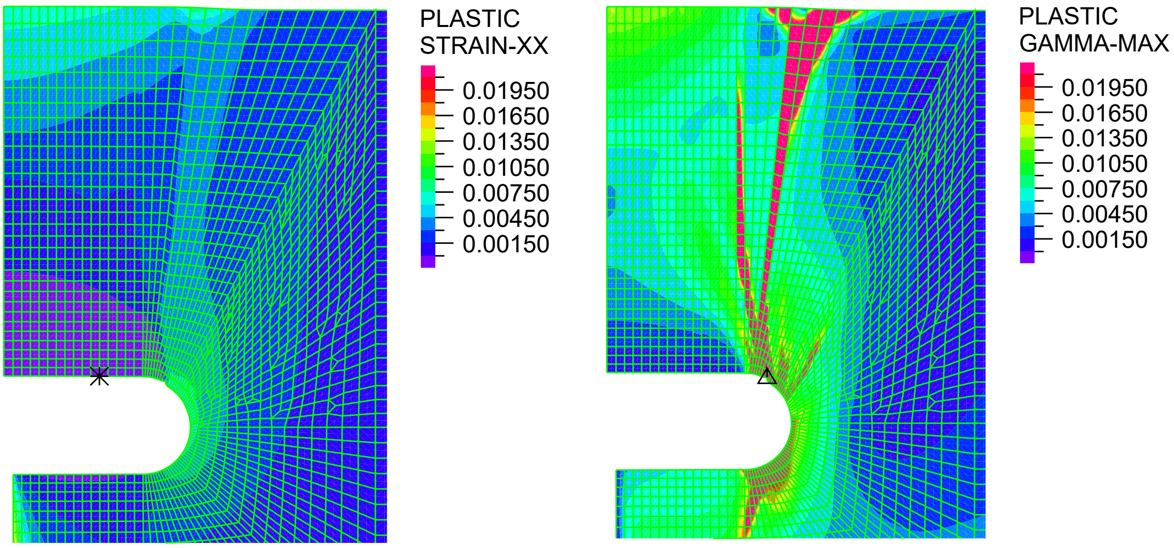

(a) iso-bands of the circumferential plastic normal strain

(b) iso-bands of the maximum plastic shear strain in the radial plane

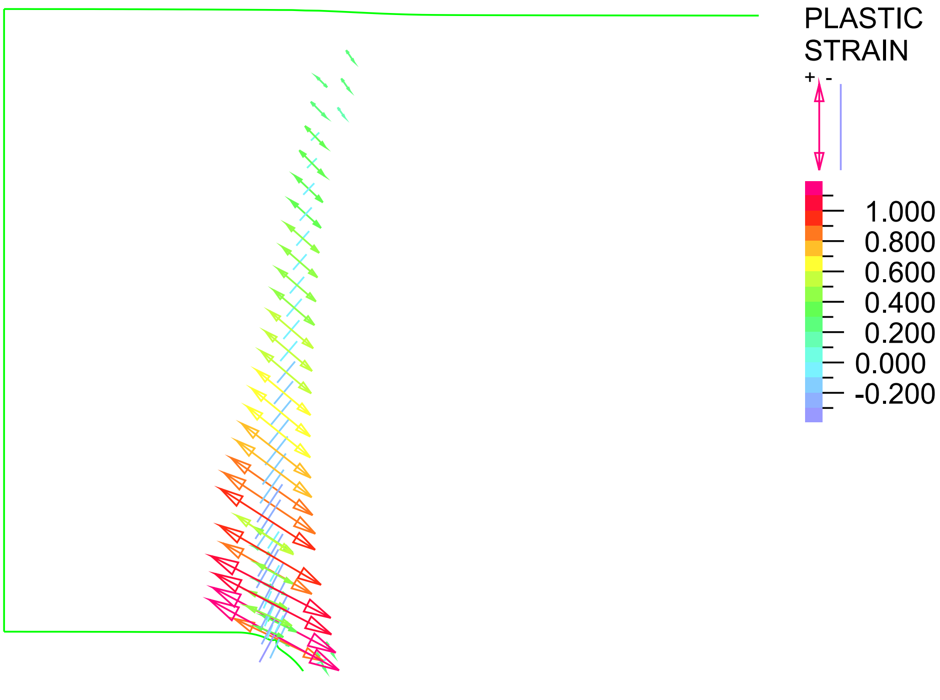

(c) vector plot of directions and magnitudes of the principal plastic strains

Figure A.15: The graphical output of the FE analysis for a sill-like magma chamber with 10 km in diameter and 10 km beneath surface, inflated till the onset of overpressure collapse.

Case S-50/5

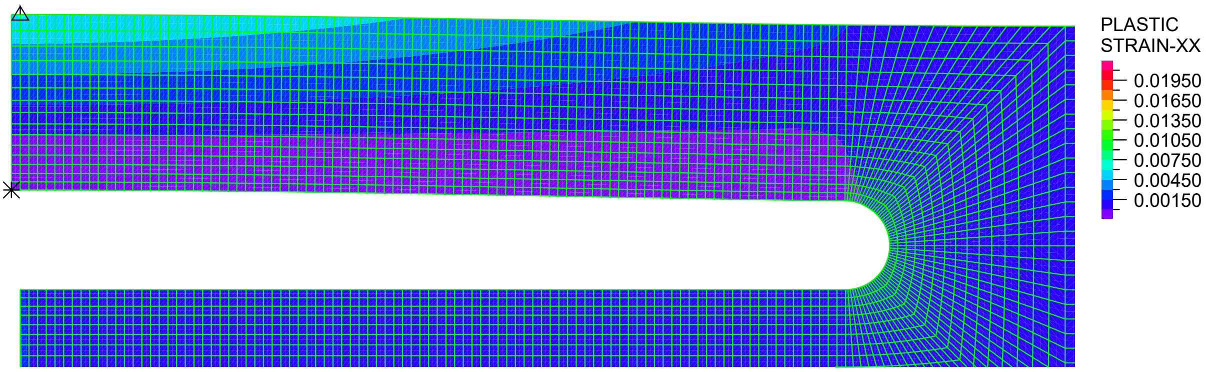

(a) iso-bands of the circumferential plastic normal strain

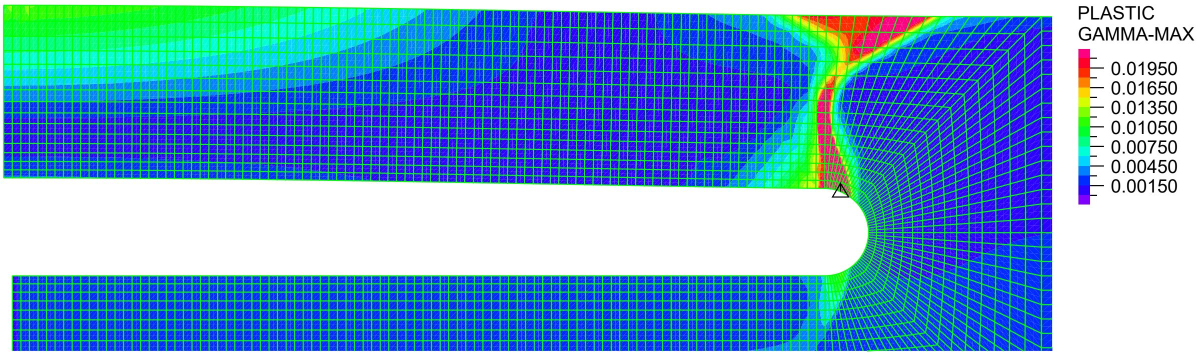

(b) iso-bands of the maximum plastic shear strain in the radial plane

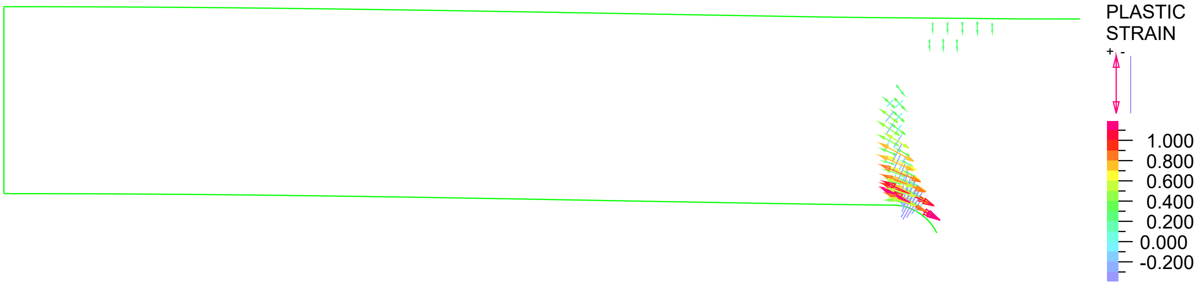

(c) vector plot of directions and magnitudes of the principal plastic strains

Figure A.16: The graphical output of the FE analysis for a sill-like magma chamber with 50 km in diameter and 5 km beneath surface, inflated till a localized zone of maximum plastic shear strain interconnected the chamber and surface.

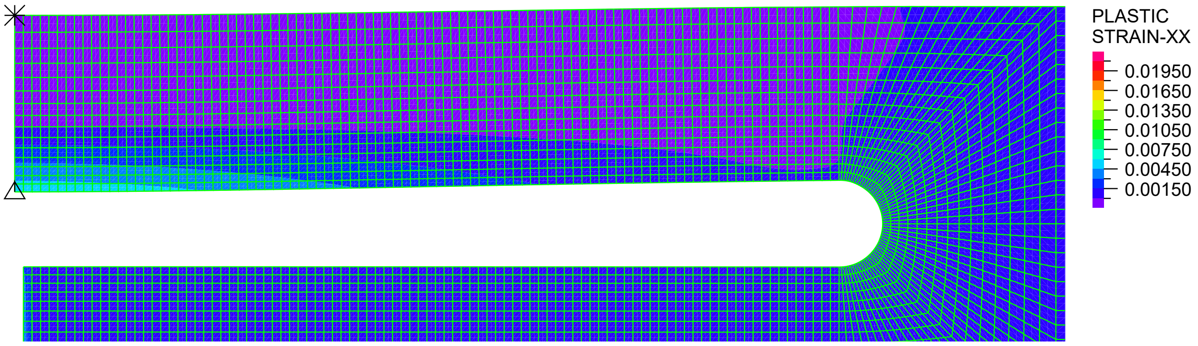

(a) iso-bands of the circumferential plastic normal strain

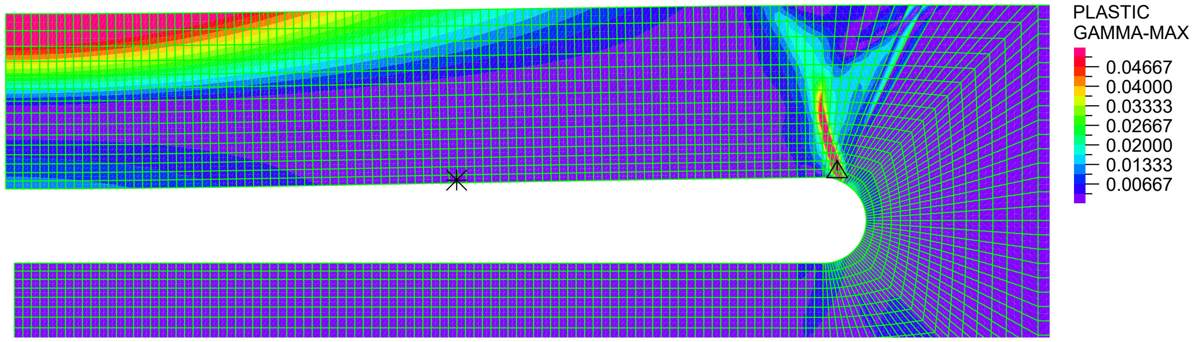

(b) iso-bands of the maximum plastic shear strain in the radial plane

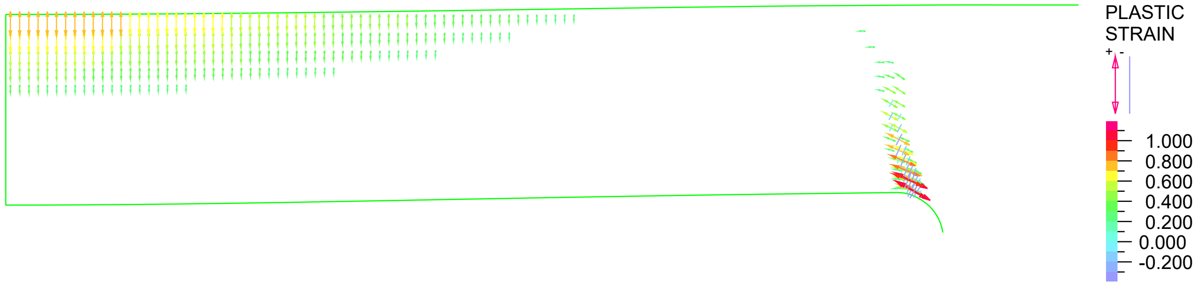

(c) vector plot of directions and magnitudes of the principal plastic strains

Figure A.17: The graphical output of the FE analysis for a sill-like magma chamber with 50 km in diameter and 5 km beneath surface, deflated till the onset of underpressure collapse.

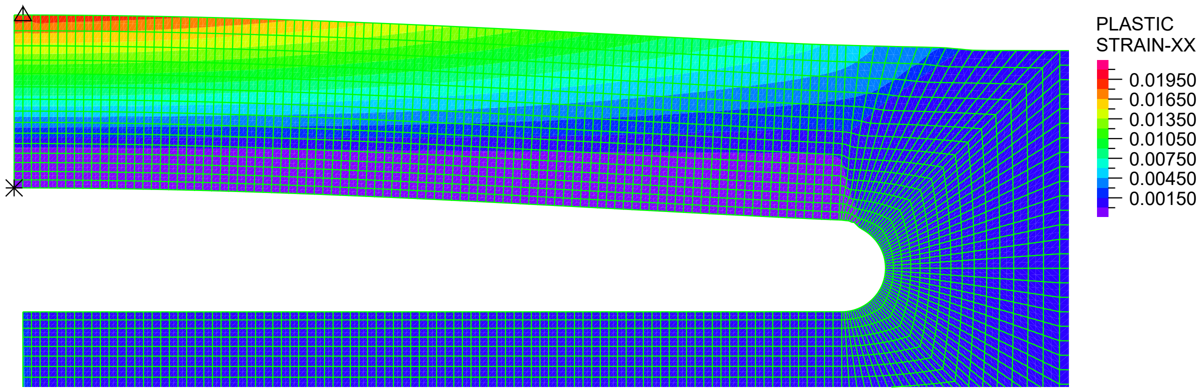

(a) iso-bands of the circumferential plastic normal strain

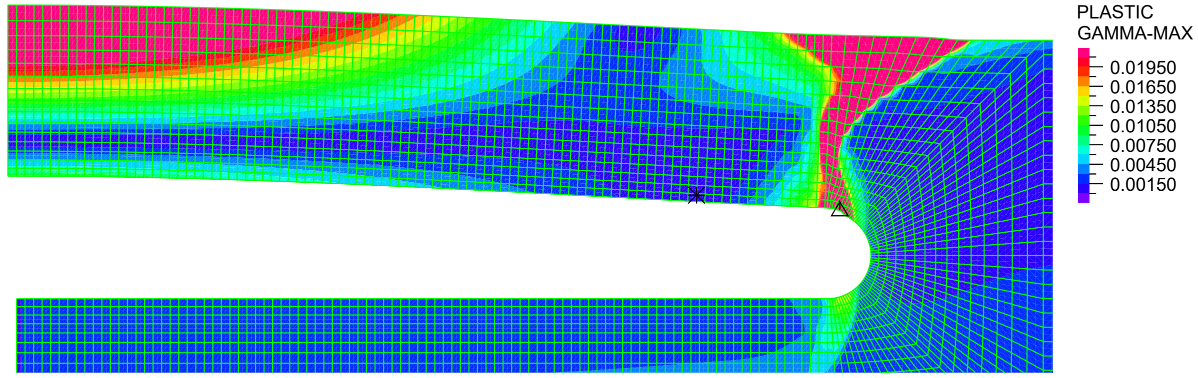

(b) iso-bands of the maximum plastic shear strain in the radial plane

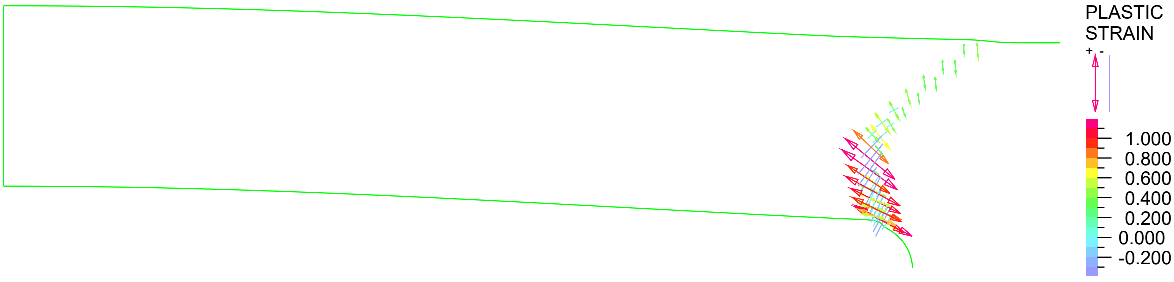

(c) vector plot of directions and magnitudes of the principal plastic strains

Figure A.18: The graphical output of the FE analysis for a sill-like magma chamber with 50 km in diameter and 5 km beneath surface, inflated till the onset of overpressure collapse.

Case S-50/7.5

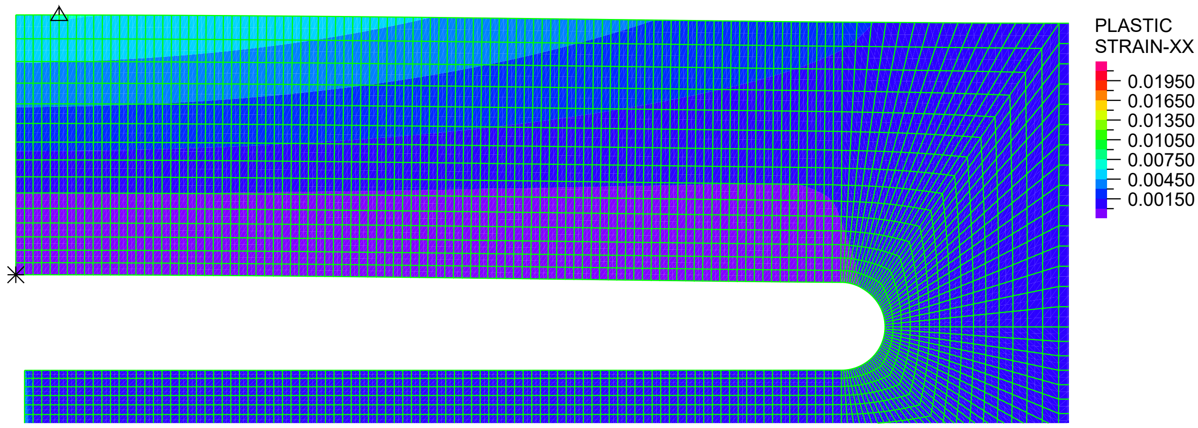

(a) iso-bands of the circumferential plastic normal strain

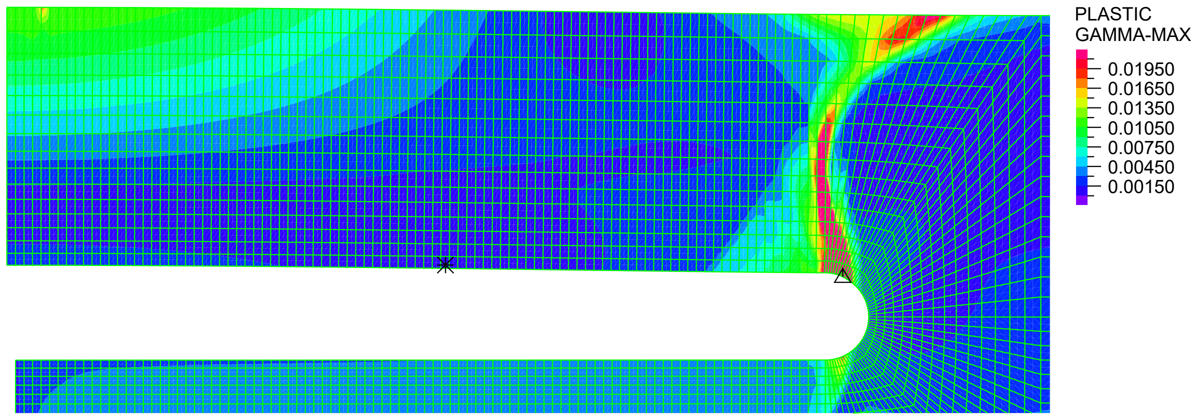

(b) iso-bands of the maximum plastic shear strain in the radial plane

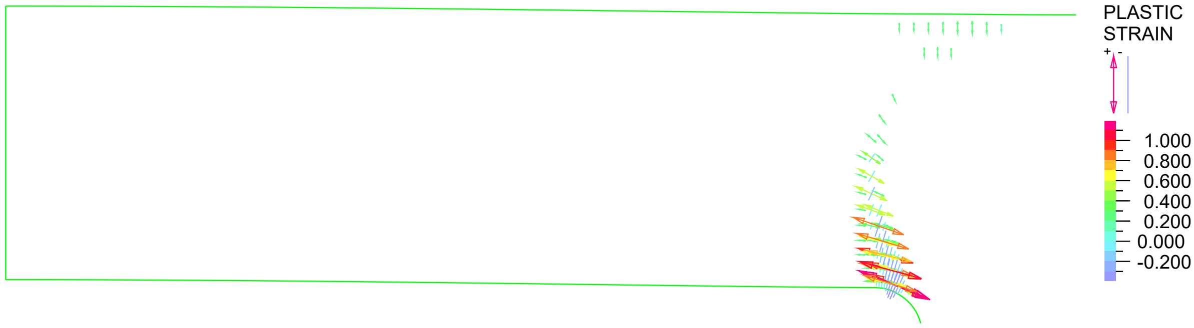

(c) vector plot of directions and magnitudes of the principal plastic strains

Figure A.19: The graphical output of the FE analysis for a sill-like magma chamber with 50 km in diameter and 7.5 km beneath surface, inflated till a localized zone of maximum plastic shear strain interconnected the chamber and surface.

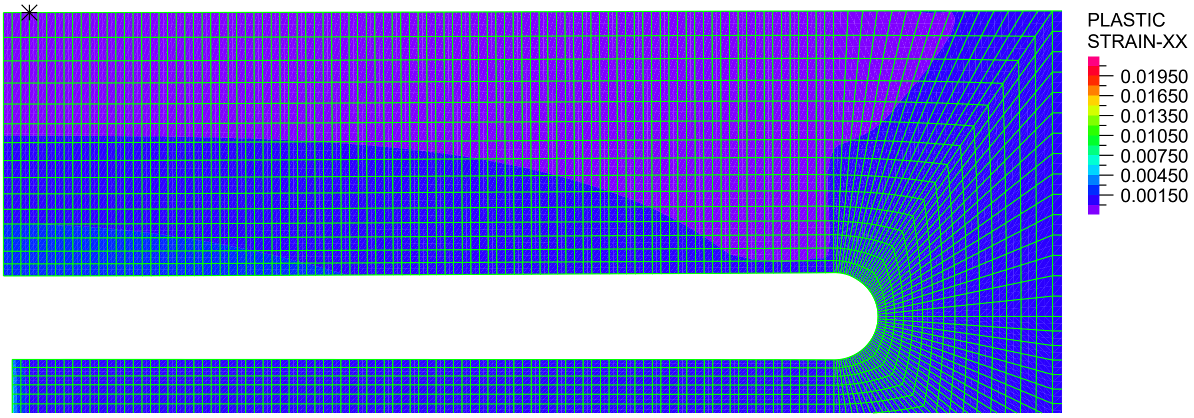

(a) iso-bands of the circumferential plastic normal strain

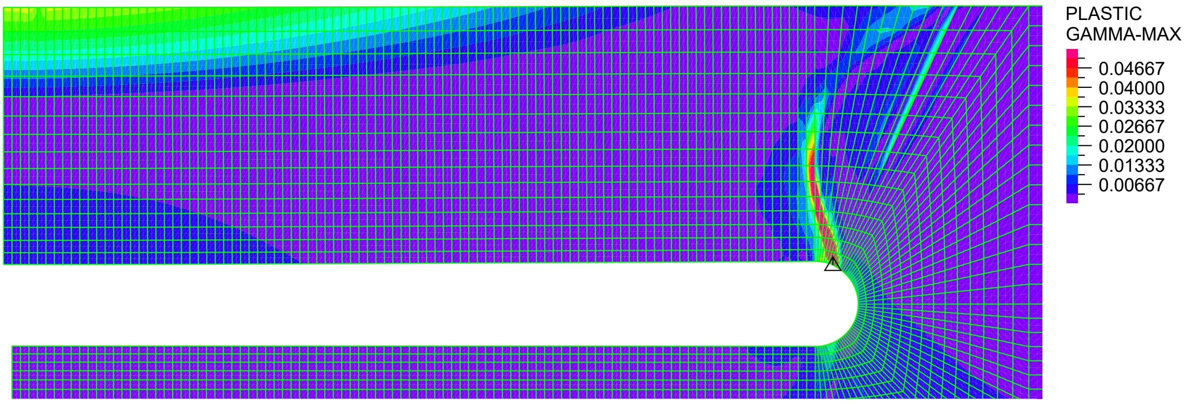

(b) iso-bands of the maximum plastic shear strain in the radial plane

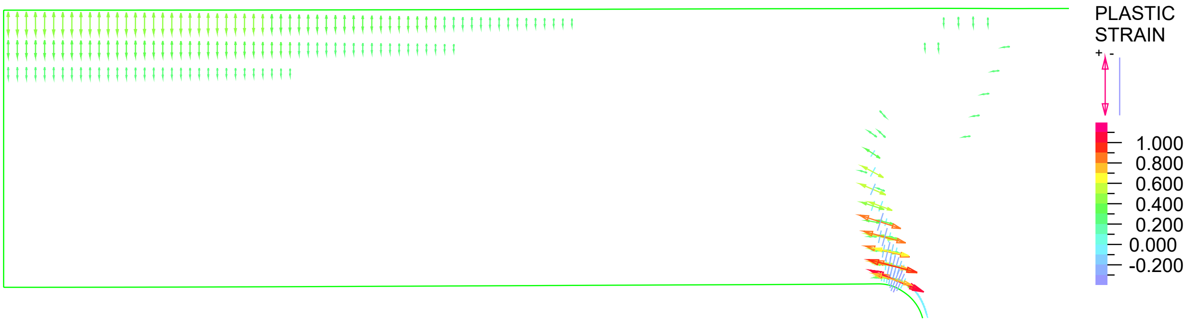

(c) vector plot of directions and magnitudes of the principal plastic strains

Figure A.20: The graphical output of the FE analysis for a sill-like magma chamber with 50 km in diameter and 7.5 km beneath surface, deflated till the onset of underpressure collapse.

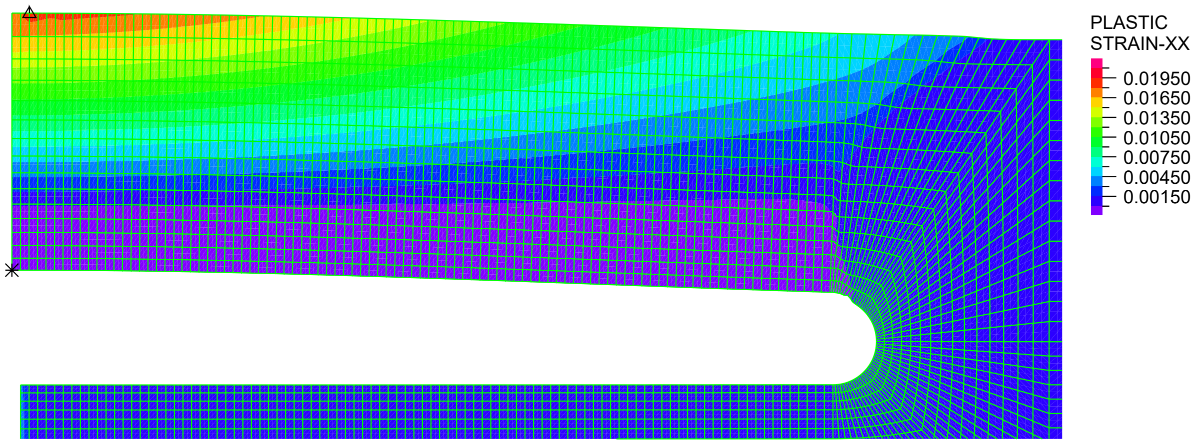

(a) iso-bands of the circumferential plastic normal strain

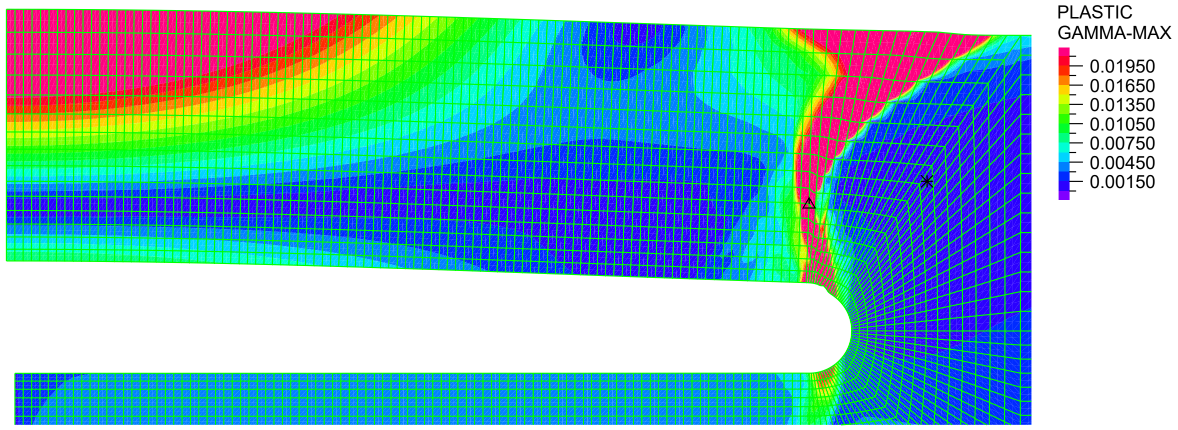

(b) iso-bands of the maximum plastic shear strain in the radial plane

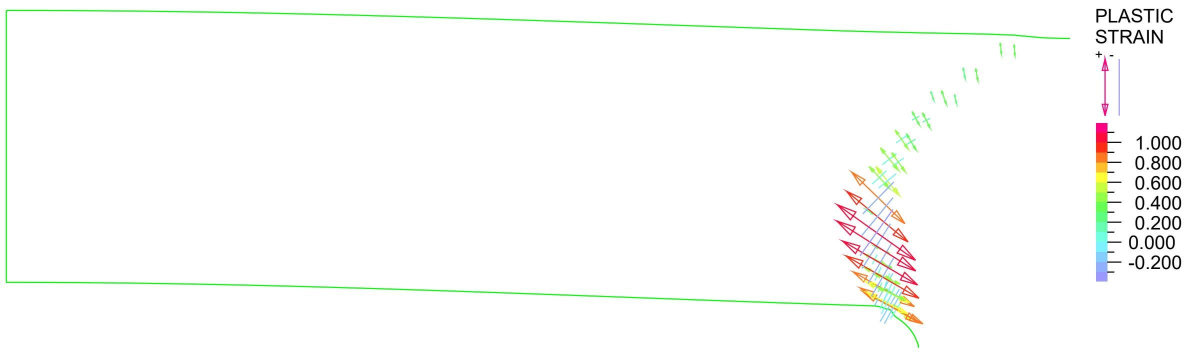

(c) vector plot of directions and magnitudes of the principal plastic strains

Figure A.21: The graphical output of the FE analysis for a sill-like magma chamber with 50 km in diameter and 7.5 km beneath surface, inflated till the onset of overpressure collapse.

Case S-50/10

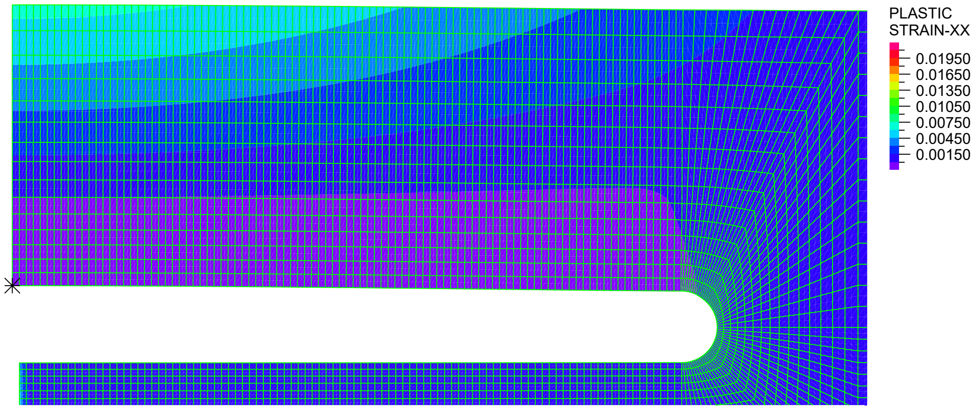

(a) iso-bands of the circumferential plastic normal strain

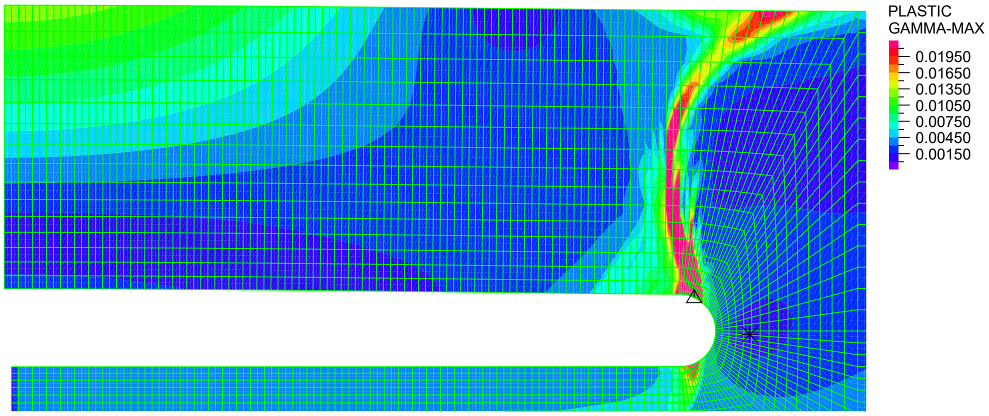

(b) iso-bands of the maximum plastic shear strain in the radial plane

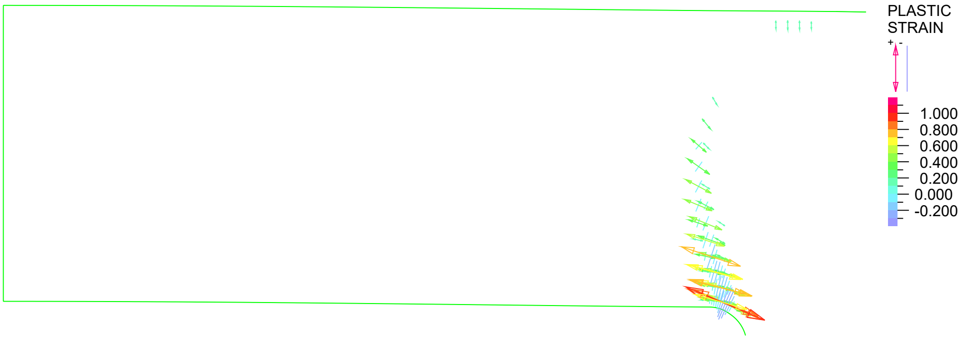

(c) vector plot of directions and magnitudes of the principal plastic strains

Figure A.22: The graphical output of the FE analysis for a sill-like magma chamber with 50 km in diameter and 10 km beneath surface, inflated till a localized zone of maximum plastic shear strain interconnected the chamber and surface.

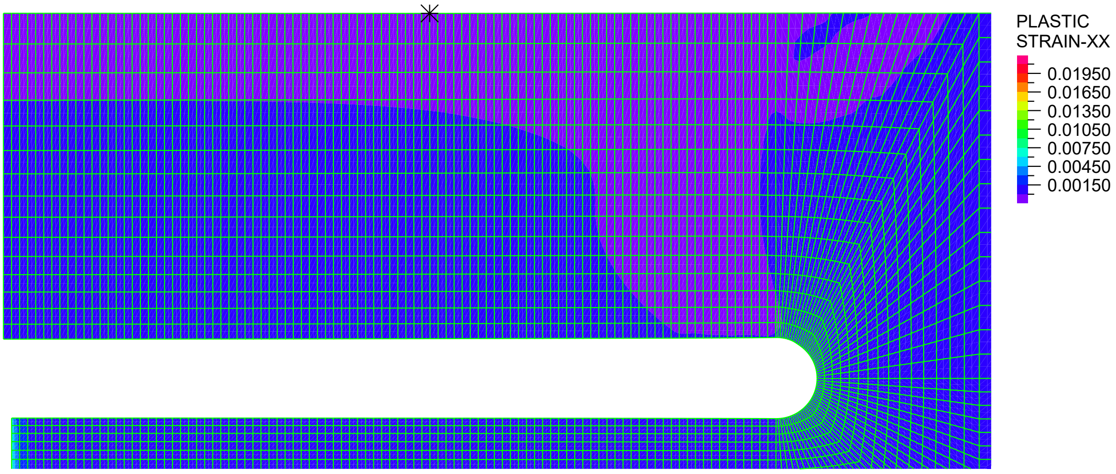

(a) iso-bands of the circumferential plastic normal strain

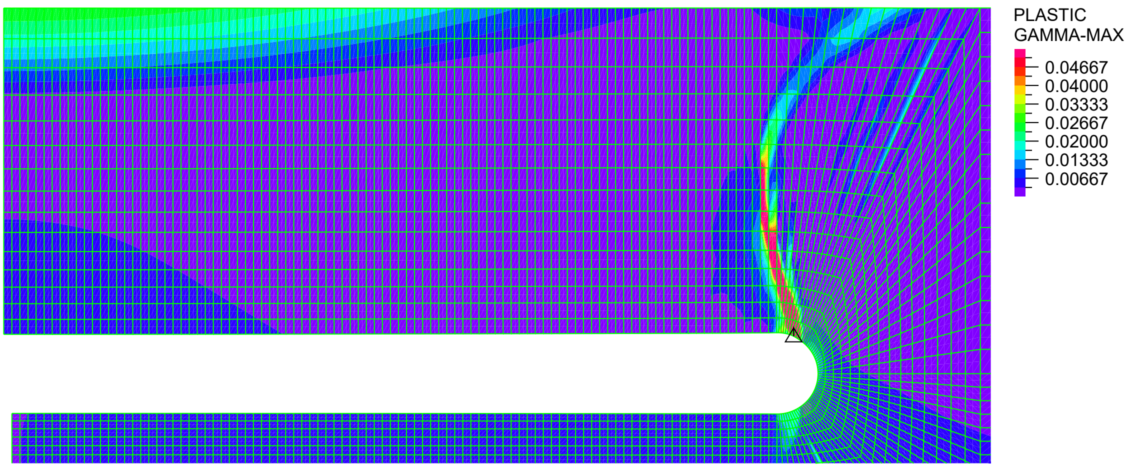

(b) iso-bands of the maximum plastic shear strain in the radial plane

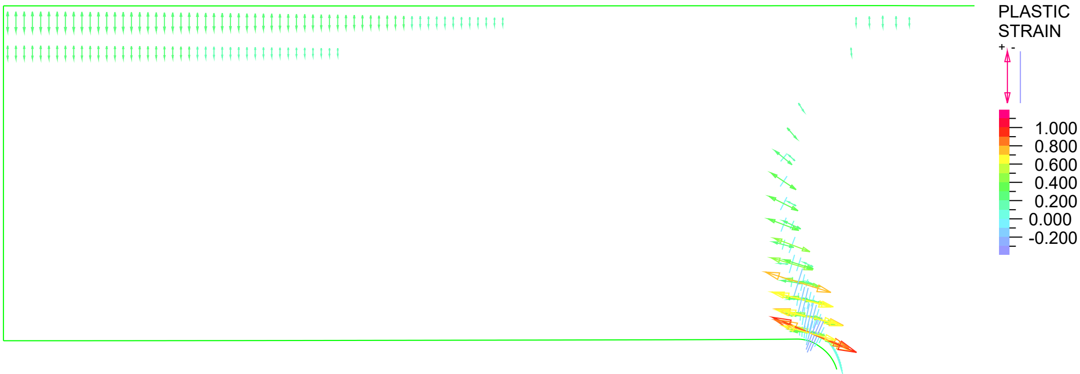

(c) vector plot of directions and magnitudes of the principal plastic strains

Figure A.23: The graphical output of the FE analysis for a sill-like magma chamber with 50 km in diameter and 10 km beneath surface, deflated till the onset of underpressure collapse.

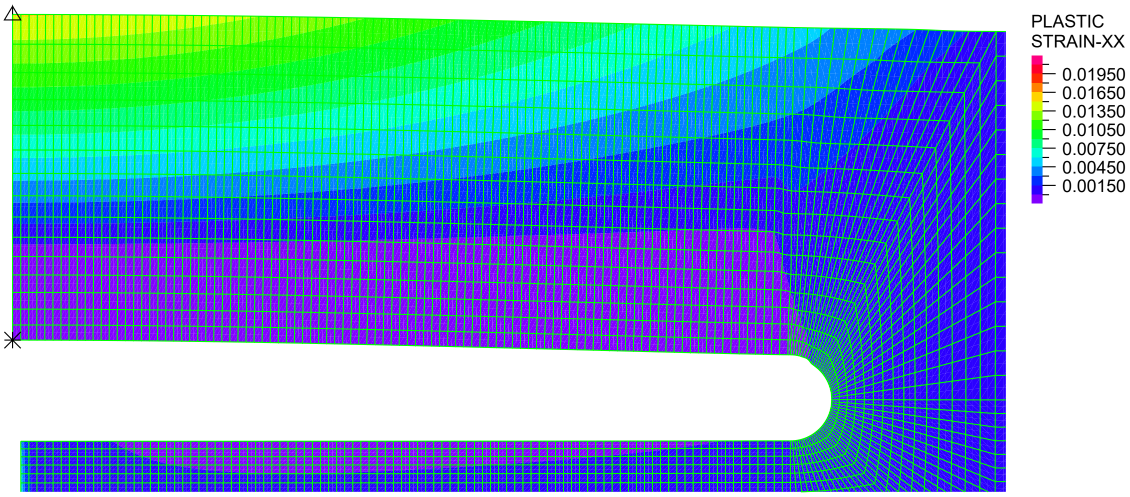

(a) iso-bands of the circumferential plastic normal strain

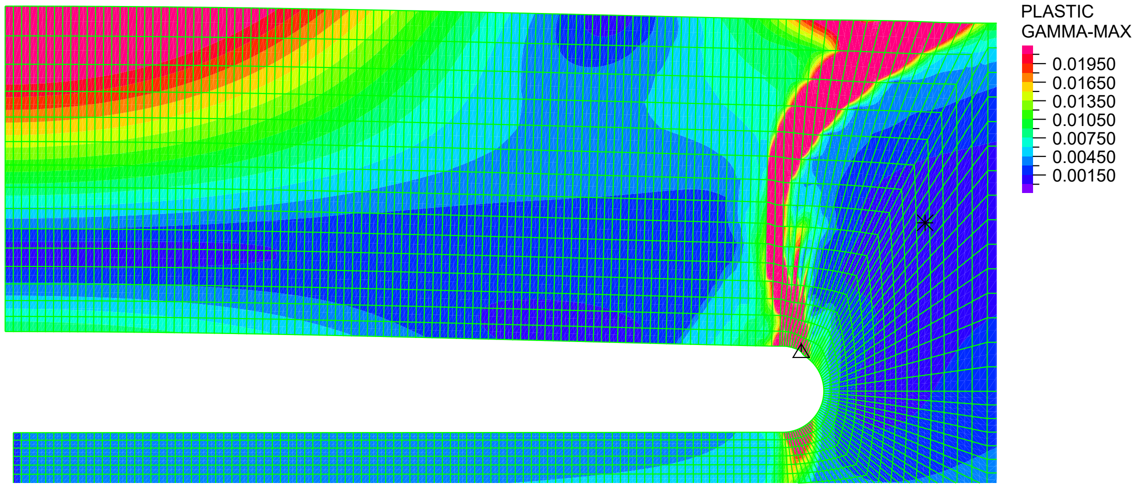

(b) iso-bands of the maximum plastic shear strain in the radial plane

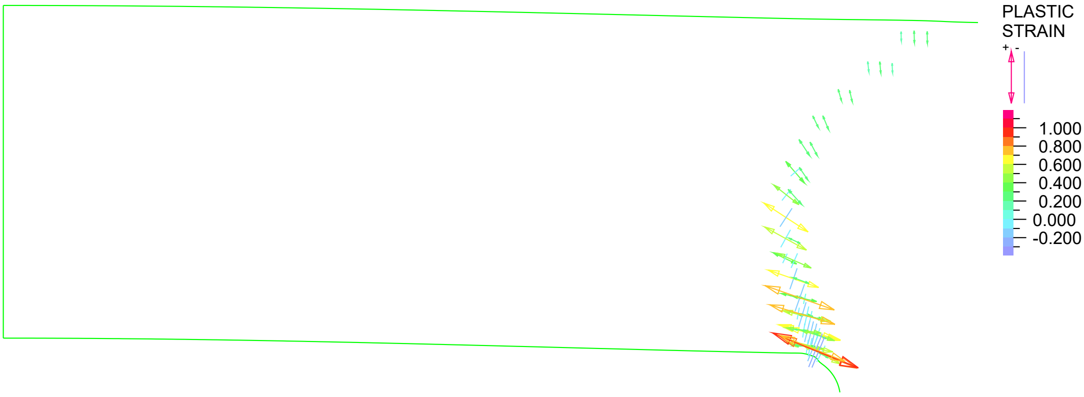

(c) vector plot of directions and magnitudes of the principal plastic strains

Figure A.24: The graphical output of the FE analysis for a sill-like magma chamber with 50 km in diameter and 10 km beneath surface, inflated till the onset of overpressure collapse.

Case B-10/5

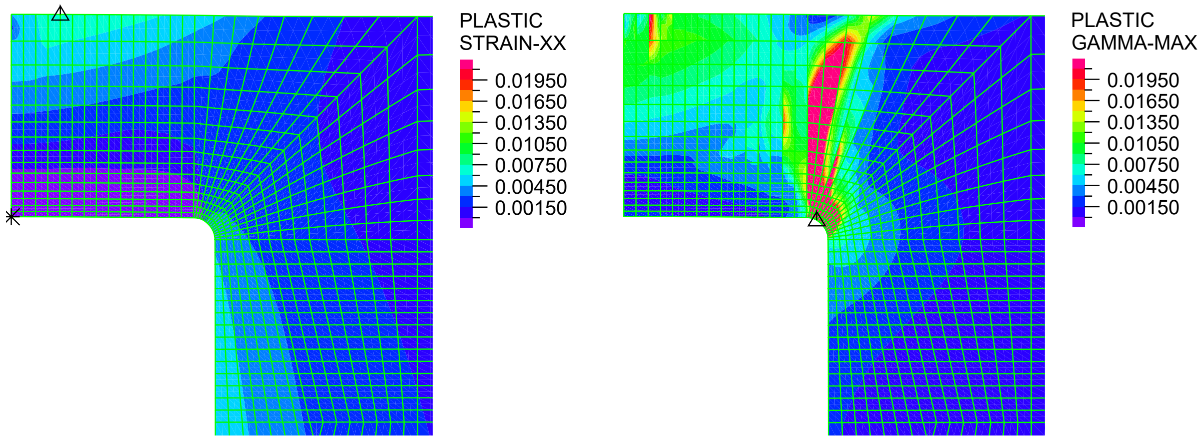

(a) iso-bands of the circumferential plastic normal strain

(b) iso-bands of the maximum plastic shear strain in the radial plane

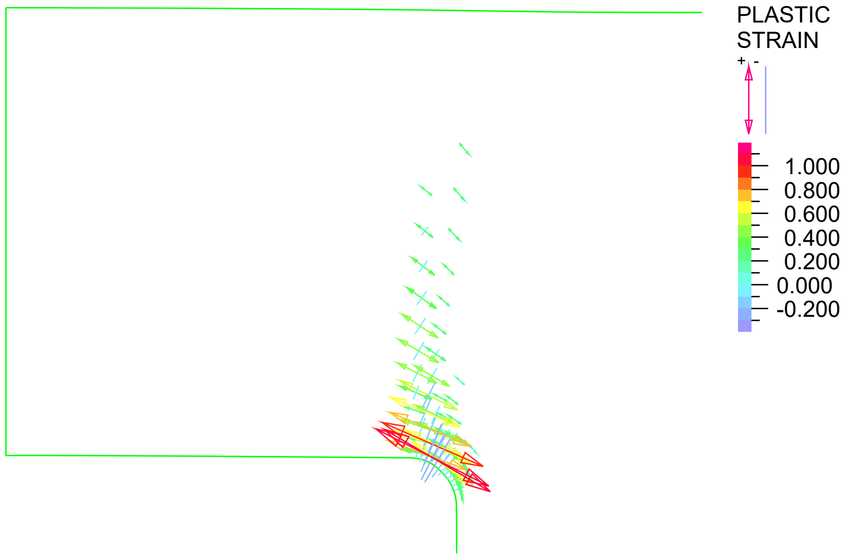

(c) vector plot of directions and magnitudes of the principal plastic strains

Figure A.25: The graphical output of the FE analysis for a bell-jar magma chamber with 10 km in diameter and 5 km beneath surface, inflated till a localized zone of maximum plastic shear strain interconnected the chamber and surface.

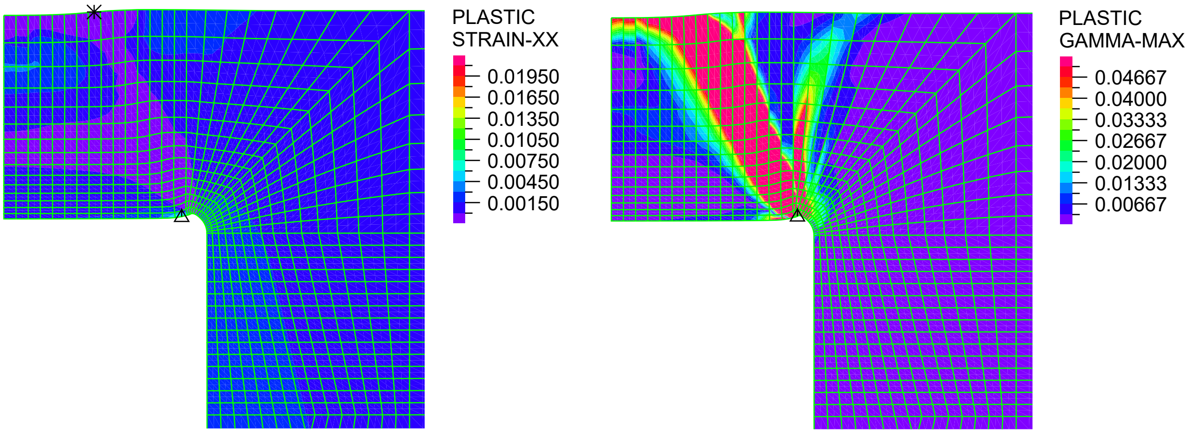

(a) iso-bands of the circumferential plastic normal strain

(b) iso-bands of the maximum plastic shear strain in the radial plane

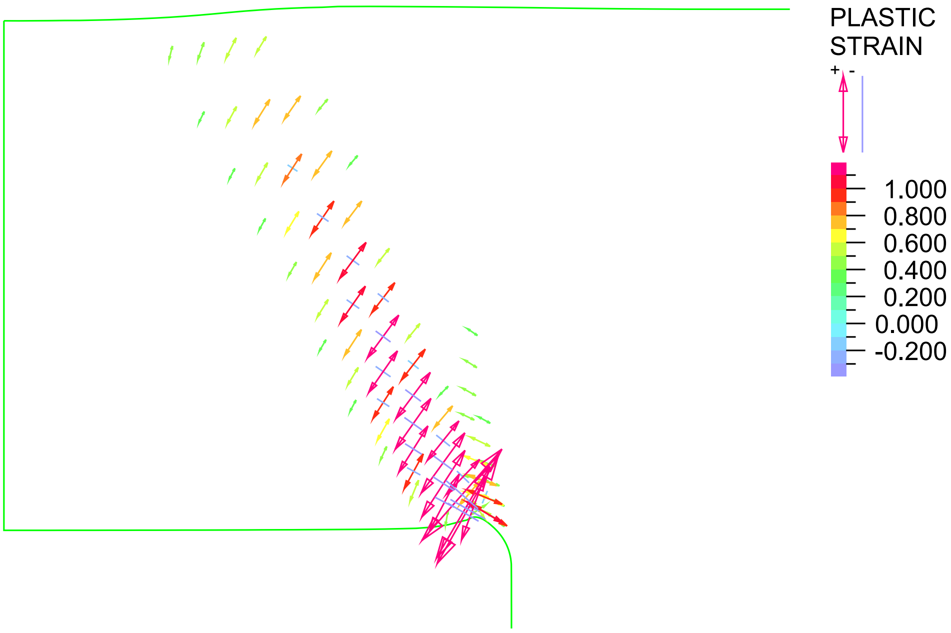

(c) vector plot of directions and magnitudes of the principal plastic strains

Figure A.26: The graphical output of the FE analysis for a bell-jar magma chamber with 10 km in diameter and 5 km beneath surface, deflated till the onset of underpressure collapse.

Case B-10/10

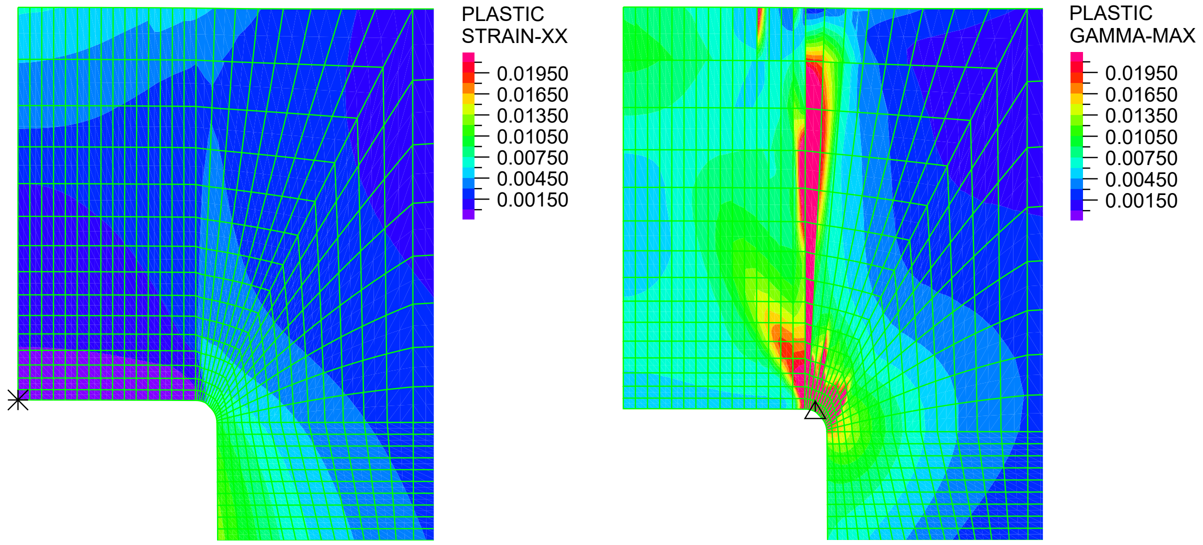

(a) iso-bands of the circumferential plastic normal strain

(b) iso-bands of the maximum plastic shear strain in the radial plane

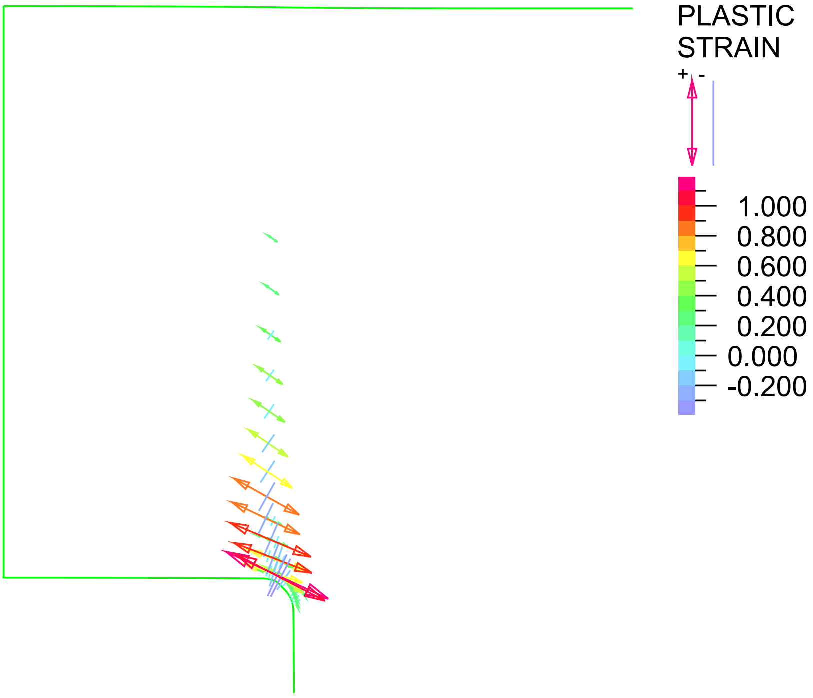

(c) vector plot of directions and magnitudes of the principal plastic strains

Figure A.27: The graphical output of the FE analysis for a bell-jar magma chamber with 10 km in diameter and 10 km beneath surface, inflated till a localized zone of maximum plastic shear strain interconnected the chamber and surface.

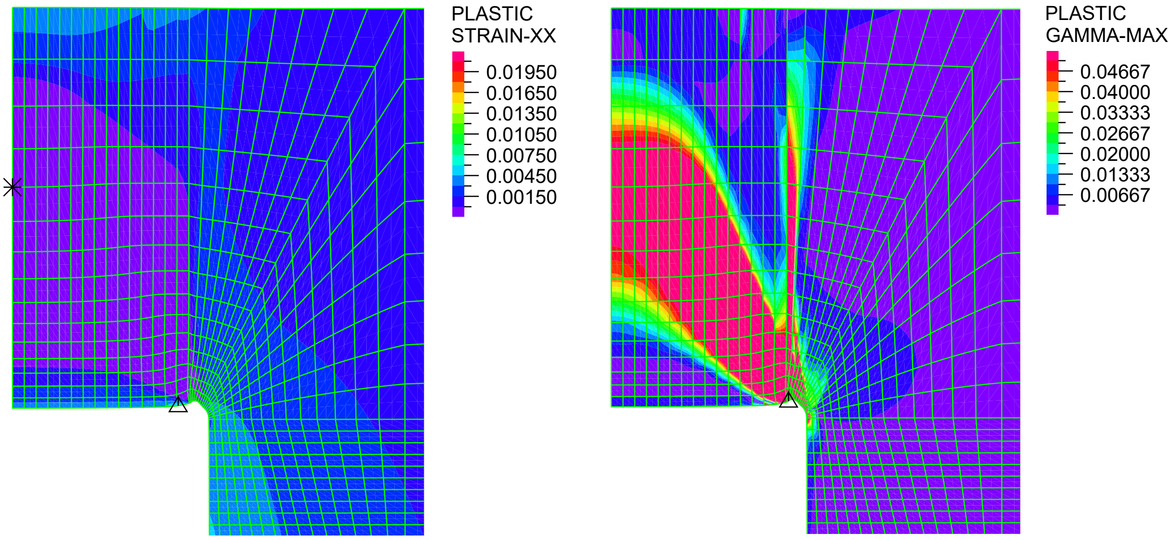

(a) iso-bands of the circumferential plastic normal strain

(b) iso-bands of the maximum plastic shear strain in the radial plane

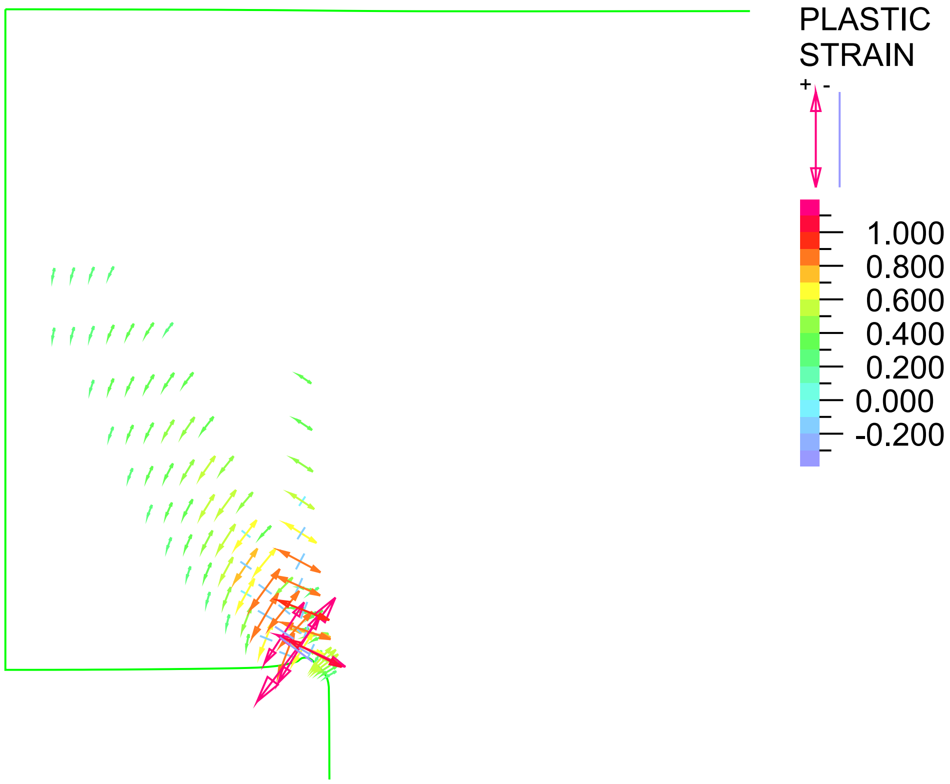

(c) vector plot of directions and magnitudes of the principal plastic strains

Figure A.28: The graphical output of the FE analysis for a bell-jar magma chamber with 10 km in diameter and 10 km beneath surface, deflated till the onset of underpressure collapse.

Case B-50/5

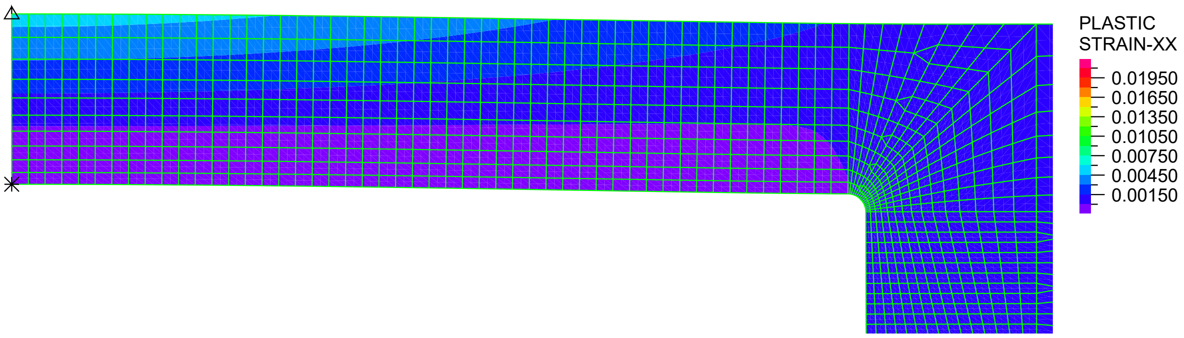

(a) iso-bands of the circumferential plastic normal strain

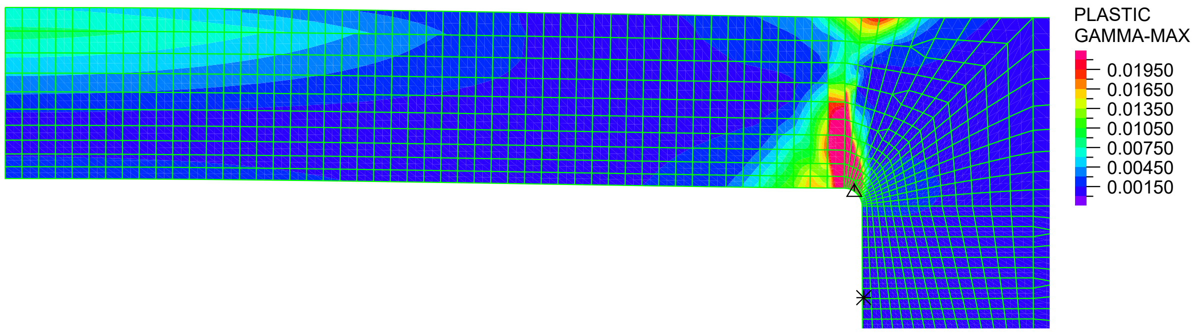

(b) iso-bands of the maximum plastic shear strain in the radial plane

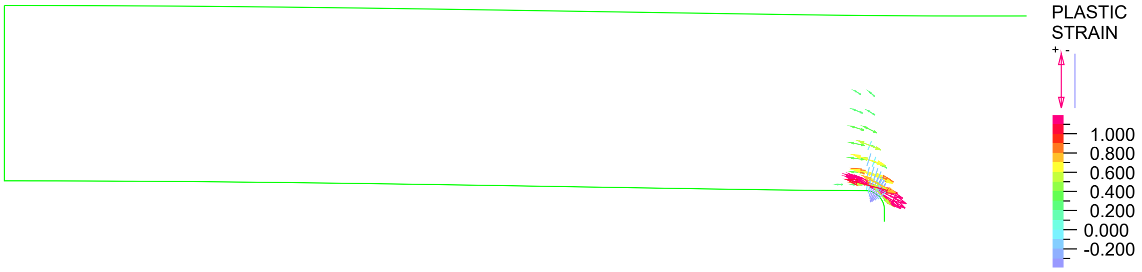

(c) vector plot of directions and magnitudes of the principal plastic strains

Figure A.29: The graphical output of the FE analysis for a bell-jar magma chamber with 50 km in diameter and 5 km beneath surface, inflated till a localized zone of maximum plastic shear strain interconnected the chamber and surface.

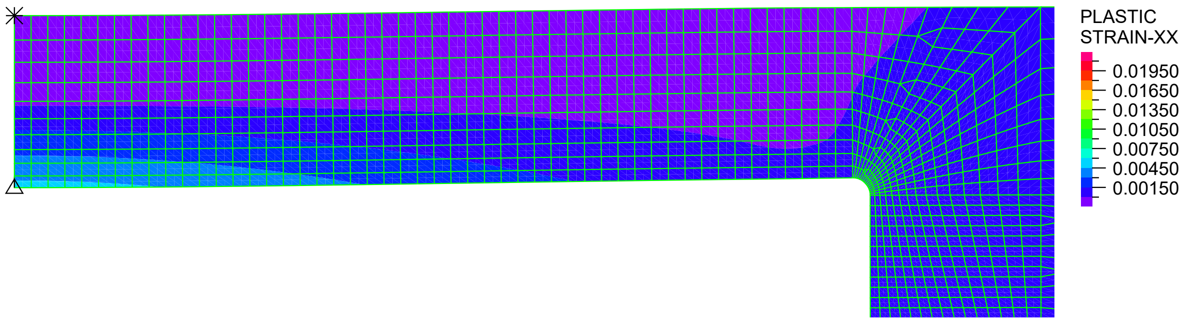

(a) iso-bands of the circumferential plastic normal strain

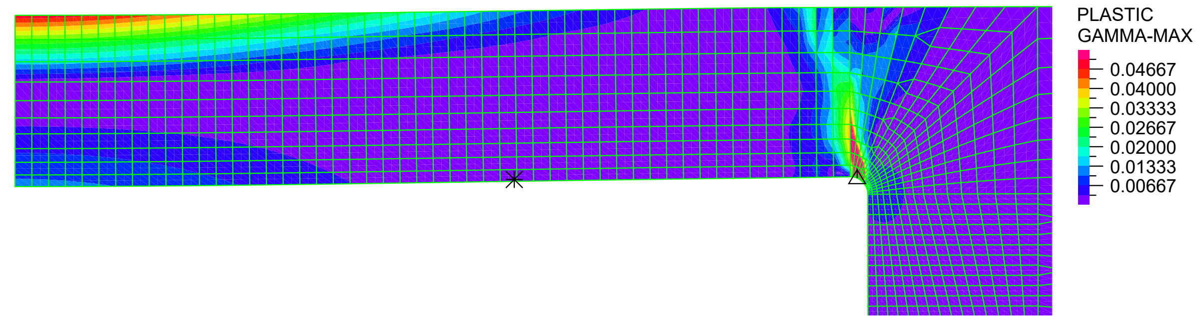

(b) iso-bands of the maximum plastic shear strain in the radial plane

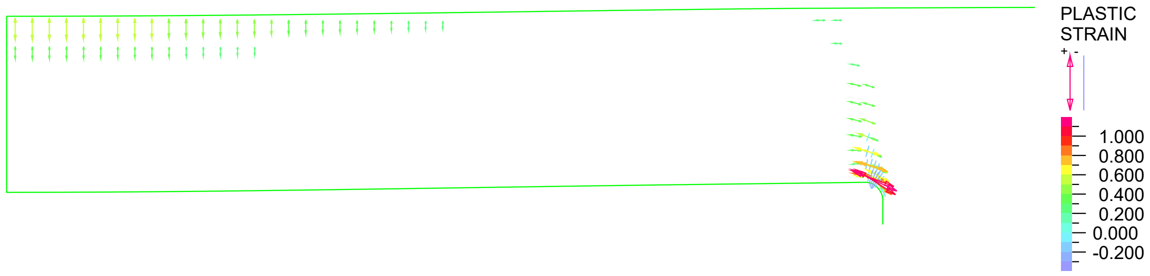

(c) vector plot of directions and magnitudes of the principal plastic strains

Figure A.30: The graphical output of the FE analysis for a bell-jar magma chamber with 50 km in diameter and 5 km beneath surface, deflated till the onset of underpressure collapse.

Case B-50/10

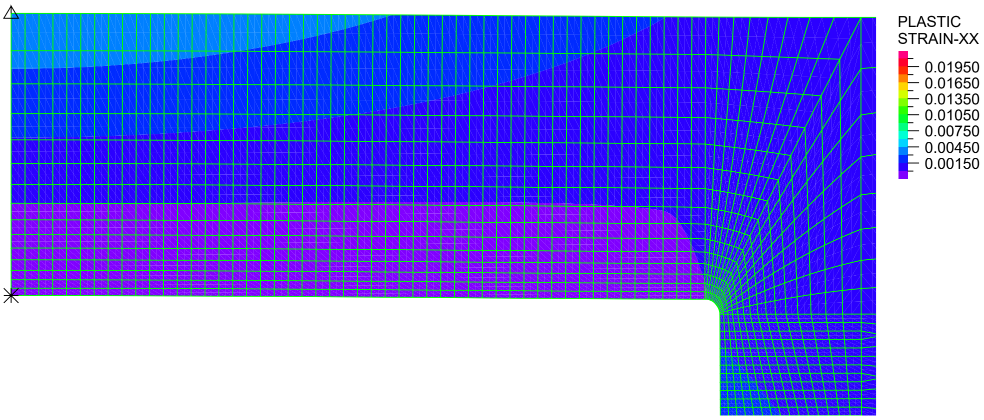

(a) iso-bands of the circumferential plastic normal strain

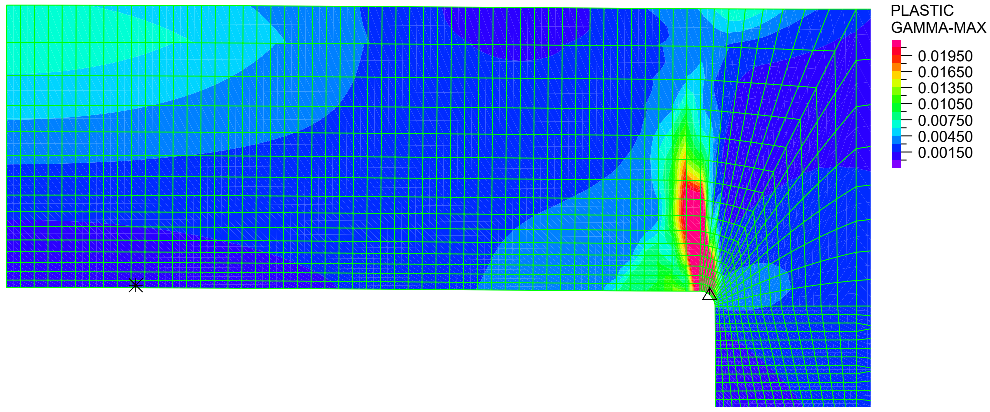

(b) iso-bands of the maximum plastic shear strain in the radial plane

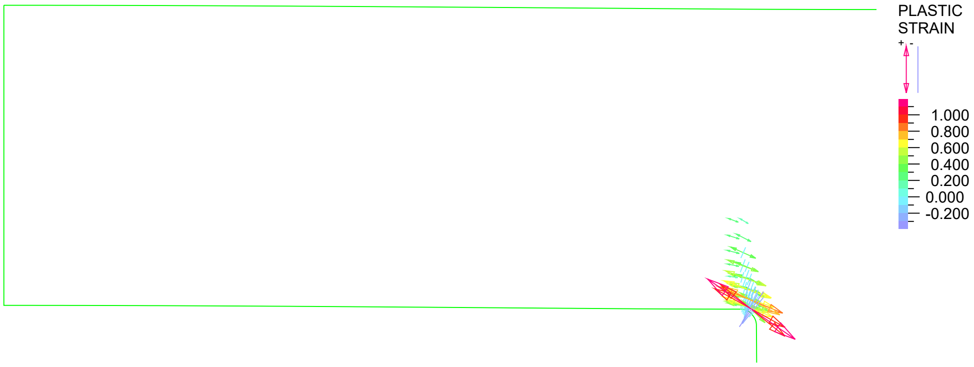

(c) vector plot of directions and magnitudes of the principal plastic strains

Figure A.31: The graphical output of the FE analysis for a bell-jar magma chamber with 50 km in diameter and 10 km beneath surface, inflated till a localized zone of maximum plastic shear strain interconnected the chamber and surface.

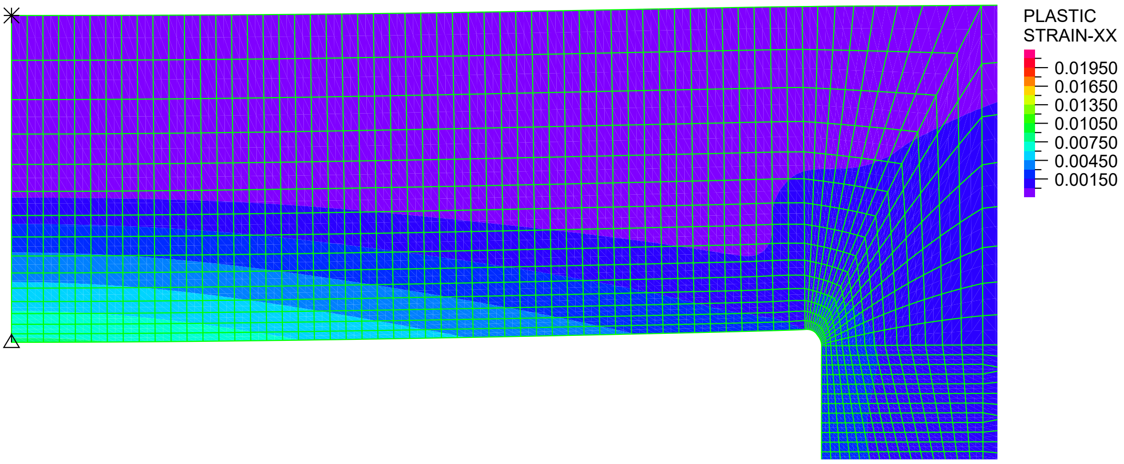

(a) iso-bands of the circumferential plastic normal strain

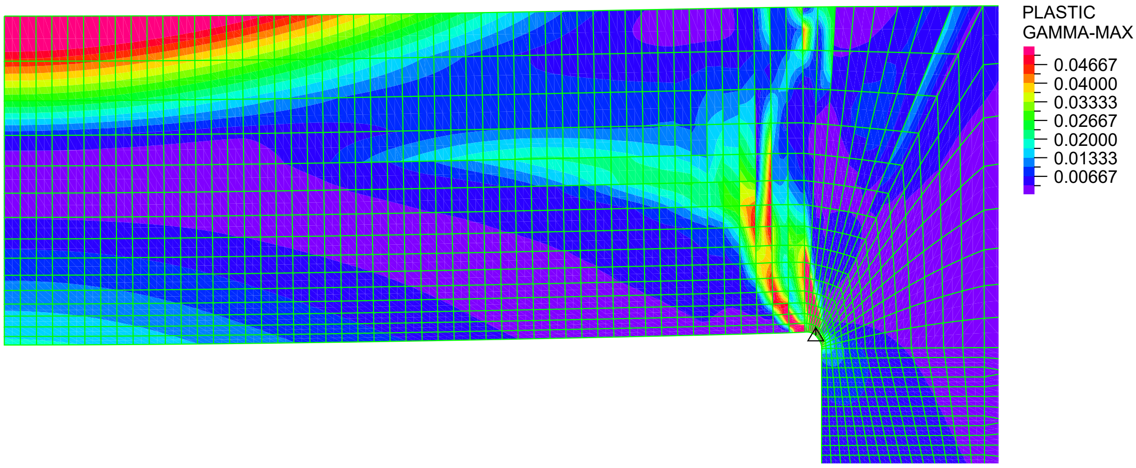

(b) iso-bands of the maximum plastic shear strain in the radial plane

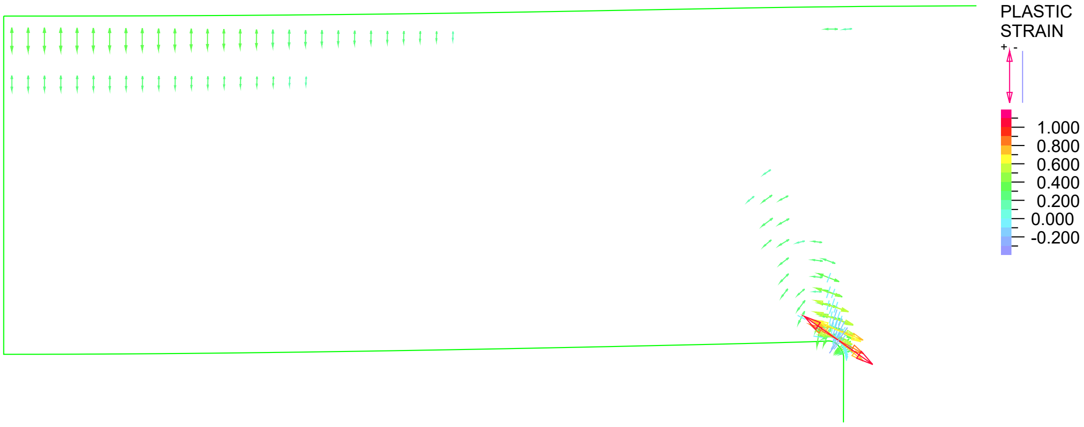

(c) vector plot of directions and magnitudes of the principal plastic strains

Figure A.32: The graphical output of the FE analysis for a bell-jar magma chamber with 50 km in diameter and 10 km beneath surface, deflated till the onset of underpressure collapse.